Pseudoscalar Semileptonic Decays of the D^0 Meson

by

Lorenzo Agostino

Laurea in Physics, University of Pavia, Italy, 2000

A thesis submitted to the

Faculty of the Graduate School of the

University of Colorado in partial fulfillment

of the requirements for the degree of

Doctor of Philosophy

Department of Physics

2004

This thesis entitled:
Pseudoscalar Semileptonic Decays of the D^0 Meson
written by Lorenzo Agostino
has been approved for the Department of Physics

Prof. John P. Cumalat

Prof. Eric Zimmerman

Date

The final copy of this thesis has been examined by the signatories, and we find that both the content and the form meet acceptable presentation standards of scholarly work in the above mentioned discipline.

Agostino, Lorenzo (Ph.D., Physics)

Pseudoscalar Semileptonic Decays of the D^0 Meson

Thesis directed by Prof. John P. Cumalat

The FOCUS experiment is designed to investigate charm particle decays. These charm particles are produced by the interaction of a photon beam with an average energy of 175 GeV on a BeO target and travel an average of few millimeters before decaying in the spectrometer. By reconstructing the daughters from the decay, we can infer properties of the charm particles.

Semileptonic decays have been used to measure many CKM matrix elements. These decays are interesting due to the simplicity of their theoretical description but they are experimentally challenging due to the fact that a neutrino is not detected. Analysis of semileptonic decays in the charm sector are of great interest because they provide an excellent environment to test and to calibrate theoretical calculation that can be implemented in the determination of poorly known matrix elements such as V_{ub}.

In this thesis we report an analysis of the decays $D^0 \to \pi^-\mu^+\nu$ and $D^0 \to K^-\mu^+\nu$. We measure the relative branching ratio as well as the ratio of the form factors $f_+^\pi(0)/f_+^K(0)$. Using a weighting technique, we further report a parametric analysis of the q^2 dependence for both the decay modes measuring the pole masses. For the decay $D^0 \to K^-\mu^+\nu$, we report on the form factor ratio $f_-^K(0)/f_+^K(0)$. Our results are:

$$\frac{\Gamma(D^0 \to \pi^-\mu^+\nu)}{\Gamma(D^0 \to K^-\mu^+\nu)} = 0.074 \pm 0.008\ (stat.) \pm 0.007\ (sys.)$$

$$m_\pi = 1.91^{+0.30}_{-0.15}\ (stat.) \pm 0.07\ (sys.)$$

$$m_K = 1.93^{+0.05}_{-0.04}\ (stat.) \pm 0.03\ (sys.)$$

$$\frac{f_-^K(0)}{f_+^K(0)} = -1.7^{+1.5}_{-1.4}\ (stat.) \pm 0.3\ (sys.)$$

$$\frac{f_+^\pi(0)}{f_+^K(0)} = 0.85 \pm 0.04\ (stat.) \pm 0.04\ (sys.) \pm 0.01\ (\mathrm{CKM})$$

Finally, we report a non-parametric study of the q^2 dependence of the form factor for the decay $D^0 \to K^-\mu^+\nu$.

To my mother and my father.

Acknowledgements

Before thanking anyone else I want to thank my mother and my father for the great support that, as usual, they showed me. I know that leaving far from each other was hard, but you always encouraged me to do what I thought it was good for my life. I'll never forget it, this thesis is for you.

These four years in Colorado have been a wonderful experience under many points of view. It has been great professionally, because I met so many great physicists from whom I tried to learn as much as I could. But it has been at least as great from the human point of view since the very same people always showed me great friendship and support. I would like to thank anybody that contributed to make this a great experience.

The first person I want to thank is my advisor John Cumalat. Since my first day in Colorado he showed all the qualities that anyone would want in the persons they work with. Even though his experience and knowledge are far greater than mine he always treated me more as a collaborator than as a student. I thank him very much for that. Further, I want to thank him for all the fun I had with him in many occasions. The only regret, not beating him at ping pong.

A special thank to Brian O'Reilly, Kevin Stenson and Eduardo Ramirez. All of you made the Colorado group a very stimulating place to work, I learned a lot from you. I want to thank you also for your friendship (which in the case of Brian came out only after the 6th beer) and the time spent outside the physics building.

To the FOCUS collaboration: thank you so much for everything. I can't imagine working in a better collaboration. I consider myself very lucky to have worked with all of you. Among all, I would like to mention Harry Cheung, that encouraged me to apply to Colorado; Will Johns, that taught me a lot about semileptonic analyses; Jim Wiss, of whom I was able to appreciate the great physics skills.

Another thank to all the people that were not related to FOCUS but that made these four years so beautiful. You are too many to thank one by one, but I want you to know that it has been a pleasure to meet you and that all off you enriched me very much.

At last, my biggest thanks to Dr. Ilaria Segoni, the most important person of all. No matter where I am and no matter what I am doing, sharing it with you makes it always worth it. You keep inspiring me and I am looking forward to spend the rest of my life with you.

Contents

Tables

Table

Figures

Figure

Chapter 1

Introduction

1.1 The Standard Model

The Standard Model is the theoretical framework that describes electromagnetic, weak and strong interactions. In the Standard Model picture, there are three kinds of elementary particles: leptons and quarks (organized in three generations) and the gauge bosons that mediate these three interactions. The three lepton generations are :

$$\begin{pmatrix} e \\ \nu_e \end{pmatrix}, \begin{pmatrix} \mu \\ \nu_\mu \end{pmatrix}, \begin{pmatrix} \tau \\ \nu_\tau \end{pmatrix}$$

which are classified according to their charge (± 1 for electron, muon and tau and zero for the neutrinos) and *lepton number*.[1] The three generations of quarks are instead characterized by a (fractional) charge, a *flavor* (the quark type) and the *color* that can be viewed as the equivalent of the electric charge in the strong interaction:

$$\begin{pmatrix} u \\ d \end{pmatrix}, \begin{pmatrix} c \\ s \end{pmatrix}, \begin{pmatrix} t \\ b \end{pmatrix}.$$

In Table 1.1 we summarize the properties of the gauge bosons which couple to quarks and leptons. Up to now only electromagnetic and weak interaction can be calculated analytically, the strong interaction contributions to a given process are generally computed using a perturbative approach or numerical calculations on the lattice.

[1] Electron and neutrino have for instance electron lepton number -1 while the positron and antineutrino have electron lepton number +1.

Interaction	Mediator	Spin	Mass (GeV/c^2)
Electromagnetic	γ	1	0.
Weak	$W^{\pm}$	1	$\sim$ 80, $\sim$ 90
Strong	g	1	0.

Table 1.1: Mediators of the electromagnetic, weak and strong interactions.

There are also attempts to explain gravity as a quantum field theory but the mediator of the gravitational force (the graviton) has not been observed. Theoretical predictions suggest the graviton to be massless, chargeless and with spin 2.

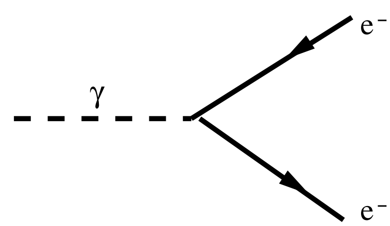

Figure 1.1: Electromagnetic process to first order in the S matrix expansion.

In quantum electrodynamics (QED) the photon couples to charged particles (lepton or quarks) with a coupling constant $\alpha_e = 1/137$. The electromagnetic Hamiltonian (in the Dirac description) can be written as:

$$H_I^{e.m.} = -e\bar{\psi}\gamma^{\alpha}A_{\alpha}\psi \tag{1.1}$$

and describes the basic electromagnetic vertex shown in Fig. 1.1 (first order in α_e) between a free electron and a photon[2] .

The electroweak Hamiltonian can be written as a generalization of the electromagnetic Hamiltonian 1.1 as:

$$H_I^{e.w.} = g_W J^{\alpha +} W_{\alpha} + g_W J^{\alpha} W_{\alpha}^{+} \tag{1.2}$$

[2] This process is forbidden by energy and momentum conservation. Other particles must be present to have allowed processes.

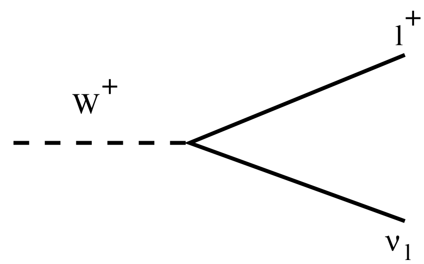

Figure 1.2: Weak process to first order in the S matrix expansion.

where W_α is the W gauge boson field while the charged current J^α follows from the V-A interaction theory and is given by $J^\alpha = \Sigma_l \bar{\psi}_l \gamma^\alpha (1-\gamma_5)\psi_{\nu_l}$. The graphical representation of a weak vertex is shown in Fig. 1.2 .

If we consider the decay of the muon, shown in Fig. 1.3, the decay amplitude that describes the dynamical part of the process can be written as :

$$M = -ig_W^2 \bar{u}(p', r')\gamma^\beta(1-\gamma_5)v(q_1, r_1)\left(\frac{-g_{\alpha\beta} + q_\alpha q_\beta}{q^2 - M_W^2 + i\varepsilon}\right)\bar{u}(q_2, r_2)\gamma^\alpha(1-\gamma_5)u(p, r) \quad (1.3)$$

which in the approximation of $q^2 << M_W^2$ becomes:

$$M = \frac{g_W^2}{8(M_W c)^2}[\bar{u}(p', r')\gamma^\alpha(1-\gamma_5)v(q_1, r_1)][\bar{u}(q_2, r_2)\gamma_\alpha(1-\gamma_5)u(p, r)]. \quad (1.4)$$

This form of the decay amplitude will be important for the discussion of semileptonic decays described in this thesis. In fact, the matrix element written as a product of

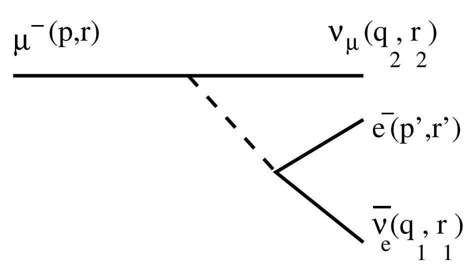

Figure 1.3: The muon decays weakly in an electron a muon neutrino and an electron anti-neutrino.

two currents becomes very handy when one vertex couples the W boson to a hadronic current.

The way the mediators couple to particles is not trivial. The photon couples to electrically charged particles (quarks or leptons) while the $W^{\pm}$ and the Z^0 couple also to the chargeless neutrinos[3] . Since the quark mass eigenstates are not the weak eigenstates, the intermediate bosons $W^{\pm}$ couple to the pairs

$$\begin{pmatrix} u \\ d' \end{pmatrix}, \begin{pmatrix} c \\ s' \end{pmatrix}, \begin{pmatrix} t \\ b' \end{pmatrix}$$

where the d', s' and b' states, are obtained by the transformation of the physical quarks through the Cabibbo-Kobayashi-Maskawa (CKM) matrix:

$$M = \begin{pmatrix} V_{ud} & V_{us} & V_{ub} \\ V_{cd} & V_{cs} & V_{cb} \\ V_{td} & V_{ts} & V_{tb} \end{pmatrix}$$

which allows cross-generational transitions. A useful approximate representation of the CKM matrix is given by the Wolfenstein parametrization [1]:

$$M = \begin{pmatrix} 1-\frac{1}{2}\lambda^2 & \lambda & A\lambda^3(\rho - i\eta) \\ -\lambda & 1-\frac{1}{2}\lambda^2 & A\lambda^2 \\ A\lambda^3(1-\rho-i\eta) & -A\lambda^3 & 1 \end{pmatrix} + \mathcal{O}(\lambda^4)$$

where $\lambda = \sin\theta_c \sim 0.22$ is the sine of the Cabibbo angle while ρ, η and A are additional free parameters in the Standard Model. Two features should be noticed: first, the more one moves away from the diagonal terms the smaller the matrix elements become, this means that off-diagonal transitions are suppressed relative to the diagonal ones. Second is the presence of a phase in the terms proportional to λ^3. This phase is responsible for CP violation in the Standard Model. Further, weak interactions of quarks are not

[3] The coupling of Z^0 to quarks which give flavor changing neutral current does not exist to first order and is highly suppressed by the GIM mechanism [2].

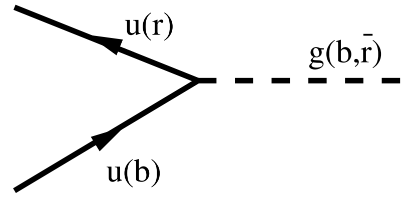

Figure 1.4: Strong vertex where an up-blue quark converts to an up-red quark by emission of a gluon.

easily accessible because the quarks are *confined* within hadrons (mesons or baryons) by the strong interaction.

Gluons mediate the strong force and they couple to each other and to quarks (Fig. 1.4) which come in six flavors and three colors (the "strong charge" introduced to explain baryonic bound states, saving Pauli's principle). The fact that there are three colors creates a big difference with respect to the electromagnetic interaction since the color (but not the flavor) can change during a strong process. This means that the gluon itself carries the "color charge".

We could ask if the Standard Model hides a more general picture. Since the early seventies people have thought about the possibility of combining electromagnetic, weak and strong theories into a *grand unified theory.*

The point was raised by the observation that α_s decreases at short distances (high energy) and so does the weak coupling α_w but at a slower rate. On the other hand the electromagnetic constant increases. By extrapolation, the three constants

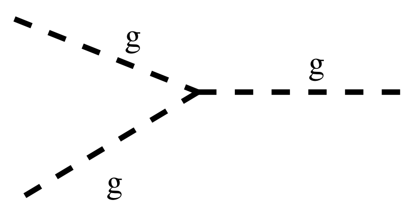

Figure 1.5: Since gluons carry color, strong interaction can couple multiple gluons as well as gluons to quarks.

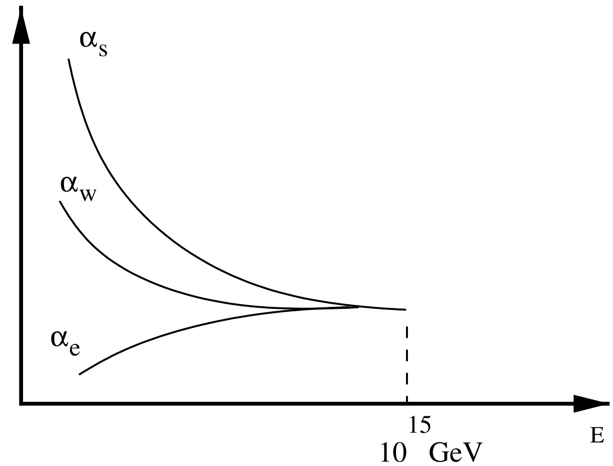

Figure 1.6: The graph shows running coupling constants which (by extrapolation) should converge around 10^{15} GeV.

seem to converge around 10^{15} GeV (Fig. 1.6) suggesting that these three interactions are only different manifestation of the same force.

Up to now, only the weak and the electromagnetic interactions have been unified. The Glashow, Weinberg and Salam theory starts with four massless mediators, three of which acquire masses through the Higgs mechanism (becoming the $W^{\pm}$, Z^0) while one remains massless: the photon.

The Standard Model had a big success in predicting the physical processes that we observe in experiments. Even so, there are still many issues that either cannot be explained (like the three generations scheme of quarks and leptons or the origin of baryonic asymmetry in the universe) or have not been precisely calculated (like the role of strong interaction effects in weak decays) within this model. Further, the Standard Model has many free parameters that are used to make predictions but are not explained, such as the quark masses and the Cabibbo angle (or in general the three angles of the CKM matrix). For many years semileptonic decays have been one of the most useful tools to address some of these questions. For example, most of the CKM matrix elements have been measured using these decays as shown in Fig. 1.7.

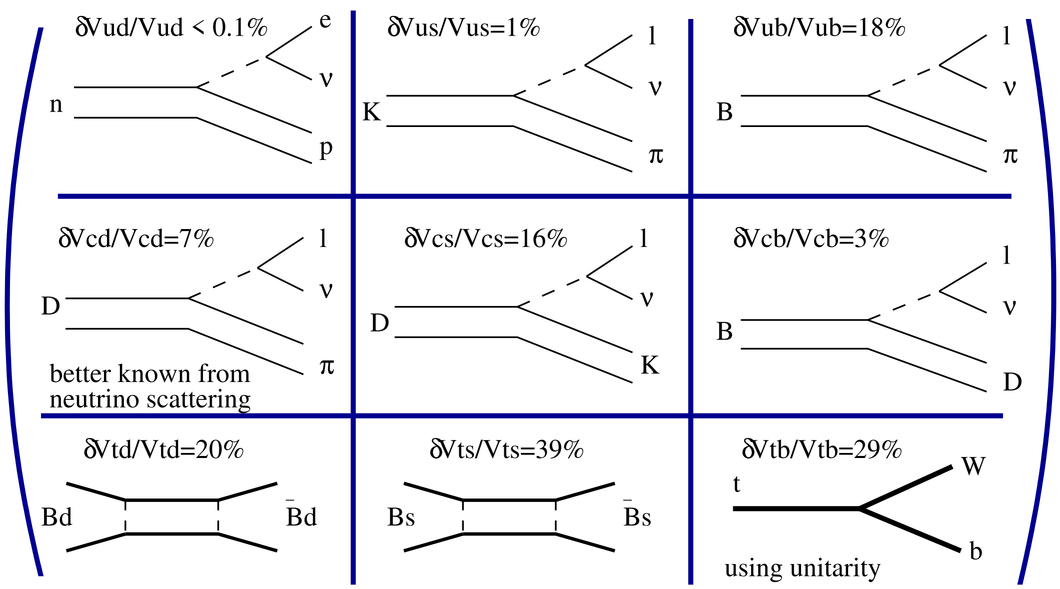

Figure 1.7: The matrix shows the current uncertainties on the CKM matrix elements and the decay modes that have been used to measure them. Semileptonic decays have played an important role in these measurements.

1.2 Weak Interactions and Semileptonic Decays

After a historical introduction of the β decay we will describe the properties of semileptonic decays, concentrating on heavy hadron systems. Most of the physics can be explained by looking at the distributions of variables such as q^2 (which is the square of the momentum transfer) and lepton energy [3]. We will also give a description of commonly used theoretical models for these decays.

1.2.1 The β Decay

Soon after Becquerel's experiments on radioactivity in 1896, it was recognized that one type of radioactivity consists of emission of β rays by nuclei. The observation of a continuum spectrum for the electron energy arising from these decays and the consequent idea of Pauli about the existence of a new particle with almost zero rest mass and half integer spin, induced Fermi to create a theory of β decay [4]. He called the new particle *neutrino*. In his theory the decay chain $n \to p + e^- + \bar{\nu}_e$ was described by the Hamiltonian :

$$H = \frac{-G_F}{\sqrt{2}} \bar{\psi}_p \gamma_\alpha \psi_n \bar{\psi}_e \gamma^\alpha \psi_\nu. \tag{1.5}$$

that describes the point-like interaction of four fermions. In the following years new discoveries like the non-conservation of parity in weak processes by C. S. Wu et al. [5] and the observation of new weak decays like $K^0 \to \pi^+ e^- \bar{\nu}_e$ were made. The new data showed that Fermi's Hamiltonian had to be modified subtracting a axial-vector term $A = \bar{\psi}\gamma^\alpha\gamma_5\psi$ from the vector term $V = \bar{\psi}\gamma^\alpha\psi$.

All the weak phenomena including the suppression of the decay $\pi^- \to e^- \bar{\nu}_e$ with respect to $\pi^- \to \mu^- \bar{\nu}_\mu$ are explained by the $V-A$ interaction theory. Today the diagram describing the β-decay is the well known tree diagram shown in Fig. 1.8.

On the other hand, as we already pointed out, weak interaction of quarks can be

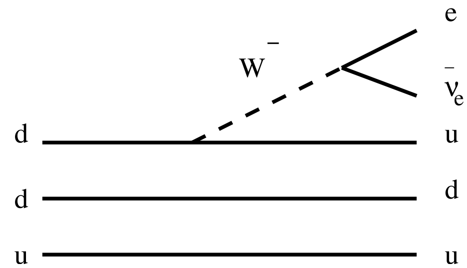

Figure 1.8: In the β decay a neutron decays to a proton and a W^- boson and the W decays subsequently to an electron-neutrino pair.

complicated by the strong force as quarks are confined in hadrons. If we apply the same formula used in the computation of the muon lifetime to the β decay, treating neutron and proton as point-like particles, then the lifetime turns out to be $\tau = 1316$ sec instead of about ~ 900 sec. Neglecting the internal structure of the nucleons provides only a crude approximation of the physics involved in the process [6]. In the next section we will show how the internal structure of the hadrons is handled by describing the hadronic current in terms of two functions of q^2.

1.2.2 The Decay Probability

In this section we concentrate on the semileptonic decay of where the initial and final state hadrons are two pseudoscalar particles. As an example, we consider the decay $D^0 \to K^- l^+ \nu$. For such a decay, the expression for the decay probability is:

$$d\Gamma = \frac{1}{(2\pi)^5}\frac{1}{4P_0}|\mathcal{M}|^2 m_l m_\nu \frac{d^3\mathbf{Q}}{Q_0}\frac{d^3\mathbf{q}}{q_0}\frac{d^3\mathbf{p}}{p_0}\delta^4(Q+p+q-P)$$

where P and Q are the 4-momenta of D^0 and the kaon and p and q the 4-momenta of the lepton and neutrino respectively. The decay amplitude $\mathcal{M}$ can be written according to Eq. 1.4 as:

$$\mathcal{M} = \frac{G}{\sqrt{2}} J^H_\mu [\bar{u}_\nu \gamma_\alpha (1-\gamma_5) u_l]$$

where the hadronic current J^H contains all the contributions of the strong interaction and is not known analytically. The hadronic current can be expressed in terms of two functions of q^2, called form factors $f_\pm$ (a detailed discussion on the form factors will be given in the next section):

$$J^H = \frac{1}{2}[f_+(q^2)(P+Q) + f_-(q^2)(P-Q)] = f_+(q^2)P - \frac{1}{2}f_+(q^2)(1-\xi)(p+q)$$

where $\xi \equiv f_-(q^2)/f_+(q^2)$. By using this form of the hadronic current, the differential decay rate becomes:

$$\frac{d^2\Gamma}{dQ_0\ dp_0} = \frac{G_F^2}{16\pi^3}|V_{cs}|^2|f_+(q^2)|^2[A + B\ Re\xi + C|\xi|^2]. \tag{1.6}$$

where V_{cs} is the CKM matrix element associated with the quark transition $c \to s$. The kinematic coefficients A, B, and C are given by:

$$A = m_D[2p_0q_0 - m_D(W_0 - Q_0)] + 1/4m_l^2(W_0 - Q_0) - m_l^2 q_0,$$

$$B = m_l^2[q_0 - 1/2(W_0 - Q_0)],$$

$$C = 1/4m_l^2(W_0 - Q_0)$$

where $W_0 = (m_D^2 + m_K - m_l^2)/2m_D$ and m_D, m_K, and m_l are the D^0, the kaon, and the lepton masses, respectively [7]. If we assume the lepton mass to be negligible[4] , the differential decay rate can be written in the simple form:

$$\frac{d^2\Gamma}{dq^2} = \frac{G_F^2}{16\pi^3}|V_{cs}|^2|f_+(q^2)|^2|\vec{Q}|^3. \tag{1.7}$$

where $|\vec{Q}|$ is the momentum of the final state hadron. That the lepton mass has a small effect on the decay amplitude can be easily seen in Fig. 1.9 where we compare the generated distribution that accounts for the mass term and the functional form obtained

[4] This assumption works well when the final state lepton is an electron.

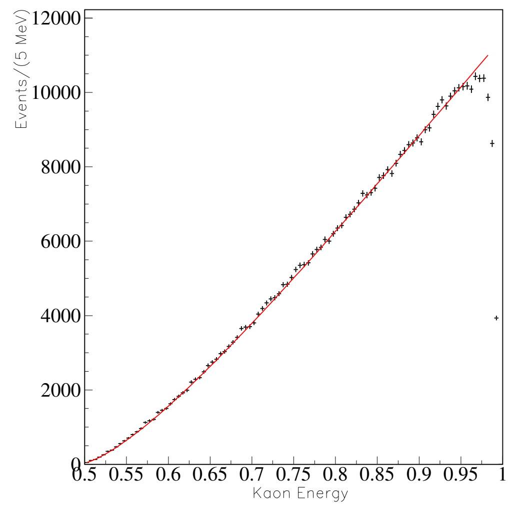

Figure 1.9: Mass term effect on the kaon energy distribution of the decay $D^0 \to K^-\mu^+\nu$: the fit is performed using a functional form that neglects the mass term and it shows that this approximation works very well up to the high edge of the kaon energy spectrum.

by neglecting this term. The mass term affects the high edge of the kaon energy region while it has virtually no effect on most of the spectrum.

1.2.3 Parametrization of the Form Factors

Many exclusive semileptonic decay analyses are model dependent in that the final measurement will depend on the value that theoretical models predict for some parameter. As pointed out in the previous section, the semileptonic decay rate can be factorized into a well understood leptonic current and into a hadronic current that can be expressed in terms of two form factors.

In order to compare theoretical predictions to experimental results, a choice for the parametrization of the q^2 dependence of the form factors f_+ and f_- has to be made. In any parameterization, the overall behavior is the same, namely the form factor will have a minimum at $q^2 \sim 0$ and will increase monotonically for increasing values of q^2.

In this analysis we implement two different parametrizations of the form factors: the pole dominance form and the modified pole form [8] which are described in Eqs. 1.8

and 1.9:

$$f_{\pm}(q^2) = \frac{f_{\pm}(0)}{1 - \frac{q^2}{m^2_{pole}}} \tag{1.8}$$

$$f_{\pm}(q^2) = \frac{f_{\pm}(0)}{[1 - \frac{q^2}{m^2_{pole}}][1 - \frac{\alpha\ q^2}{m^2_{pole}}]}. \tag{1.9}$$

The normalizations $f_{\pm}(0)$ are the form factor values in the maximum recoil configuration, m_{pole} is the so called *pole mass* and α is a parameter that measures how much the q^2 dependence differs from the simple pole dominance, due to the contribution of higher states (poles) to Eq. 1.8.

A way to picture the idea behind Eq. 1.8 is given in Fig. 1.10 in the case of D^0 decaying to $K^-\mu^+\nu$. The charm and the strange quarks form a resonant bound state that couples to the W boson. The quantum numbers of this state have to be the same as the quantum numbers of the W^+. The lowest $c\bar{s}$ state with the proper quantum numbers is the D_s^* with a mass of 2.114 GeV/c^2. Today, it's commonly accepted that even if the pole form is correct, higher state particles (or even multi-particle systems) will give some additional contribution. This contribution will be bigger in the region of

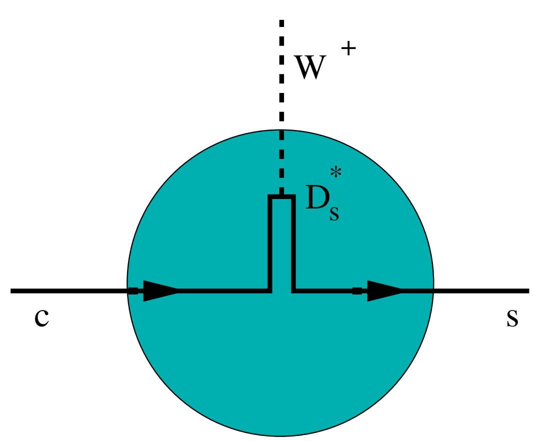

Figure 1.10: Graphical representation of the pole dominant parameterization of the form factor. The W^+ couples to an intermediate state formed by a c and an $\bar{s}$ state with the same quantum numbers as the W^+. The first state available is the D_s^* (2114).

low q^2 where the effect of the dominant pole is comparable to the effect of these higher states. At some level, this “interference” will result in a distortion of the single pole behavior at low q^2 [9]. With the modified pole parametrization in Eq. 1.9, we can quantify this distortion.

1.2.4 Dynamics of Semileptonic Decays

Let’s take a heavy pseudoscalar ($j = 0$) meson like a D or a B meson which decays to a lighter pseudoscalar or vector meson plus a lepton-neutrino pair. A very useful way to describe the dynamical properties of the decay is to look at the Dalitz plot [3] which describes the decay probability for different kinematic configurations (Fig. 1.11).

In this example the Dalitz plot has been generated for the decay $D^0 \to K^-\mu^+\nu$ and $D^0 \to \pi^-\mu^+\nu$ (by Monte Carlo simulation) according to Eq. 1.6. The kinematic variables used in describing the Dalitz plot are q^2 (the 4-momentum transferred by the W, proportional to the daughter hadron energy through the formula $q^2 = M_D^2 + M_K^2 - 2\ M_D\ E_K$) and the lepton energy in the D rest frame. The pure phase-space would be uniform over the Dalitz plot, with any modulation given by the dynamical part of the decay rate. The best way to explain the structure of the Dalitz plot is to investigate separately the effects that influence the q^2 and the lepton energy distributions.

The first effect on the q^2 distribution is the hadronization process of the kaon. This can be understood in terms of the relative velocity of the recoiling quark from the decay and the spectator quark (Fig 1.12 shows the possible configurations for a D meson decay) forming the final state hadron. In the kinematic configuration where the q^2 is large (Fig. 1.12b), the spectator quark and the daughter quark from the decay are at rest with respect to one another. This produces a system that has a large overlap with the wave-function of an ordinary meson like a K^- or a K^{*-}. This configuration is called *zero-recoil* and is the configuration where the form factors have maximum value.

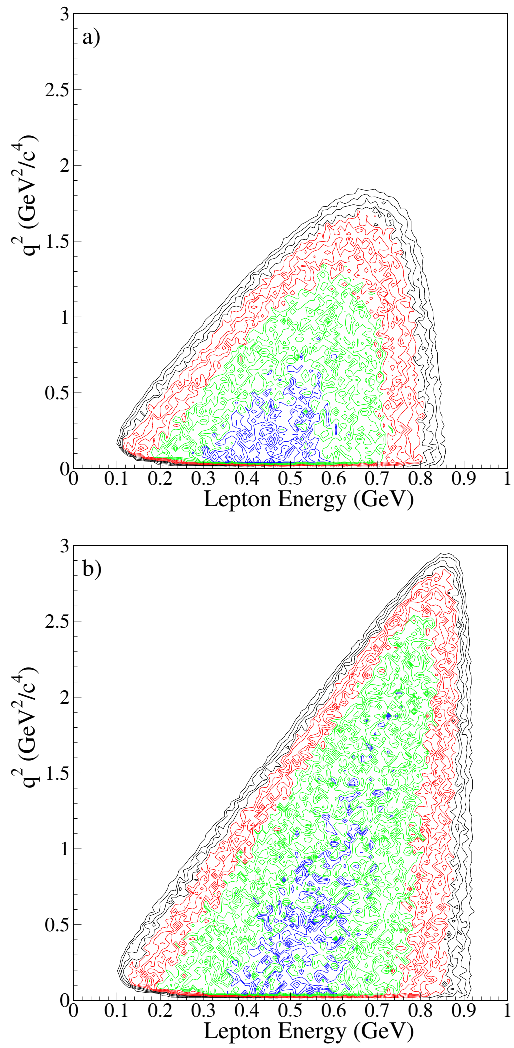

Figure 1.11: Dalitz plot of the decays $D^0 \to K^-\mu^+\nu$ (a) and $D^0 \to \pi^-\mu^+\nu$ (b) as a function of the variables q^2 and lepton energy. The blue region indicates the highest decay intensity.

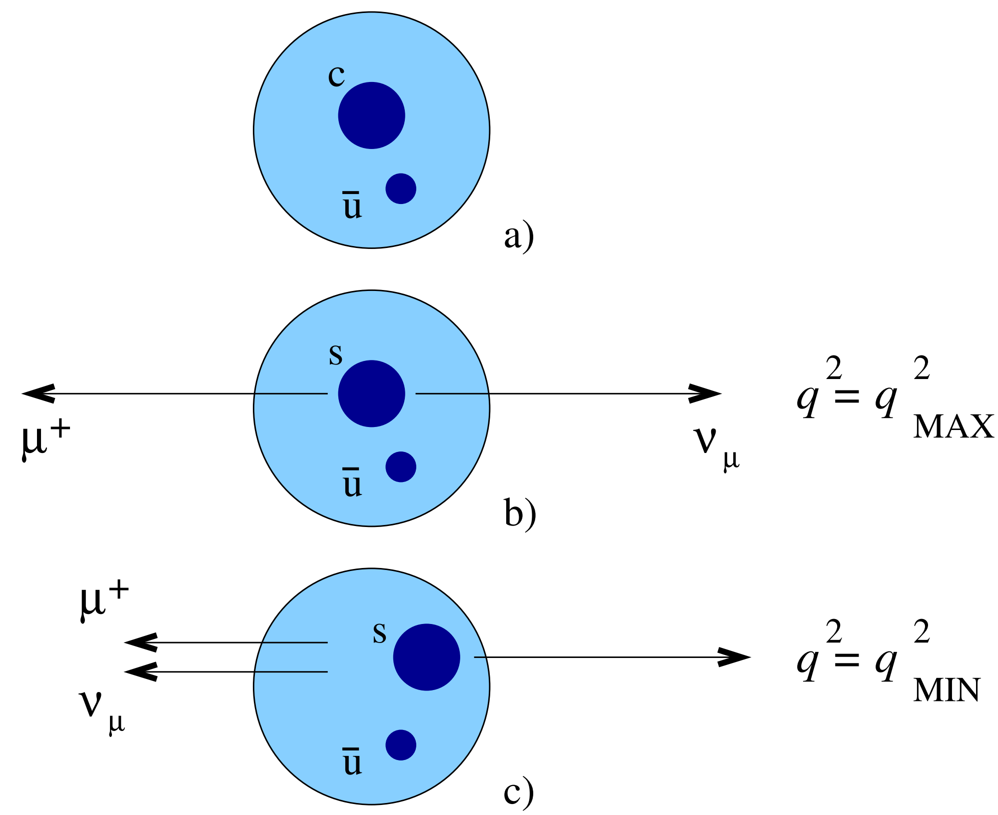

Figure 1.12: Possible kinematic configurations during the hadronization process of a D^0 meson decaying to a kaon: (a) The D^0 meson before the decay; (b) decay configuration for $q^2 = q^2_{max}$, where the form factors are large for producing a kaon (or a K^*) meson in the final state; (c) configuration for $q^2 = q^2_{min}$ where the form factors are smallest.

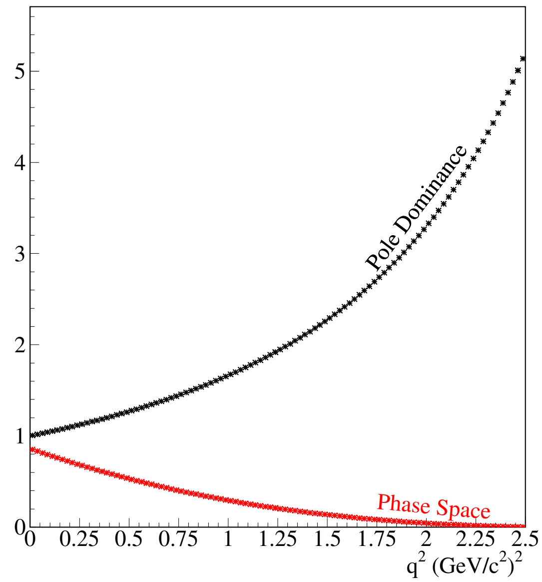

Figure 1.13: Comparison between the pole dominance parametrization of the form factor and the P_K^3 dependence as a function of q^2.

At the other extreme, when the q^2 is very small (Fig. 1.12c), the daughter quark from the decay has a very large recoil velocity relative to the spectator quark. In this case the value of the form factor is small and the resonance formation is less favorable, so the two quarks tend to develop separately in analogy to QCD jets[5] . The two kinematic limits in the hadronization are given when q^2 approaches the maximum value $q^2_{max} \sim 2m_D E_l + \frac{2m_K^2 E_l}{2E_l - m_D}$ and the minimum value $q^2_{min} = m_l^2$ (about zero for electrons).

Another variable that affects the q^2 distribution is the spin of the particles. The W^* (virtual) behaves like a spin 1 object and if both the initial and final state hadrons are pseudoscalar particles, then the process is allowed to occur only via a p-wave while if the daughter hadron is a vector, then s, p, d-waves are allowed. Further, pseudoscalar decay rates are proportional to the third power of the momentum of the daughter hadron (see Eq. 1.7) which suppresses the decay when the q^2 approaches the zero recoil configuration or maximum q^2 (see Fig. 1.13).

[5] This is particularly true in b decays where the phase-space available is large.

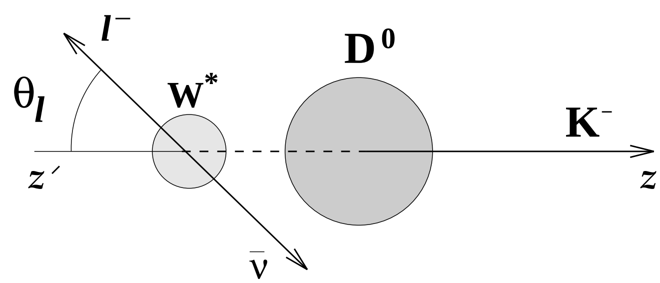

Figure 1.14: The angle θ_l is defined as the angle between the direction of the charged lepton in the W^* rest frame and the direction of the W^* in the meson M rest frame.

The lepton energy is also affected by different variables. The best way to picture the effect of these variables is to look at the angle θ_l which is defined as the polar angle between the charged lepton in the W^* rest frame and the line of flight of the W^* in the heavy hadron rest frame (Fig. 1.14).

At the maximum recoil configuration ($q^2 \rightarrow q^2_{min}$) the W^* has a big boost which increases the energy of the leptons emitted in the same direction of the W^*. For the minimum recoil configuration ($q^2 \rightarrow q^2_{max}$) the W^* is produced nearly at rest so the range of lepton energies decreases. For $q^2 \sim q^2_{max}$ the W^* is at rest in the D^0 rest frame and the lepton energy is the same for every value of θ_l.

The $V - A$ interaction affects the variable θ_l (Fig. 1.15) and therefore the lepton energy distribution: in charm (or bottom) decays the quark daughter has predominantly helicity $\lambda = -1/2$. If the final state meson is a pseudoscalar particle, then its helicity is zero and so the helicity information carried by the quarks in the hadronization process is lost. The expected angular distribution for each value of the q^2 is:

$$\frac{dN}{d\cos\theta_l} \sim \sin^2\theta_l$$

In vector decays like $D^0 \rightarrow K^*(892)^-\mu^+\nu$, the recoiling quark ($\lambda = -1/2$) can combine with a spectator quark ($\lambda = \pm 1/2$) to form a $\lambda = 0$ or $\lambda = -1$ meson.

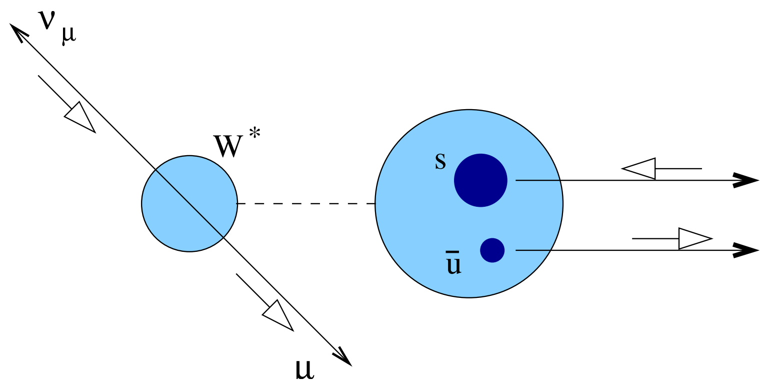

Figure 1.15: The helicity is determined by whether the s quark combine with a quark that has helicity $\lambda = +1/2$ or $\lambda = -1/2$.

This property is experimentally manifested with a higher probability for the final state meson to have a helicity $\lambda = -1$ than for $\lambda = +1$, and, by angular momentum conservation, it applies also to the W^*, affecting the lepton energy (or $\cos\theta_l$) distribution. In charm decays the lepton has $\lambda = +1/2$ so the angular distribution for $\lambda_{W^*} = \pm 1$ is:

$$\frac{dN}{d\cos\theta_l} \sim (1 \pm \cos\theta_l)^2$$

leading to a softer spectrum for $\lambda_{W^*} = -1$ than for $\lambda_{W^*} = +1$. In b decays the charged lepton has $\lambda = -1/2$ so the angular distribution for $\lambda_{W^*} = \pm 1$ is:

$$\frac{dN}{d\cos\theta_l} \sim (1 \mp \cos\theta_l)^2 \tag{1.10}$$

meaning that the lepton energy is harder for $\lambda_{W^*} = -1$ rather than $\lambda_{W^*} = +1$.

1.3 Charm photoproduction

The FOCUS experiment produced charm particles via a photoproduction mechanism. This was achieved by directing a photon beam to a BeO target. Because of flavor conservation, charm quarks are always produced in pairs and the subsequent hadronization process determines the final state meson or baryons. Photoproduction of charm quarks is dominated at lowest order by photon-gluon fusion process [12] illustrated in Fig. 1.16 a), b).

The photoproduction cross section of charm particles depends linearly on the gluon density within a nucleon as well as the partonic cross section:

$$\sigma(\gamma p \to c\bar{c}) = \int_{4m_c^2/s}^{1} dx_g g(x_g, \mu^2)\hat{\sigma}(sx_g)$$

where x_g is the fraction of the nucleon momentum carried by the incident gluon. The next to leading order contributions shown in Fig. 1.16 c), d), e), f) are significant in charm and they have to be included in the Monte Carlo simulation to provide a satisfactory match to the data.

An interesting feature of this mechanism is that during the hadronization process an asymmetry in the particle-antiparticle momenta arises from the difference between the momentum fraction of the nucleon remnant from the target carried by the quark and di-quark (Fig. 1.17). The charm quark dresses with the di-quark remnant from the nucleon forming a baryon while the anti-charm quark binds to the remaining quark forming an anti-meson. The same process is responsible for an excess of charm baryons over charm anti-baryons and an excess of charm anti-mesons over charm mesons. These phenomena are in fact observed in the data.

1.4 Scope of this Thesis

Using the data collected by the FOCUS experiment we performed an analysis of the pseudoscalar semileptonic decays $D^0 \to K^-\mu^+\nu$ and $D^0 \to \pi^-\mu^+\nu$. The fit to the data is accomplished through a binned maximum likelihood fit to two-dimensional distributions, either $D^{*+} - D^0$ mass difference vs. q^2 or $\cos\theta_l$ vs. q^2 where the free parameters are the signal and background yields. In addition we use a weighting technique in the

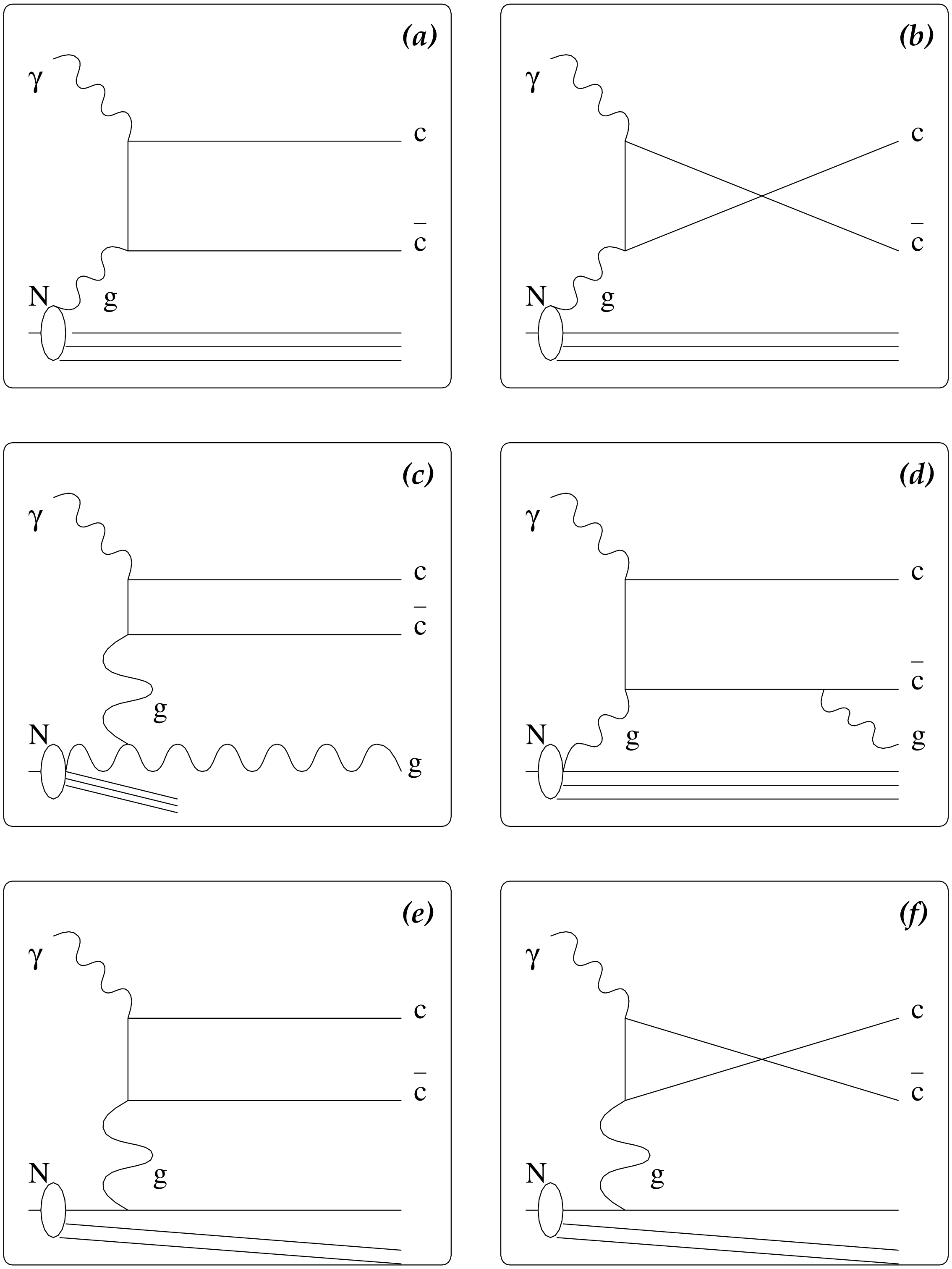

Figure 1.16: Contributions to the photon-gluon fusion process. The photon from the beam interacts with a gluon from the target creating a $c\bar{c}$ pair.

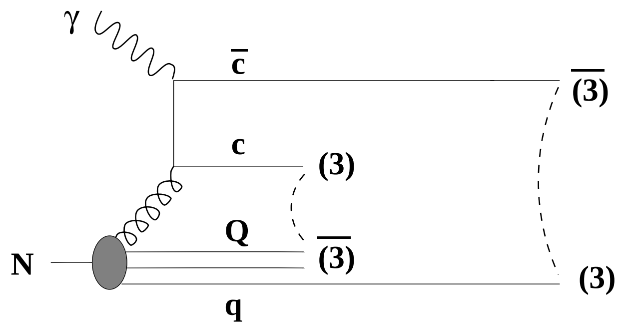

Figure 1.17: In associated charm production the charm quark dresses with the di-quark while the anti-charm quark binds to the remaining quark creating an asymmetry in the particle-antiparticle momentum spectra as well as in the number of meson (baryon) particles and meson (baryon) anti-particles.

fitting process to report a model dependent measurement of the q^2 dependence for the Cabibbo favored and the Cabibbo suppressed modes. Since the efficiency tends to have a non-negligible q^2 dependence, the weighted Monte Carlo distributions are used to recompute the efficiency at each fit iteration. From the fitted yields and efficiencies, we report a new measurement of the branching ratio of the Cabibbo suppressed mode relative to the Cabibbo favored mode. From the relative branching ratio $\Gamma(\pi^-\mu^+\nu)/\Gamma(K^-\mu^+\nu)$ we are also able to compute the form factor ratio $f_+^\pi(0)/f_+^K(0)$ through a numerical integration of the differential decay rate modulated by the reconstruction efficiency as a function of q^2. We compare this result to recent SU(3) symmetry breaking predictions.

In the parametric analysis of the q^2 dependence, the two models that we consider are the standard pole dominance form:

$$f_+^{K,\pi}(q^2) = \frac{f_+^{K,\pi}(0)}{1 - \frac{q^2}{M_{pole}^2}} \tag{1.11}$$

for which we measure M_{pole}, and the modified pole form:

$$f_+^{K,\pi}(q^2) = \frac{f_+^{K,\pi}(0)}{(1 - \frac{q^2}{M_{D^*,D_s^*}^2})(1 - \alpha\frac{q^2}{M_{D^*,D_s^*}^2})} \tag{1.12}$$

for which we determine the parameter α that measures the contribution from higher states to the first pole. Further, given the large yield in the Cabibbo allowed mode $D^0 \to K^-\mu^+\nu$, we report a measurement of the helicity suppressed contribution $f_-^K(0)/f_+^K(0)$.

In the last part of the thesis we present a model independent measurement of the q^2 dependence of the form factor $f_+(q^2)$ for the high statistics mode $D^0 \to K^-\mu^+\nu$. We make use of the parametric analysis fit to extract the signal yield in bins of q^2. Then, we apply a method to deconvolve the smearing effects due to experimental resolution. This is achieved by implementation of the so called deconvolution matrix which relies on our Monte Carlo simulation.

Our results will be compared to other experimental measurements as well as the theoretical predictions. Many recent theoretical approaches provide predictions of the form factors for heavy to light quark transitions including contributions of the helicity suppressed form factor $f_-(q^2)$ [9, 10, 11]. In particular we will show that a new Lattice QCD calculation in the unquenched approximation compares well with our result for the form factor ratio $f_+^\pi(0)/f_+^K(0)$.

Chapter 2

The Photon Beam

The FOCUS experiment collected data produced by the interaction of a photon beam on a BeO target. This chapter describes how the final photon beam was produced. After a brief introduction of the Tevatron collider, which accelerates protons to energies of about 800 GeV we will discuss the multi-step process that leads to a clean sample of photons with a central energy of about 175 GeV.

2.1 The Tevatron Proton Beam

The layout of the Fermi National Accelerator Laboratory (FNAL) is shown in Fig. 2.1. During 1996-97, the Tevatron supplied the beams for the fixed target experiments and during this period the FOCUS collaboration collected a large sample of charm decays.

To obtain the 800 GeV proton beam the Fermilab facility uses a $750,000$ eV Cockcroft-Walton gap to accelerate ions consisting of two electrons and one proton. These ions are then injected into a 500 feet long linear accelerator (LINAC) with an energy of 750 keV. In the LINAC, radio-frequency cavities accelerate these ions to an energy of 400 MeV. This relatively energetic beam passes through a carbon foil that strips off the electrons, and the remaining protons are injected into the Booster.

The Booster is a synchrotron accelerator with a diameter of about 500 ft and located about 20 feet below ground. Protons are cycled thousands of times using dipole

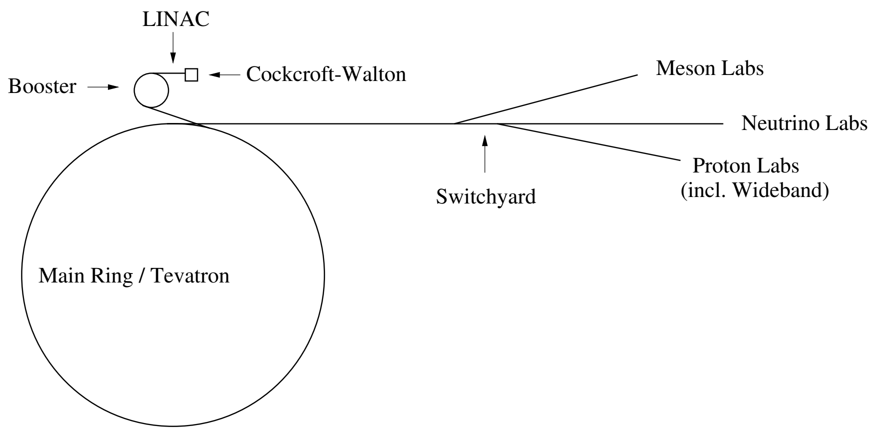

Figure 2.1: Schematic layout of the accelerator at the Fermilab facility.

magnets to bend the beam and an RF cavity to accelerate the protons until they reach an energy of 8 GeV. Each bunch of protons is then injected in the Main Ring.

Like the Booster, the Main Ring is a synchrotron accelerator and it accelerates protons to an energy of 150 GeV. The protons are finally injected into the Tevatron.

The Tevatron has a circumference of about 4 miles and it uses superconducting, liquid helium, dipole magnets to bend the proton beam. Within the Tevatron, the protons reach an energy near the TeV. Further, the Tevatron operates with a repeating cycle of beam acceleration and beam extraction. The acceleration process takes about 40 sec and is followed by a 20 sec extraction period (spill) that guarantees a long-duration beam of uniform intensity to the fixed target experiment areas.

Three different areas ("Proton," "Neutrino," and "Meson") receive the Tevatron beam through a series of electrostatic devices and specialized extraction magnets. The FOCUS experiment was located at the end of the Wideband Photon Beam line in the Proton area. Approximately 4.5×10^{12} protons/spill were delivered to Wideband.

2.2 The Wideband Photon Beam Line

The advantage of using a photon beam instead of a hadron beam is that the charm photoproduction cross section to the photon total hadronic cross section is three to five times larger than the hadron charm cross section to the hadron total cross section. This significantly reduces the hadronic background in the data. The disadvantage of the photon beam is the large electromagnetic background. This background can be greatly suppressed by using an hadronic trigger.

The multi-step process that produces a usable photon beam for the FOCUS experiment is shown in Fig. 2.2. The 800 GeV protons from the Tevatron interact with a 1.6 m long cryogenically cooled liquid deuterium target. The products of these interactions contain π^0 particles which decay electromagnetically ($\tau \sim 10^{-16}$ sec.) into two photons. The "production target" material was chosen with a A/Z^2 ratio that maximizes the number of strong interactions (high hadronic cross section) while minimizing the photon reabsorption. The charged particles produced in the interaction are immediately swept away by dipole magnets while the neutral particles strike a photon converter consisting of a 0.5 radiation length lead sheet. Photons are converted to electron/positron pairs. A beam dump downstream of the converter absorbs the uninteracted neutral hadrons while the electron-positron pairs are focused by quadrapole magnets into two beams ("double bands") and directed around the beam dump. The electron/positron beams are selected by collimators and magnets to have nominal momentum of 300 GeV/c with a momentum spread of $\pm 15\%$. The main sources of contamination in the electron/positron beams are hadrons from Λ^0 decays which account for about 4% of the triggered events and some muons from the production target. The two beams are recombined by dipole magnets and the resulting beam is re-focused (so that it would impact the experimental target if unimpeded) on a lead radiator that consists of 20% of a radiation length. Photons are produced by the interaction of the beam on the radiator through the bremsstrahlung process. The recoil beams of electrons and positrons are than deflected toward two (electron/positron) calorimeters. The mean energy of the bremsstrahlung photons is 175 GeV.

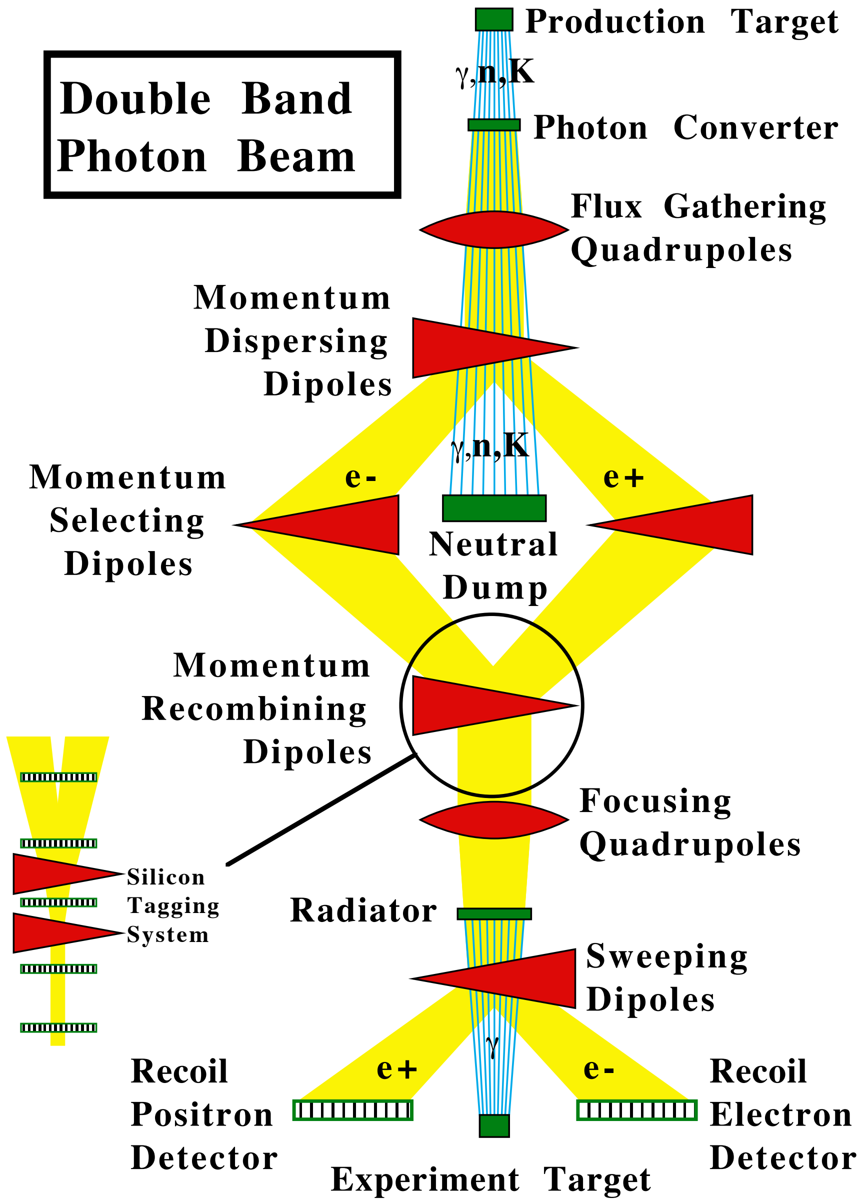

Figure 2.2: Schematic overview of the FOCUS beam line.

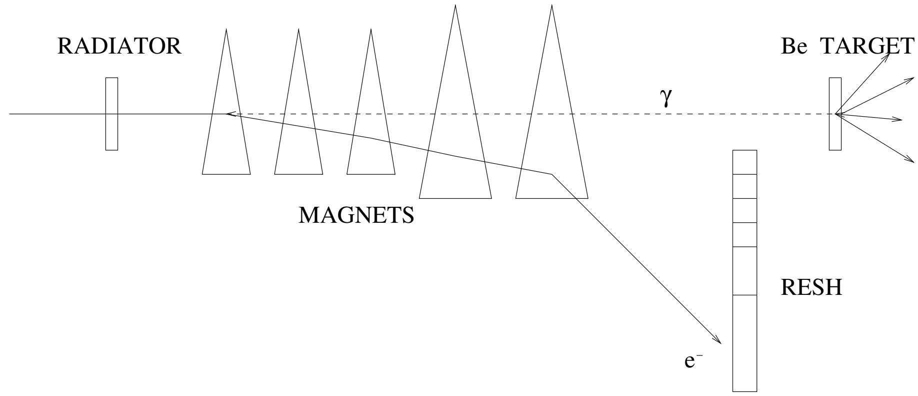

Figure 2.3: Schematic view of the beam tagging system. Electrons and positrons are deflected into the RESH (shown) and POSH (not shown). Noninteracting photons strike the Beam Gamma Monitor calorimeter.

2.3 Beam Tagging System

Information about the energy of the incident photon is provided by the beam tagging system [13] shown in Fig. 2.3. The energy E_γ of the photon is computed by measuring the energy E_i of the incident electron before the radiator, the energy E_f of the recoil electron after the radiator and the energy $E_{\rm non}$ deposited in the Beam Gamma Monitor (BGM) calorimeter which measures the energy of additional photons that do not interact with the experimental target:

$$E_\gamma = E_i - E_f - E_{\rm non}$$

We need to measure $E_{\rm non}$ because we always have a soft secondary photon in the bremsstrahlung process. The BGM is located in the middle of the FOCUS spectrometer. The Recoil Electron/Positron Shower Calorimeters measure the energy E_f of the electron after the radiator. These calorimeters each consist of 13 counters with horizontal segmentation to measure both the bend angle of the electron and the energy from the electromagnetic shower.

Chapter 3

The FOCUS Spectrometer

In this chapter we describe the FOCUS spectrometer starting from the experimental target and continuing to a description of the detectors as they exist the beam line (see Fig. 3.1).

The FOCUS spectrometer is an upgrade of the E687 experiment which is described in reference [14]. It is a large aperture, multiparticle forward spectrometer with two dipole magnets. The magnets are run at opposite polarity to focus the electron/positron pairs at the BGM. As the pairs are predominantly produced at zero degrees, they are contained in a narrow gap horizontally.

The tracking of charged particles is provided by a system of silicon strip and a system of multi-wire proportional chambers. Three Čerenkov counters and two muon detectors are responsible for particle identification. Finally, the FOCUS spectrometer is equipped with one hadronic calorimeter and two electromagnetic calorimeters. The chapter ends with a description of the trigger and the data acquisition systems.

3.1 The Experimental Target

The incoming photons interact in a Beryllium Oxide (BeO) target through a photon-gluon process that produces the charm-charmbar pairs. The material for the target was chosen to minimize electron/positron pair production and particle re-interactions. Since charm particles are relatively long lived, the decays are identified by requiring a

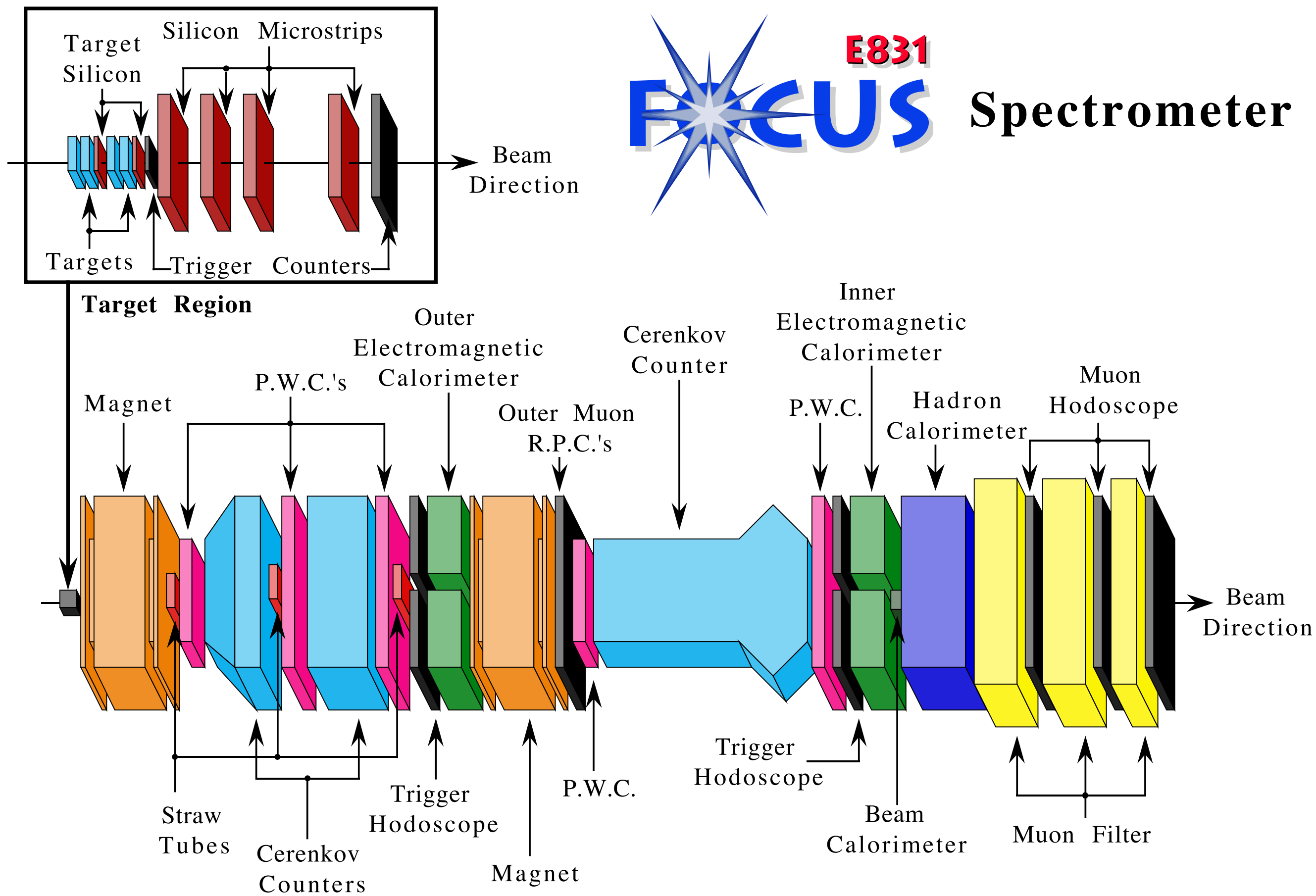

Figure 3.1: Layout of the FOCUS spectrometer.

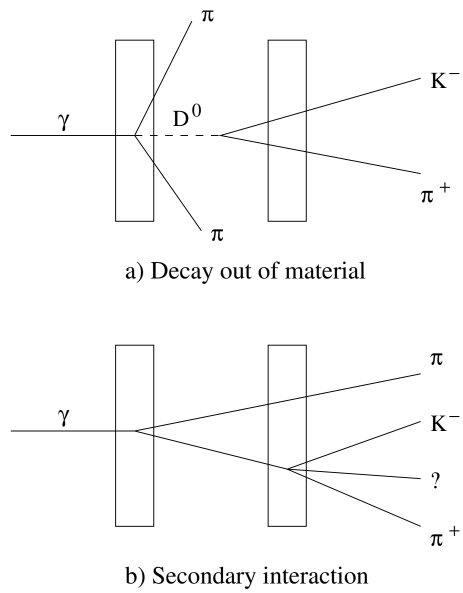

Figure 3.2: a) Decay of a D^0 particle to the final state $K^-\pi^+$. The decay occurs out of the target material. b) Example of background from re-interaction of particles coming from the the interaction vertex.

separation between production and decay vertices. Secondary vertices identified outside of the target material are predominantly due to particle decays. Therefore to reduce the amount of confusion generated from secondary interactions of non-charm particles (Fig. 3.2), the number of charm decays outside the material was enhanced by implementing a segmented target. Further, the high A/Z^2 ratio of the beryllium oxide allows each segment to be thin increasing the number of decays in air.

Each segment of the target has an area of 25.4 mm^2 and a thickness of 6.75 mm. Further, each target segment is followed by a 10 mm decay region. In Fig. 3.3 the location of primary and secondary vertices is shown for the charm meson decay $D^0 \to K^-\pi^+$.

3.2 The Silicon Microstrip Detector

The main problem with a segmented target is that it extends the target region in length. If the detection of the tracks is performed downstream of the target, the spatial

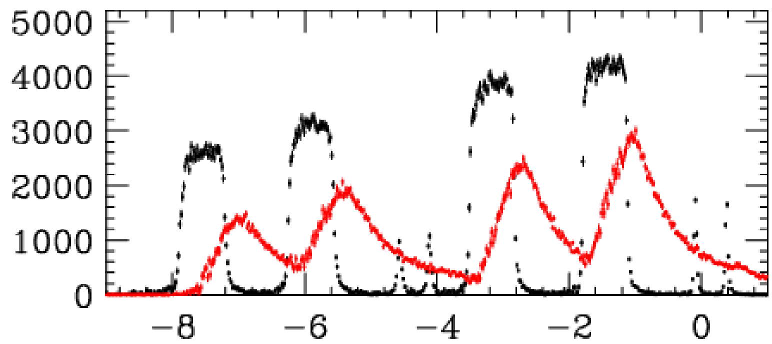

Figure 3.3: Location of primary (black) and secondary (red) for golden mode decays. The primary vertex locations correspond to the position where the target material and the TSSD planes are located. Most of the decay vertices occur outside of this material. Note that the efficiency drops off as the primary vertex is upstream.

resolution of the vertices is degraded as the decay occurs more and more upstream. This can be avoided by adding additional silicon strip detectors inside the target region. For about 2/3 of the run, a silicon microstrip detector (TSSD's) was embedded within the target segments [15]. The TSSD was arranged in two views with an orientation of $\pm 45°$ relative to the horizontal. Each view consists of 1024 strips 25 μm wide and 50 mm long forming a total area of 25×50 mm^2. Four additional microstrip stations are positioned downstream of the first trigger counter (TR1). Each station has three views with each view separated at a distance of 5 mm and forming angles of -135°, -45° and -90° with the horizontal. The first three stations are separated by 6 cm while the last is separated by 12 cm. Each view has two regions with different strip pitch. The inner and outer regions of the first station have a spacing of 25 μm and 50 μm respectively, while the other three stations have 50 μm and 100 μm spacing in the two regions. Charged particles passing through this detector ionize the material inducing a current which is amplified and digitized. A schematic overview of the target region is shown in Fig. 3.4.

This device provides excellent spatial and proper time resolution. We can compute an estimate of the improvement in the experimental resolution base on the argument that for a particle with lifetime τ, the decay rate satisfy the relation:

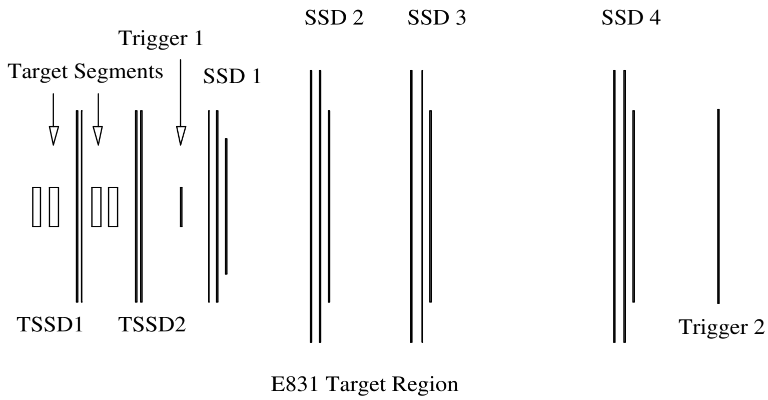

Figure 3.4: Schematic overview of the FOCUS target silicon region.

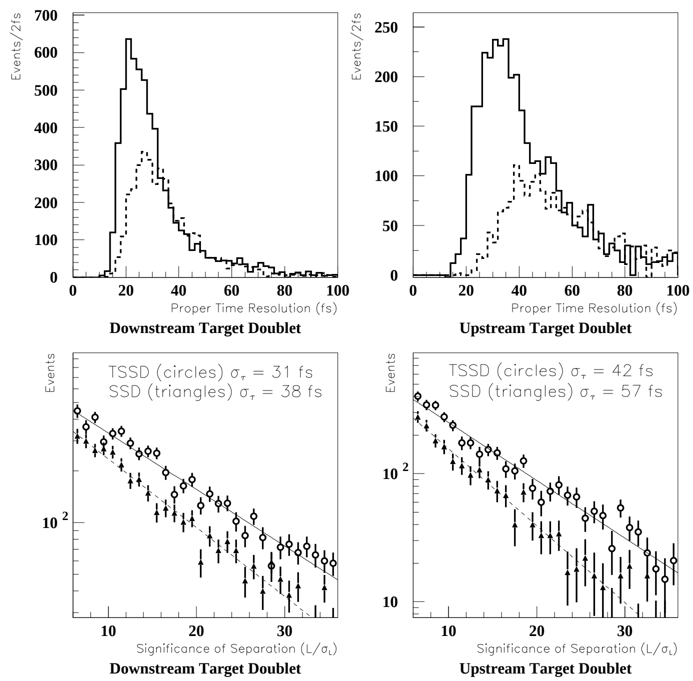

Figure 3.5: Proper time resolution for the decay $D^0 \rightarrow K^-\pi^+$. The data is split into events from the most downstream (left column) and the most upstream (right column) pair of BeO segments. Top plots: comparison in the proper time resolution when the target silicon information is included (solid line) and when this information is not included (dashed line). Using the target silicon the fraction of events with good resolution increases. Bottom plots: we show the fit to the number of events as a function of L/σ_L. The TSSD improves the proper time resolution significantly.

$$N_0 \exp\left(-t/\tau\right) = N_0 \exp\left[(\sigma_t/\tau)(-L/\sigma_L)\right]$$

where t (σ_t) is the proper time (proper time resolution) and L (σ_L) is the decay length (decay length resolution). By making an exponential fit to the yields as a function of the primary and secondary vertices separation L/σ_L, we can infer the proper time resolution. In Fig. 3.5 we show the fit for the decay $D^0 \rightarrow K^-\pi^+$, the resolution improves by 35% when the information from the target silicon detector is included.

3.3 Multiwire Proportional Chambers

Five multiwire proportional chambers (PWC) are implemented in the FOCUS spectrometer. Chambers P0, P1 and P2 are located between the two analysis magnets. Chambers P3 and P4 are positioned downstream of M2. Each chamber is provided with four planes organized in x (vertical wires) and y (horizontal wires) views and in two "stereo" views called u and v forming an angle of $\pm$ 11.3° with the horizontal (Fig. 3.6). These views are used to resolve ambiguities. The angle of 11.3° was chosen to provide additional information in the bending (y) view. Each charged track is classified according to the number of chambers in which the hits are observed. Outer tracks that don't leave hits in P3 or P4 are called "stubs" while inner tracks that leave hits in all the chambers are called "5-chamber" tracks.

These chambers are built from alternating planes of high voltage wires and grounded sense wires. The planes P1, P2 and P4 have a maximum area of 60×90 in^2 and are separated by a few millimeters. The voltage difference between the wires is about 3 kV. The chambers are filled with gas selected on the basis of its ionizing properties. All chambers use a gas mixture of 75% argon and 25% ethane. Particles passing through the chamber ionize the gas; the electrons liberated are accelerated by the voltage difference toward the grounded sense wires inducing further ionization of the gas that in turn causes a cascade of electrons. A hit is recorded when the electric current passes a certain threshold. Chambers P0 and P3 are sized to match the magnet apertures. These chambers have shorter wires and operate at higher voltage. Chambers P1, P2 and P4 are larger, have wider spacing and operate at a lower voltage.

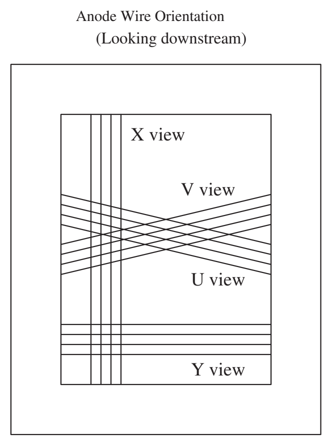

Figure 3.6: The four views of the PWC chambers.

3.4 The Straw Tubes

The straw tube wire chambers were positioned in the high flux electron/positron pair region as an additional source of information in the case that the PWC system needed to be deadened in this region. While this system worked well and data was read out, this information was not used in the track reconstruction.

3.5 Dipole Magnets

Two magnets with opposite polarity are used to determine the charged particle momentum. The first magnet is located downstream of the SSD system while the second is positioned near the middle of the spectrometer. Both magnets bend the

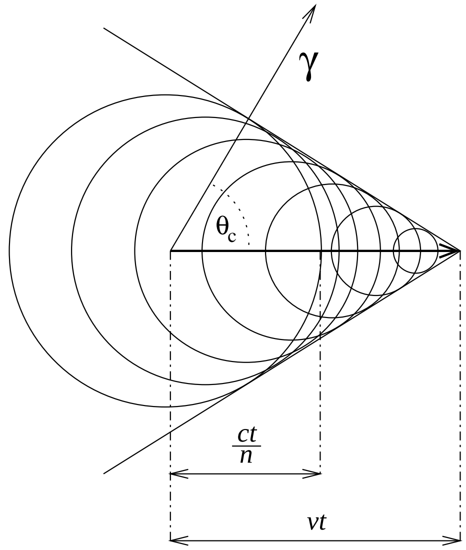

Figure 3.7: The Čerenkov cone depends on the index of refraction of the medium and the speed of the particle.

charged particles along the y direction. M1 operates at 1020 amps providing a transverse momentum kick of 0.4 GeV/c while M2 operates at 2000 amps and provides a kick of 0.836 GeV/c allowing the electron-positron pairs, produced at the target, to be refocused onto the BGM calorimeter.

3.6 Čerenkov Counters

The FOCUS spectrometer is equipped with three multi-cell threshold Čerenkov counters [16] with sufficient spatial resolution to link the Čerenkov signal to individual tracks. The signal is produced by emission of light of charged particles traveling through the material with a speed higher than the speed of light in the same material. If n is the index of refraction of the material, the condition for a particle to create Čerenkov light is given by:

$$\beta = \frac{p}{E} = \frac{p}{\sqrt{p^2 + m^2}} \geq \frac{1}{n}$$

from which we can extract the Čerenkov threshold for the particle momentum:

Detector	Gas	Threshold (GeV/c)		
		π	K	p
C1	58% He/42% N_2	8.5	29.9	56.8
C2	N_2O	4.5	16.2	30.9
C3	He	17.0	61.0	116.2

Table 3.1: Gases and threshold momenta of the three Čerenkov detectors.

$$p_{thresh} = \frac{m}{\sqrt{n^2 - 1}}.$$

The half-angle of light emission is shown in Fig. 3.7 and is given by:

$$\theta = \cos^{-1} \frac{1}{n\beta}$$

Given the momentum of a particle measured in the tracking system and the intensity of the associated light measured in the Čerenkov counter, we compute the probability for a mass hypothesis of the particle. In FOCUS it is possible to discriminate between electrons, pions, kaons and protons over a wide range of momentum (Table 3.1).

C1: The first counter C1 is located between the multiwire chambers P0 and P1 and uses a mixture of 58% helium and 42% nitrogen resulting in a pion threshold of 8.5 GeV/c. It has a xy cross section of 50 $\times$ 80 in^2. It consists of 90 cells, split between into an inner and outer regions. The inner part uses planar mirrors that reflect the light onto Winston cones which concentrate the light onto 50 photo-multiplier tubes (PMT's). The outer portion has spherical mirrors that focus the Cerenkov light onto 40 PMT's.

C2: This counter is located between P1 and P2 and operates using nitrous oxide gas (N_2O) with a pion threshold of 4.5 GeV/c. It has an xy dimension of 64 $\times$ 100 in^2 and it consists of 110 cells divided into inner and outer regions analogous to C1.

C3: This detector is located between P3 and P4 and uses helium gas for a pion threshold of 17 GeV/c, has a transverse xy area of 60 $\times$ 93 in^2, and consists of 100 cells

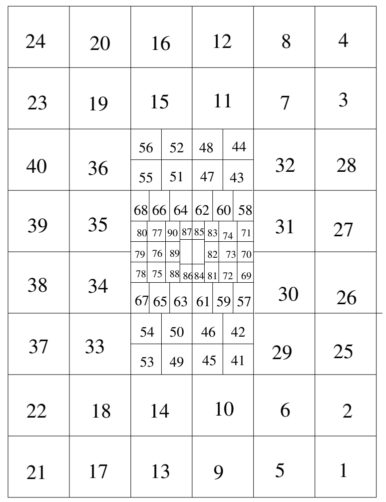

(a) C1. Cells 1–40 use spherical mirrors, 41–90 use planar mirrors.

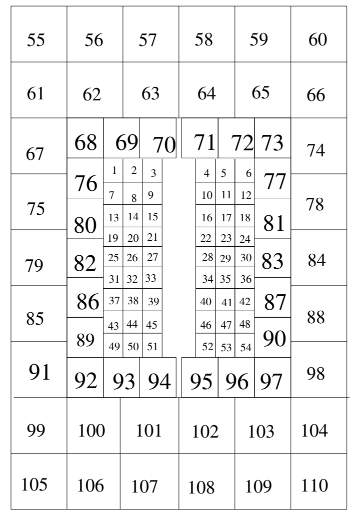

(b) C2. Cells 1–54 use planar mirrors, 55–110 use spherical mirrors.

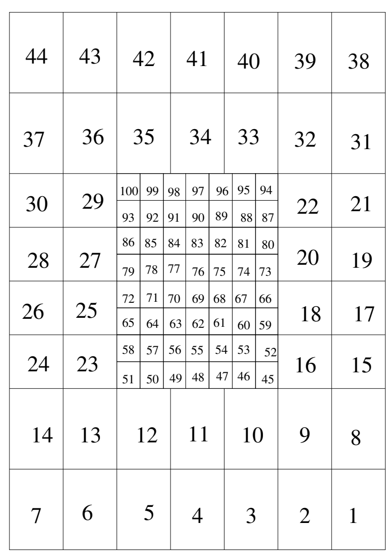

(c) C3. All cells use spherical mirrors.

Figure 3.8: The arrangement of the light gathering cells for the three Čerenkov counters, C1, C2, and C3.

which use spherical mirrors to focus light onto photomultiplier tubes.

3.7 Electromagnetic Calorimeters

Calorimeters provide information about the energy of a particle (charged or not). FOCUS uses two types of electromagnetic calorimeters: a sampling calorimeter made with alternating layers of absorber and scintillating material and an lead glass integrated calorimeter which detects the charged particles through emission of Čerenkov light.

3.7.1 The Inner Electromagnetic Calorimeters

The inner electromagnetic calorimeter (IE) [17] is built from about 802 lead glass blocks arranged in a tower geometry. Each block has a transverse dimensions 5.8×5.8 cm^2 and a depth of 60.2 cm equivalent to 18.75 radiation lengths or 2.2 proton interaction lengths. There are two sides to the detector with a central gap to allow the passage of the intense beam of non-interacting photons and converted electron/positron pairs. Each block is wrapped with aluminized mylar to reflect light back into the block. Photomultiplier tubes detect the light at the back of each block. In Fig. 3.9, the beam's eye view of the detector is presented. This device is used in the trigger logic with three types of inputs: the sum of the total IE energy, the sum of the transverse energy, and a two-body trigger to select $J/\psi \rightarrow e^+e^-$ decays.

3.7.2 The Outer Electromagnetic Calorimeters

The Outer Electromagnetic calorimeter (OE) is located before M2 with an opening of 55×88 cm^2 and an overall size of 255×205 cm^2 with a vertical gap in the pair region. The OE measures energy for tracks at a large angle relative to the beam-line [18]. It is a sampling calorimeter and is built with alternate layers of lead and plastic scintillator. There are 23 layers of 3.1 in scintillators organized in four (x, y, u and v) orientations. The u and v planes form an angle of 45° with the horizontal. To further

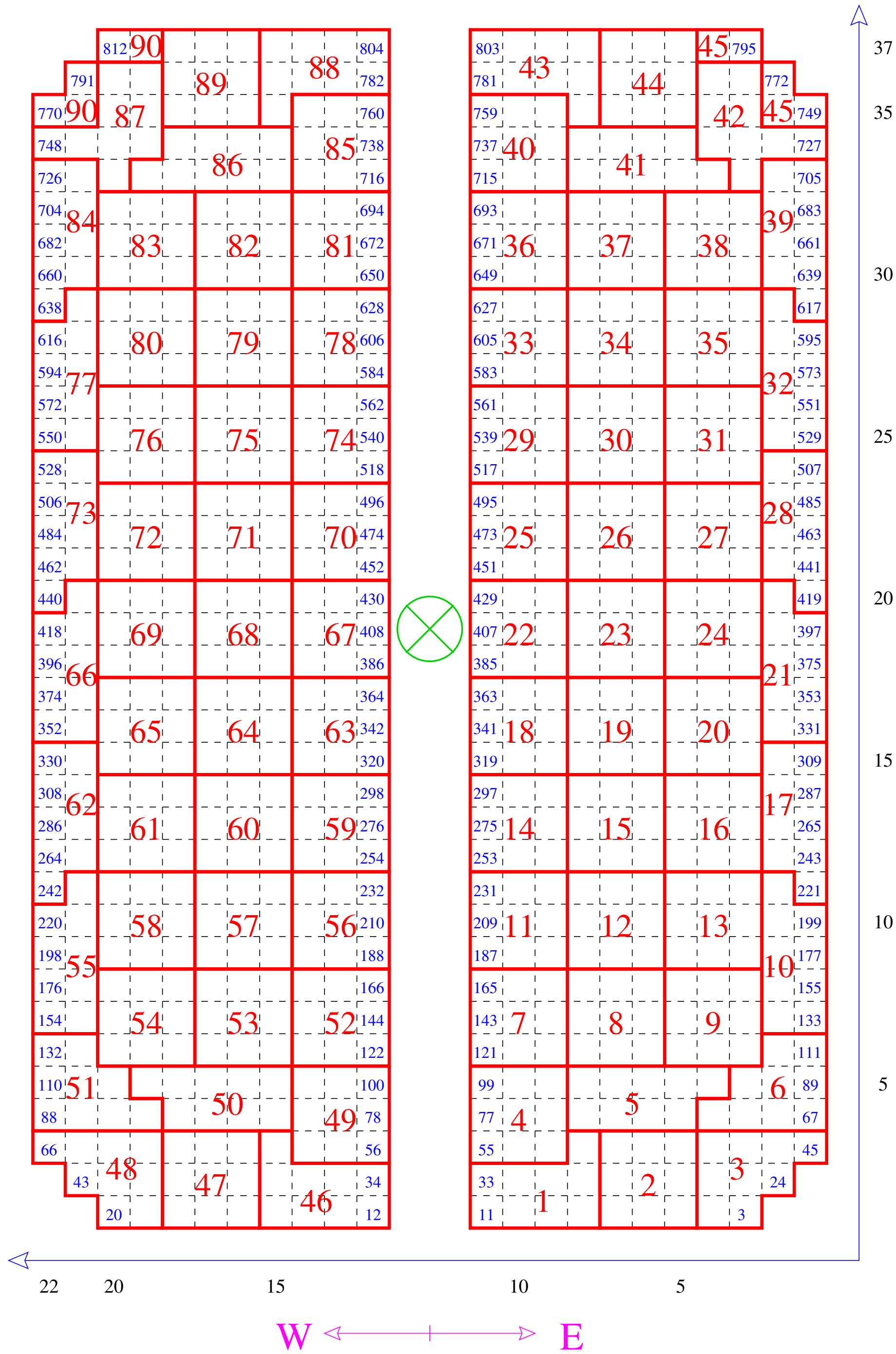

Figure 3.9: Front view of the inner electromagnetic calorimeter.

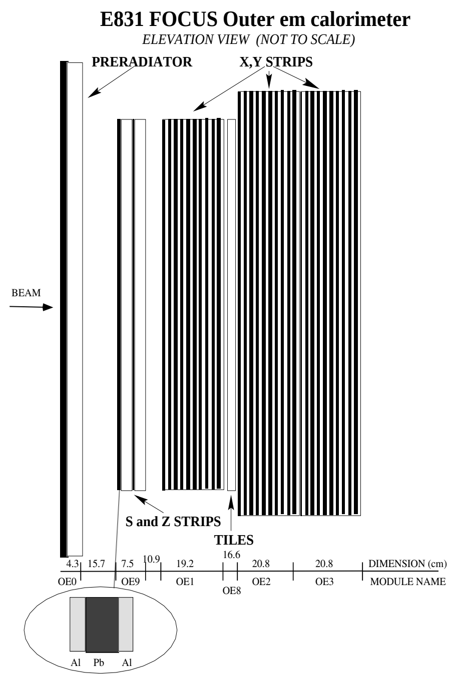

(a) Outer electromagnetic calorimeter layout

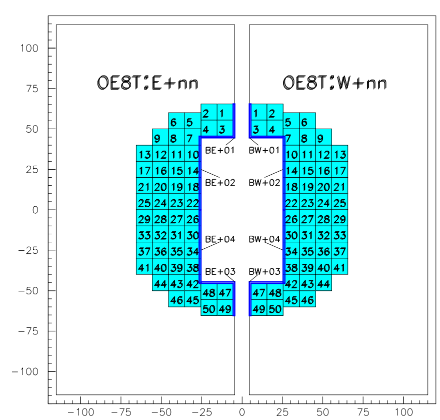

(b) Outer electromagnetic calorimeter layout

Figure 3.10: A schematic of the outer electromagnetic calorimeter.

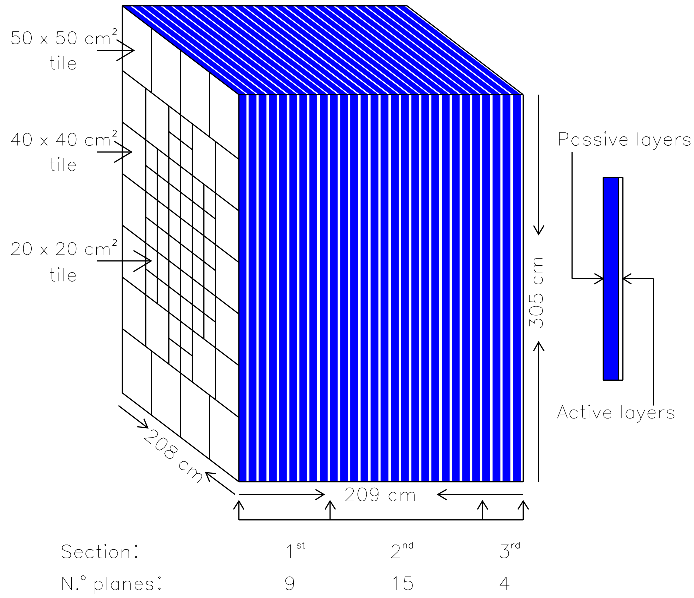

Figure 3.11: Hadron Calorimeter layout.

resolve ambiguities, there is a single layer of 100 scintillator tiles located in the high flux (inner) region. The side and front views of the OE detector are shown in Fig. 3.10.

3.8 The Hadron Calorimeters

The detection of neutral hadrons is accomplished by the Hadron Calorimeter (HC) located downstream of the IE [19]. Like the outer electromagnetic calorimeter, the HC is a sampling calorimeter with 28 alternating layers of scintillators and steel for a total of 7.8 interaction lengths and 72.7 radiation lengths. The HC measures 255 $\times$ 205 cm^2 in the xy cross section and 209 cm in depth. The layers measure 4.4 cm in thickness. The scintillator is subdivided into 66 towers segmented in three sections as illustrated in Fig. 3.11. To achieve better resolution, the inner region is equipped with 20 $\times$ 20 cm^2 tiles while the outer region has 40 $\times$ 40 cm^2 and 50 $\times$ 50 cm^2 tiles. The layers are grouped into three sections in which the corresponding tiles are optically combined by optical fibers. The readout consists of a total of 198 channels for the entire HC. The HC is used at the level-one trigger. The summed energy has to exceed a 20 GeV threshold.

3.9 The Muon Detectors

Given the highly penetrating behavior of muons compared to electrons and hadrons, the muon detection is accomplished by searching for particles that survive after passing through a thick layer of absorbing material. The spectrometer is equipped with an inner muon detector located at the end of the spectrometer and an outer muon detector located downstream of M2.

The Inner Muon: An array of scintillators called muon hodoscopes (MH) [21] is used to detect muons at a small angles relative to the beam line. The MH hodoscopes are arranged in three stations separated by steel filters as shown in Fig. 3.12.

The three filters are 61 cm, 129 cm and 68 cm thick for a total of 15 hadronic interaction lengths. The HC which is located just upstream of the inner muon system provides an additional 126 cm of steel.
Each station has two views: MH1 and MH2 have x and y views while MH3 has u and v views oriented at 30° relative to the horizontal. The widths of the scintillator strips increases for stations further downstream to account for multiple Coulomb scattering of particles that travel through more material. The strip width is 5 cm, 8 cm, and 10 cm for MH1, MH2, and MH3, respectively.

The Outer Muon: This detector is located just downstream of second analysis magnet to detect tracks at large angles that pass through the material provided by the outer electromagnetic calorimeter and M2. Resistive plate chambers were used for this detector due to the presence of the magnetic field from M2 and due to the confined space available [22]. The RPC's are double gap modules (Fig. 3.13) which operate at a high voltage (5.8 kV) applied to graphite coated bakelite across a gap filled with a gas mixture of 5% freon, 8% isobutane, 16% CO_2 and 71% argon. The system provides complete coverage and some redundancy.

The 24 RPC modules were assembled in three views with eight RPC's in each

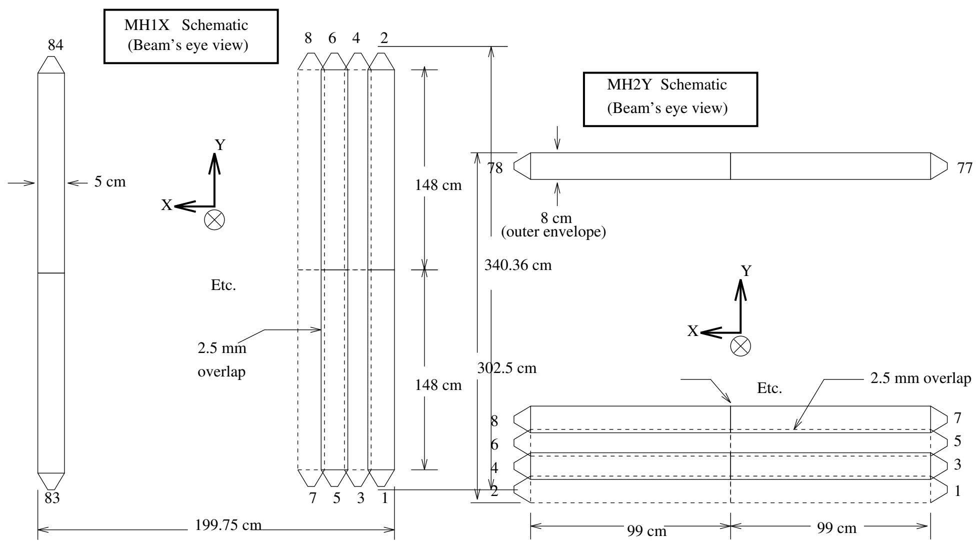

(a) MH1X. The arrangement of MH2X is similar.

(b) MH2Y. The arrangement of MH1Y is similar.

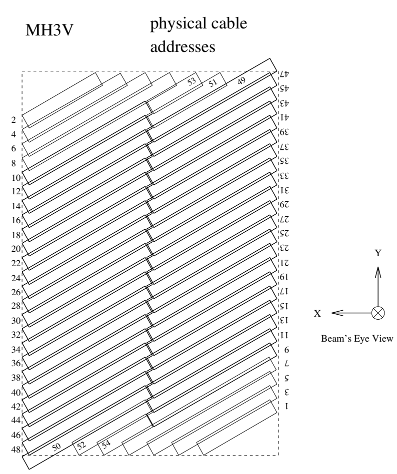

(c) MH3V. MH3U is identical except the counters are rotated by 90°.

Figure 3.12: Views showing the counter arrangements of the Inner Muon Hodoscope arrays.

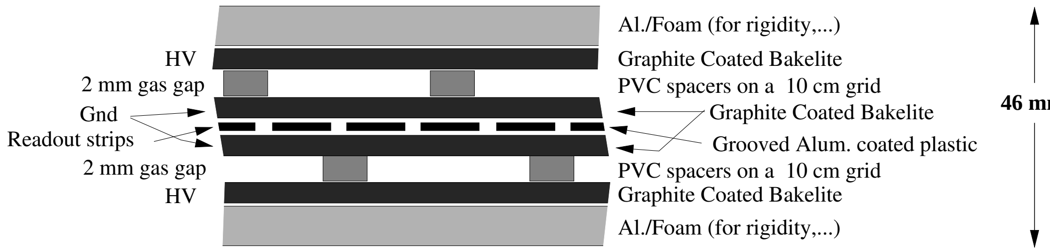

Figure 3.13: RPC modules cross section.

view. Each module measures 1.0×1.6 m^2 or 1.0×1.8 m^2. The readout strips are located between the bakelite modules and are 2.9 cm wide. The x view plane has two sets of vertical strips, each covering half of the RPC module. The y view has one set of horizontal strips covering the full width of the module. The u view has one set of strips at 45° that cover the full module. Modules from the three views that are aligned in the z direction define a "tower". Two out of three modules in a tower have to fire to assign the muon identification to a track.

3.10 The trigger

A hadronic trigger is required to reject the dominant component of electromagnetic background. From a typical (20 sec) spill containing about 10^8 interactions, FOCUS triggered on about 30×10^3 interactions, about 95% hadronic. The full list of the separate trigger signals are shown in Table 3.2.

The trigger operates at two levels: a master gate level with a fast (200 ns) trigger which initiates the data readout process for most detector elements and a second level trigger that decides in 1.2 μs whether the readout should be completed. If the second level trigger rejects the event, a 1 μs clear cycle resets the readout electronics. Once the event is accepted, the readout process is completed in about 110 μs depending on the event. The combined triggers form the Master Gate and the second level trigger are summarized in Table 3.3 and Table 3.4, respectively.

Scintillating Hodoscopes: TR1 is a single scintillating plane located between

Table 3.2: Summary of FOCUS triggers.

Trigger	Description
TR1	Interaction in target
TR2	Confirms hit in target
OH_1	At least one outer particle
$(H\times V)_1$	At least one inner particle
$(H\times V)_2$	At least two inner particle
IE_2	At least two hits in the IE
IM_1	At least one hit in the IM
IM_2	At least two hits in the IM
OM_1	At least one hit in the OM
OM_2	At least two hits in the OM
E_{HI}	Hadronic energy sum over a high threshold
E_{LO}	Hadronic energy sum over a low threshold
E_{IE}	Electromagnetic energy sum over threshold
E_{IE2}	Improved electromagnetic energy sum
$MULT_n$	Enough PWC hits for at least n tracks
AM·AMD	Halo muons veto
IM(E+W)	Hits in both halves of IM triggers (veto)

Table 3.3: The FOCUS Master Gates. Master Gates denoted (PS) are prescaled and are used for calibration.

Trigger	Definition	Physics signal
MG1	TR1 · TR2 · 2B ·E_{HI}	Hadronic trigger
MG2	TR1·TR2·2B·IE_2	$J/\psi \to e^+e^-$
MG3	TR1·TR2·$[\mathrm{IM}_1 + \mathrm{OM}_1] \cdot E_{\mathrm{LO}}$	Semi-muonic decays
MG4	TR1·TR2·2B·$[\mathrm{IM}_2 + \mathrm{OM}_2 + \mathrm{IM}_1 \cdot \mathrm{OM}_1]$	$J/\psi \to \mu^+\mu^-$
MG5	TR1·TR2	e^+e^- pairs (PS)
MG6	TR1·TR2·2B	Two-body events (PS)
MG7	TR1·TR2·$[\mathrm{IM}_1 + \mathrm{OM}_1]$	One-muon events (PS)

the target silicon and the SSD's. A signal from TR1 indicates that there was an interaction in the experimental target. After the SSD's a set of four scintillating planes form the TR2 trigger element. Hits in TR2 ensure that the tracks went through the SSD's system.

The OH scintillator array is located upstream of the outer electromagnetic calorimeter and therefore it detects tracks that go out of acceptance before reaching the end of the spectrometer. The OH has an aperture that matches the aperture of the second analysis magnet and has a pair region gap.

To favor hadronic events (that have larger transverse momentum with respect to the electromagnetic background), FOCUS has a wide angle requirement in the trigger. This is achieved using HxV arrays read out horizontally and vertically. The HxV array is located after the last PWC plane and in front of the IE. The HxV array has a vertical gap to allow electron/positron pairs through. This detector provides two triggers for one and two charged particles respectively. The information from the OH array and the HxV array (Fig. 3.12) is combined to make the two body requirement:

$$2B = (H \times V)_2 \ \mathbf{OR} \ [(H \times V)_1 \ \mathbf{AND} \ OH_1]$$

This requirement demands at least two charged tracks in the inner region or a charged track in the inner region and an outer track in the outer region.

Table 3.4: A typical second level trigger set for FOCUS. The actual triggers changed occasionally, especially the di-muon triggers.

Trigger	Definition	Physics signal
TRIG1	MG1$\cdot E_{\text{IE-2}}\cdot$MULT4	Hadronic trigger
TRIG2	MG2 $\cdot$ (H$\times$V)$_2$ $\cdot E_{IE}$	$J/\psi \to e^+e^-$
TRIG4	MG4$\cdot$IM$_2$ $\cdot$ $(H \times V)_2$$\cdot$!(AM$\cdot$AMD)	J/ψ, inner only
TRIG5	MG5	Prescaled MG5
TRIG6	MG6	Prescaled MG6
TRIG8	MG1	Prescaled MG1
TRIG9	MG4$\cdot$OH$\cdot$OM$_2$$\cdot$MULT2$\cdot$!(AM$\cdot$AMD)	J/ψ, outer only
TRIG11	MG4$\cdot$IM$_1$$\cdot$OM$_1$$\cdot$MULT1$\cdot$ (H$\times$V)$_1$ $\cdot$ IM(E+W)	J/ψ, inner/outer

The trigger system is completed by IM1, a system of two planes of scintillators located just downstream of MH1 and IM2, a single plane of scintillators upstream of MH2. These two arrays are shown if Fig. 3.14. IM1 and IM2 use the same logic used in the HxV producing a trigger for a single inner muon and for at least two inner muons respectively.

3.11 Data Acquisition

A description of the Data Acquisition system (DAQ) in FOCUS can be found in Reference [23]. Each detector sends a signal that is digitized in the DAQ and written to tape. All the elements of the spectrometer are connected to a single RS-485 DAQ bus. The information on the bus is stored in a Dual Ported Memory system. This data is staged on an SGI workstation and written to tape. Approximately 30,000 events were saved per 20 second spill. The readout time required less than 100 μs and about 4 Kbytes per event were written to tape. The information from the detector elements is saved in self-contained records for each event.

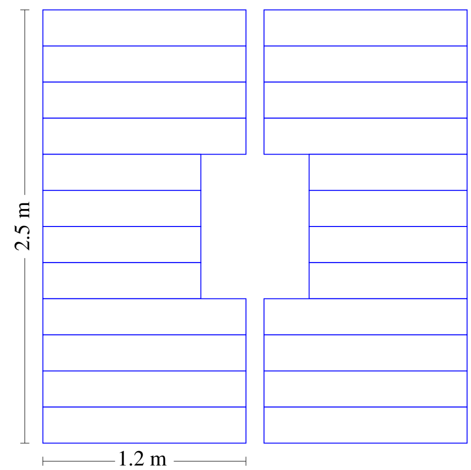

(a) The OH hodoscope arrays.

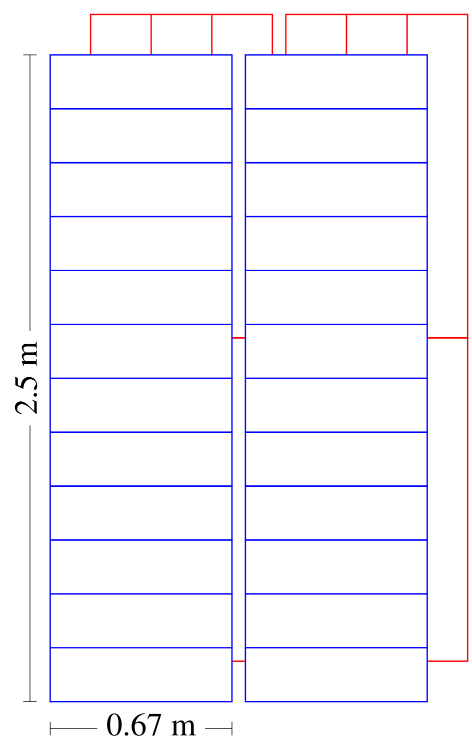

(b) The $(H \times V)$ hodoscope arrays.

Figure 3.14: OH and $(H \times V)$ hodoscope arrays.

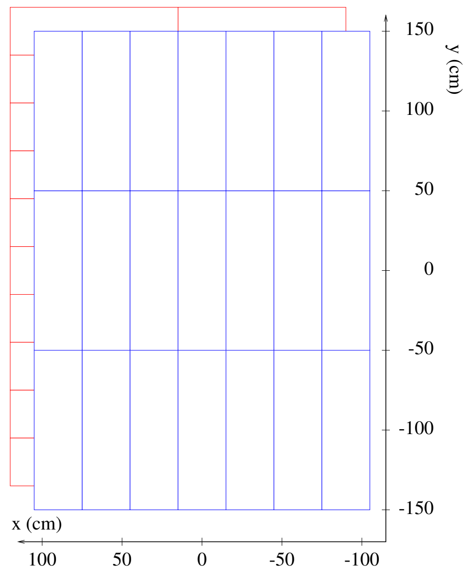

(a) The IM1V and IM1H arrays.

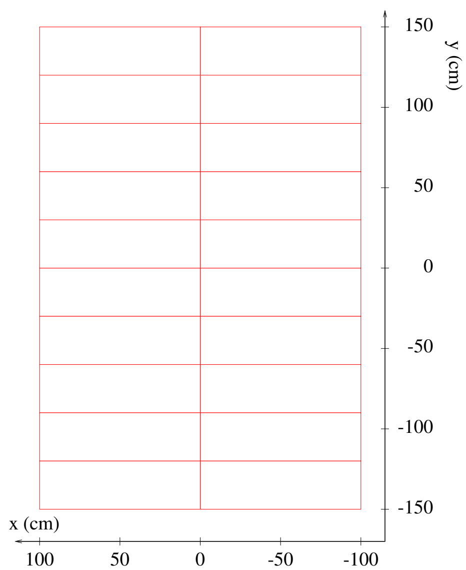

(b) The IM2H array.

Figure 3.15: The IM trigger counter arrays. a) IM1 has both horizontal and vertical scintillators arrays, b) IM2 has a single horizontal scintillator array.

Chapter 4

The Data Reconstruction

In this chapter we describe the algorithm used to reconstruct charm decays in FOCUS. We begin by describing the track reconstruction and momentum determination followed by an explanation of the main features of the Čerenkov identification algorithm. The central part of the chapter is dedicated to the reconstruction of particular categories of particle decays like vees, kinks, and hyperons. The chapter concludes with a description of energy reconstruction in the calorimeters and muon identification.

4.1 Tracking

The tracking algorithm uses information from both the SSD system and the PWC tracking chambers. Tracks in the two systems are reconstructed by applying a technique called "projection finding" in which hits in the different SSD or PWC stations are combined to look for clusters in all the available views. Later a "linking" process between the two detectors is performed to look for long-lived (compared to charm decays) charged particles.

4.1.1 SSD Track Reconstruction

The silicon microstrip detectors provide most of the information about vertexing. The reconstruction process is accomplished in three steps: the first step consists in finding a hit or a cluster of hits in each station and in identifying the center of each

hit. This is achieved using the information provided by the ADC's which convert the amount of charge deposited in the strips (through ionization of the material) into a digital pulse height. A pulse height weighting of the hits associated with the strips determines the impact point. This process is followed by a consistency check on the hypothesis that corresponding hits in different views match a straight line. Views in three out of four planes are required to have a $\chi^2/DOF < 3$ for this hypothesis. Only clusters in the middle SSD stations are allowed to be shared by multiple projections. Finally, the projections found in each view are combined into tracks. To satisfy the "track" requirement, these projections must have a $\chi^2/DOF < 8$. If more than one shared combination is found, the projection with the lowest χ^2/DOF is selected. It is possible to determine if one or two particles generated a hit by comparing the total ADC counts to the number expected for a Minimum Ionizing Particle (MIP). There is sufficient range in the ADC's to distinguish the passage of one MIP from two MIP's.
The reconstruction efficiency and resolution are functions of the momentum of the particle. In E687, the spatial resolution of a track in the inner region was:

$$
\begin{aligned}
\sigma_x &= 11.0\mu m \times \sqrt{1 + \left(\frac{17.5\ \ \mathrm{GeV/c}}{p}\right)^2} \\
\sigma_y &= 7.7\mu m \times \sqrt{1 + \left(\frac{25.0\ \ \mathrm{GeV/c}}{p}\right)^2},
\end{aligned}
$$

while in the outer (lower resolution) region it was about twice as large. In FOCUS a better resolution is achieved by using a pulse height sharing algorithm rather than a uniform averaging algorithm.

4.1.2 PWC Track Reconstruction

The FOCUS spectrometer is equipped with five Multiwire Proportional Chambers of which the first three are located between the first analysis magnet and the outer electromagnetic calorimeter, and the last two are located downstream of the second analysis magnet. The PWC tracks are reconstructed in a similar manner to the SSD, by finding and combining projections from different views. While the projection finding algorithm uses only PWC information in the y, u and v views, in the x (non bend) view, this process is seeded by extrapolation of SSD tracks to the PWC system. A search is made for PWC hits that match this seed projection. Once this process is over, unused hits in all the views are used to create new projections and new tracks.

Both "stub" and "5-chamber" tracks must have hits in at least three chambers with no more than four total missing hits and must have a maximum of two missing hits in a single chamber. Sub-categories such as kinks (tracks decaying into a charged and a neutral particle) and vees (neutral particles decaying into two charged daughters) have to satisfy less stringent selection criteria.

Once candidate tracks are found, a least squares fit is applied to compute slopes and intercepts in the xz and yz planes. Three chamber tracks pass through only one analysis magnet and they are fit to a single straight line. Tracks that produce hits in the 5 PWC stations are bent by M2 and therefore are fit to two lines. For this category of tracks, the momentum can be determined using only PWC information while 3-chamber tracks require the information from the SSD system. In each case corrections are applied to account for fringe fields and off-field components of the magnetic field. An iteration process is performed to account for these corrections until convergence is reached. In each event, a maximum of 30 PWC tracks and 600 PWC hits are allowed. About 3.5% of the data events reach this limit and are rejected.

4.1.3 Linking algorithm

A match is attempted between the tracks reconstructed in the SSD system and the tracks reconstructed in the PWC system. The match is performed by extrapolating the two tracks to the center of the first analysis magnet. If two PWC tracks match the same SSD track, a χ^2/DOF determines the best track hypothesis, although both candidates are saved. Only a maximum of two PWC tracks are allowed to be matched to one SSD track. Requiring that SSD tracks are singly linked in the PWC's can significantly reduce background from the conversion of photons into electron/positron pairs. Pairs are often reconstructed as a single track in the SSD system because of the small opening angle between the two tracks. These tracks are separated in the bending view by the first analysis magnet and are reconstructed as separate PWC tracks.

4.2 Momentum Determination

As discussed above, the momentum is determined by the deflection of tracks in the two analysis magnets, M1 and M2. An iterative process is applied to correct for the effects of the magnetic field extending beyond the magnet. Many factors determine how much a track direction will be changed by the magnet: slower tracks or tracks that enter the magnet with an angle will be affected more. In the same way, the daughters of vees or kinks that decay within the magnet will experience less magnetic field. An excellent understanding of the magnetic field map is required to reconstruct these states. The approximate momentum resolution for tracks whose momenta are determined by the two analysis magnets is:

$$\frac{\sigma_p}{p} = 0.034 \times \frac{p}{100\ \mathrm{GeV/c}} \times \sqrt{1 + \left(\frac{17\ \mathrm{GeV/c}}{p}\right)^2}$$

$$\frac{\sigma_p}{p} = 0.014 \times \frac{p}{100\ \mathrm{GeV/c}} \times \sqrt{1 + \left(\frac{23\ \mathrm{GeV/c}}{p}\right)^2}$$

for three chamber and five chamber tracks, respectively. Low momentum tracks have a momentum resolution dominated by multiple Coulomb scattering represented by the second term in the square root.

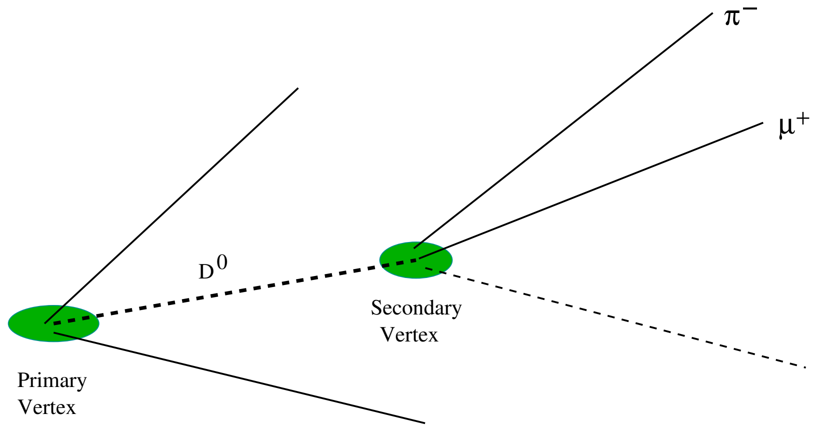

Figure 4.1: Event topology for a semileptonic decay.

4.3 Vertexing

The primary vertex is defined as the "point" where the photon from the beam interacts with the BeO target creating a charm-charmbar pair. The secondary vertex is defined as the point where the charm particle decays (Fig. 4.1). The longest lived charm particles, the D^+ ($\tau \sim 1040$ fs) and the D_s^+ ($\tau \sim 490$ fs) travel an average of 5 mm to 1 cm before decaying in the spectrometer and only rarely do they leave a hit in the TSSD's. This means that primary and secondary vertices must be inferred by the products of the charm decay or from other tracks in the target region. A vertex with n tracks is found by minimization of a χ^2:

$$\chi^2 = \sum_{i=1}^{n} \left(\frac{x - (x_i + x_i' z)}{\sigma_{x,i}} \right)^2 + \left(\frac{y - (y_i + y_i' z)}{\sigma_{y,i}} \right)^2$$

where (x, y, z) are the vertex coordinates and x_i, x_i', y_i, and y_i' are the SSD track slopes and intercepts. The secondary vertex is found by combining candidate tracks from a given decay and by requiring the associated confidence level (obtained from the χ^2 above) to be greater than 1%.

Two methods are used by an algorithm called DVERT [24] to reconstruct the primary vertex. The first method that we describe is the one implemented in this analysis (and in all semileptonic analyses) and is coded in the DVFREE routine. After exclusion of candidate tracks from the charm particle decay vertex, this routine randomly selects a "seed" track reconstructed in the SSD system and it tries to combine the seed track with other tracks. A track is kept in the vertex if the confidence level of the vertex remains above 1%. When all the tracks have been tried, a new seed track is selected among the tracks that have not been used in a primary and the process is repeated. Each track but the seed track can be included in every primary found. Once the primary vertices are found, selection criteria are needed to pick the best candidate. Monte Carlo studies show that choosing the highest multiplicity vertex and, in the case of ambiguities, picking the most upstream vertex, maximizes the probability to find the right vertex.

Another approach, called "candidate driven", is used when each of the charm decay products is reconstructed. The momenta of the daughter particles are used to determine the momentum and direction of the charm particle (seed track). This highly efficient algorithm takes the charm particle seed and nucleates other tracks reconstructed in the SSD adding them one by one to the seed until the confidence level of the vertex falls below 1%.

4.4 Particle Identification

The FOCUS spectrometer is equipped with three Čerenkov detectors that can aid in distinguishing between the electron, pion, kaon, and proton hypotheses. The Čerenkov algorithm CITADL (Čerenkov Identification Algorithm using Digital Likelihood) returns the negative log-likelihood that the track had a Čerenkov pattern similar to that expected for the particle hypothesis. CITADL uses only the on/off status of Čerenkov cells rather than their pulse height in identifying particles. It determines for each track which cells within the three counters are contained in the $\beta = 1$ light cone. With this information, the algorithm evaluates the log-likelihoods assuming a Poisson probability $P_{i\alpha}$ that a track of mass α and parameters $\vec{t}$ will produce the observed outcome from the i-th cell. The routine returns its identification in terms of χ^2-like variables W_α called "Wobs":

$$W_\alpha = -2\sum_i \ln(P_{i\alpha}(\vec{t})), \tag{4.1}$$

where the sum is intended on all cells within the Čerenkov light cone $\beta = 1$. The Poisson probability $P_{i\alpha}$ is given by:

$$P_{i\alpha} = 1 - exp(-FE_{i\alpha}(\vec{t}))$$

and

$$P_{i\alpha} = exp(-FE_{i\alpha}(\vec{t}))$$

if the cell is on or off respectively and where $FE_{i\alpha}(\vec{t})$ represents the amount of light expected in cell i in the hypothesis that the track with parameters $\vec{t}$ has mass α. Cells that are inside more than one tracks' Čerenkov cone are excluded from the calculation. In the log-likelihood computation, the probability that a given track fires accidentally due to noise is taken into account [16].

Rather than using their absolute value, the hypotheses are compared to each other through a likelihood ratio. The event selection is accomplished by requiring a particle hypothesis α to be favored with respect to another hypothesis β by a n units of likelihood:

$$W_\beta - W_\alpha \ > \ n.$$

Another way to reject background is to require that the desired hypothesis be favored with respect to the best of the four hypotheses:

$$\min\left(W_{\beta=e,\ \pi,\ K,\ p}\right) - W_\alpha > \ n$$

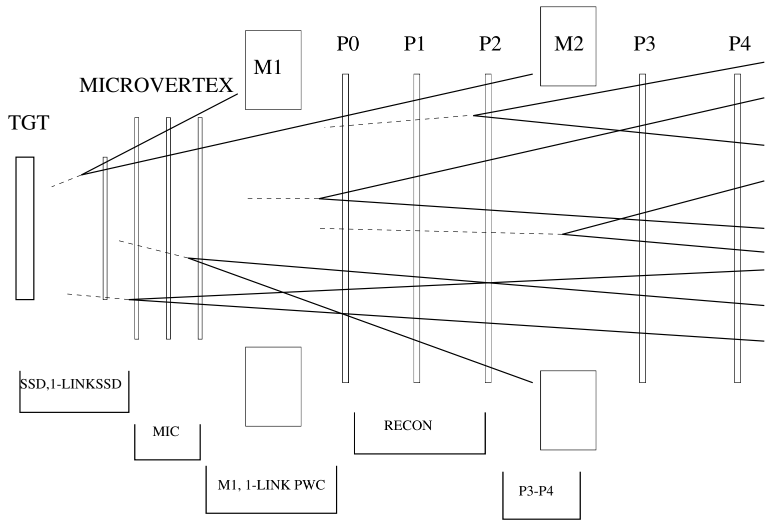

Figure 4.2: Different categories of vees reconstructed in FOCUS .

This algorithm guarantees high flexibility in the analysis process, allowing one to choose between efficiency and purity of the sample.

4.5 Vees Reconstruction

Neutral particles, Λ^0 and K_S^0, are called vees because their signature in the spectrometer is given by two charged tracks coming from a common vertex (the vee decay vertex). Since these particles are relatively long lived they often travel for a few meters in the spectrometer before decaying. The classification of these particles is based on the position of the decay vertex. Three main regions can be identified: the target region, the SSD region, and the region between the SSD and the first PWC chamber P0. Subcategories are based on the number of PWC chambers in which, each daughter of the vee, is reconstructed. In Fig. 4.2, all the vee categories are shown.

The common feature of the algorithm is to find a pair of tracks in the SSD or the PWC that originates from a common vertex [25]. Once this is accomplished, the momentum of each track is redetermined and the invariant mass is recomputed. The invariant mass is required to be consistent with the K_S^0 or the Λ^0 hypotheses and, in the case on the Λ^0, the proton mass is assigned to the higher momentum track. No Čerenkov identification is applied at this stage. In Fig. 4.3, the invariant mass distribution for the different categories is shown.

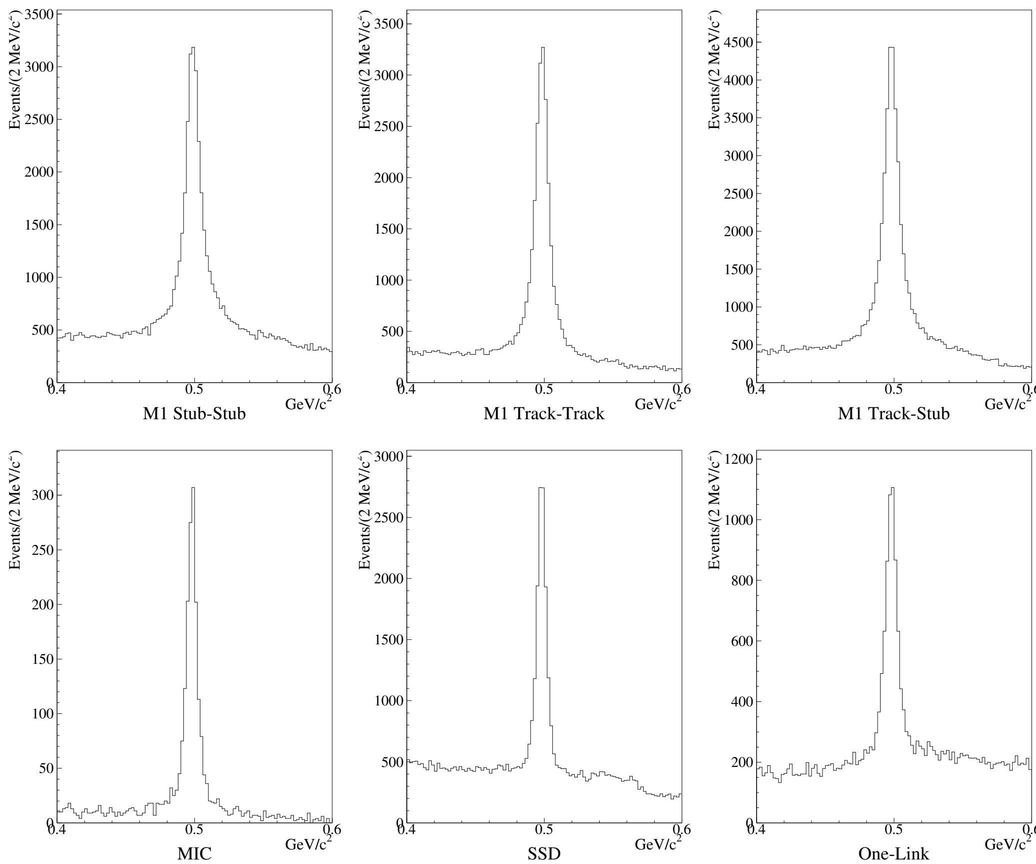

Figure 4.3: Invariant mass distributions for six categories of K^0_S's. The distributions come from a small sample of runs and include non charm events. The dominant categories in charm decays are the (*M1 track-track*) and (*M1 track-stub*) Vees.

4.6 Kink Reconstruction

The term "kink" indicates particles decaying into a charged and a neutral track. In FOCUS, kink reconstruction is performed for $\Sigma^{\pm}$ particle decays: $\Sigma^+ \rightarrow p\pi^0$, $\Sigma^+ \rightarrow n\pi^+$ and $\Sigma^- \rightarrow n\pi^-$. Like the vees, kinks are long lived and usually decay after the SSD. The algorithm considers all unlinked SSD tracks that point to the aperture

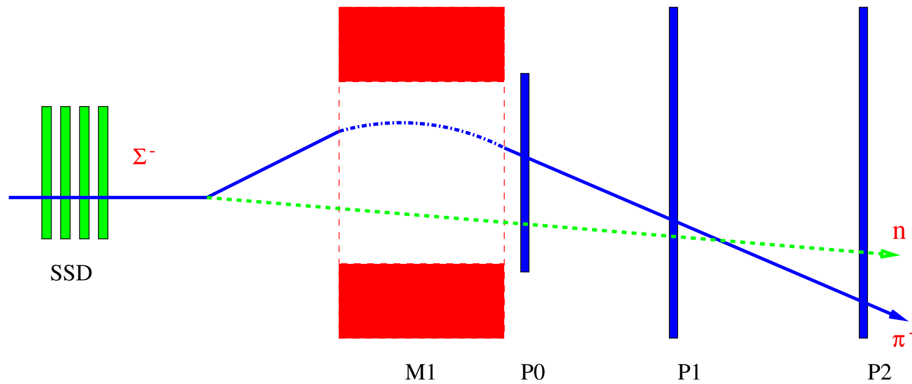

Figure 4.4: Topology of a "kink" in the FOCUS spectrometer.

of M1. These $\Sigma^{\pm}$ tracks are matched to unlinked PWC tracks. PWC tracks that have been used in a successful vee reconstruction are not considered. First, an initial z vertex location is determined by intersecting the SSD and PWC segments in the xz-plane. The z location is required to be downstream of the last SSD station and upstream of the first PWC chamber (Fig. 4.4). If the z vertex is located before the first analysis magnet, the candidate kink particle does not undergo a deflection and the parent momentum can be computed by assuming the parent mass and imposing kinematic constraints on the decay. This technique results in a two-fold ambiguity on the Σ candidate momentum. If the kink decays within M1 this ambiguity can be broken and a unique solution can be found. Tracing through M1 is possible only for 5-chambers PWC tracks for which information on the momentum is determined by the second analysis magnet M2.

To reduce background, Čerenkov requirements are made on the charged daughter: in the decay $\Sigma^+ \to p\pi^0$ the proton hypothesis is required to be favored with respect to the pion hypothesis by at least 4 units of likelihood, i.e. $W(\pi) - W(p) > 4$. In the case of $\Sigma^+ \to n\pi^+$ or $\Sigma^- \to n\pi^-$, the pion is required to be inconsistent with any other hypothesis and the neutron is required to deposit sufficient energy in the region where it is expected to strike the calorimeter.

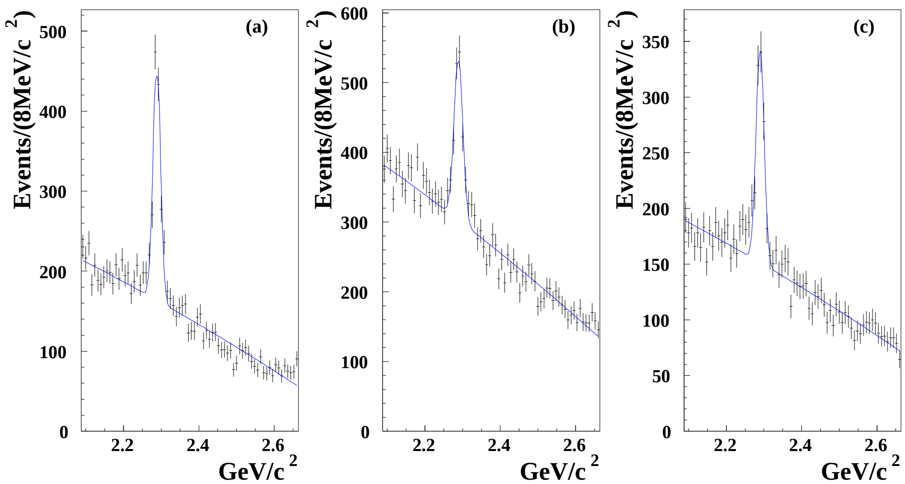

Figure 4.5: Three invariant mass plots for the decays (a) $\Lambda_c^+ \to \Sigma^+\pi^+\pi^-$ where $\Sigma^+ \to p\pi^0$ with a yield of 915±50 events, (b) $\Lambda_c^+ \to \Sigma^+\pi^+\pi^-$ where $\Sigma^+ \to n\pi^+$ with a yield of 854±65 events, and for (c) $\Lambda_c^+ \to \Sigma^-\pi^+\pi^-$ where $\Sigma^- \to n\pi^-$ with a yield of 654±42 events.

The neutron candidate must satisfy $0.3 < E/P < 2.0$ where P is the momentum of the neutron computed using the kinematic constraints [25]. The invariant mass distribution for the decay $\Lambda_c^+ \to \Sigma^+\pi^+\pi^-$ and $\Lambda_c^+ \to \Sigma^-\pi^+\pi^+$ are shown in Fig. 4.5

4.7 Hyperon Reconstruction

In FOCUS we reconstruct the hyperons Ξ^- and Ω^- in the final states $\Lambda^0\pi^-$ and $\Lambda^0 K^-$, respectively. These decays occur with a branching ratio of essentially 100% in the Ξ^- and about 68% for the Ω^-. The two main topology for these decays are defined by the position of the decay vertex. Hyperons that decay upstream of the SSD system are called “type-1”, while if the decay vertex is within or downstream of the SSD system, we refer to these particles as “type-2” (Fig. 4.6). A different reconstruction algorithm is applied according to the hyperon type. The hyperons are fully reconstructed. The main requirement for the neutral daughter is that it has to have a mass consistent with the Λ^0 mass. Further, the vee daughter must satisfy Čerenkov requirements, in particular, the proton hypothesis on the highest momentum track has to be favored over the pion

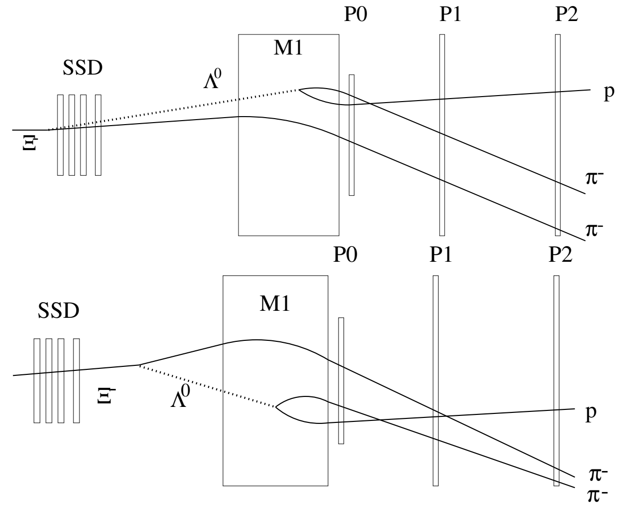

Figure 4.6: A schematic of a Ξ^- decay which occurs upstream (top) and downstream (bottom) of the silicon strip detector (SSD).

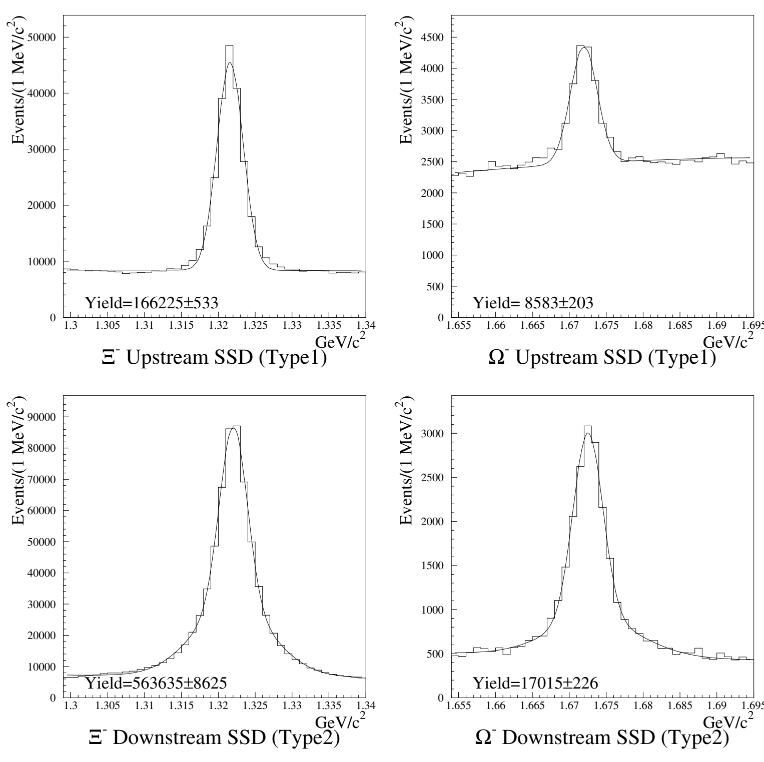

Figure 4.7: The invariant mass plots for the $\Lambda\pi^-$ and the ΛK^- combinations for the category where the decays occurs upstream (top row) and downstream (bottom row) of the SSD detector. The plots are for the full FOCUS data sample.

hypothesis by four units of likelihood [25]. In Fig. 4.7 the invariant mass distribution for type-1 and type-2 hyperons, is shown.

4.8 Electromagnetic Shower Reconstruction

The Čerenkov detector is useful in separating electrons and pions in certain ranges of momentum. Above the hadronic Čerenkov thresholds, the electron identification is provided by the calorimeters [26]. Since the electron rest mass is negligible and since the electromagnetic calorimeters are designed to collect nearly all the electromagnetic energy, electrons are identified by requiring that the ratio E/P be close to one. In the IE, electrons are required to have an E/P ratio between 0.8 and 1.2. If a track satisfies this cut, the algorithm assigns a variable IEID of 10. This variable is successively incremented by a value between 0 and 3 based on Čerenkov information. The OE uses a similar algorithm and assigns a discrete value to a variable named OESCORE, based on the E/P ratio and the Čerenkov information.

4.9 Hadronic Shower Reconstruction

Shower reconstruction in the hadronic calorimeter associates neutral clusters in the IE with energy clusters in the HC. In fact about 80% of the hadrons in the inner portion of the spectrometer undergo a nuclear reaction in the IE and begin showering. The IE has a resolution on the impact point of less than 1 cm. The energy resolution in the HC is given by [28]:

$$\frac{\sigma_E}{E} = 0.86\% + \frac{85\%}{\sqrt{E\ (\mathrm{GeV})}}$$

where the energy E assigned to the hadron is the sum of the energy deposited in the HC and the energy deposited in the IE. Reconstruction of neutral hadrons is used in the kink reconstruction algorithm.

4.10 Muon Identification

The muon reconstruction algorithm has the objective to limit as much as possible the misidentification (mainly from pions) while keeping a high efficiency. Three main mechanisms can contribute to muon misidentification: the detection of muons from the beam that are located close to a charged track reconstructed in the PWC; the "punch through" of hadrons that survive the thick layers of steel without producing a shower; the "in-flight" decays of pions or kaons into muons.

Muon candidates are reconstructed by extrapolating PWC tracks into the muon detectors and by looking for clusters of hits [27]. The search radius for clusters of hits depends on the track momentum. In the inner muon detector the track must be associated with hits in at least 4 out of 6 planes. To give flexibility for choosing an appropriate compromise between efficiency and background rejection, a given track is fit to the hits and a confidence level CL_μ is computed. This is achieved by constructing a χ^2 test to the hypothesis that the projected track passes through the hits within the anticipated error. Correlations between the hits due to multiple Coulomb scattering are accounted for and the χ^2 assumes the form:

$$\chi^2 = \sum_i \sum_j \, (t_i - X_i) \, C_{ij}^{-1} \, (t_j - X_j)$$

where the sum ranges over the muon detector planes, t_i is the coordinate of the track when extrapolated to the i-th plane and X_i is the actual hit in the i-th plane. The matrix C_{ij} is the coordinate covariant matrix which includes both measurement error and MCS effects and is given by $C_{ij} =< \delta X_i \, \delta X_j >$. The minimum requirement for a muon candidate is $CL_\mu > 0.01\%$.

The muon misidentification rate as a function of the track momentum is shown in Fig. 4.8 and compares data two two Monte Carlo simulations with different amount of noise. The principal noise in the muon detector comes from muons from decays of

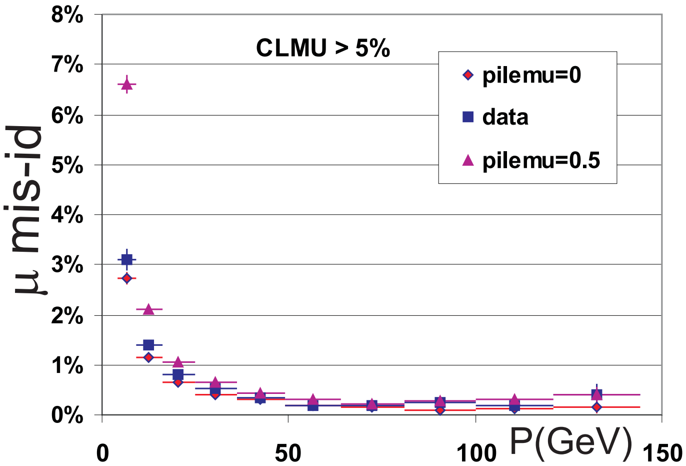

Figure 4.8: Misidentification of five chambers track kaons as muons in the inner muon detector [20]. A cut on the muon confidence level at 0.01% is required. The data (blue) comes from background subtracted high statistics charm decays and is compared two two Monte Carlo samples. The first Monte Carlo simulation has no noise from muon halo (pilemu=0.) simulated. The second simulation (pilemu=0.5) has a muon halo rate which is higher than is present in typical charm data.

pions contaminating the electron beam upstream of the converter. This background is commonly called muon halo. In Fig. 4.9 the MH plane efficiencies is presented. This efficiency is computed as the probability that a plane had a hit given that the other five planes had a hit.

The outer muon identification is complicated due to the presence of the internal magnetic field of M2. The algorithm in this case accounts for the bending due to the magnetic field for smearing due to multiple Coulomb scattering. In the case of outer muon tracks, one has to find hits in at least 2 of the 3 planes. Outer muons have not been used in this analysis.

4.11 Data Processing

FOCUS collected nearly 6.5 billion events during the data taking. The data were stored on about 6000 8 mm tapes amounting to more than 25 terabytes. The DAQ saved raw detector information from each PWC wire, Čerenkov cell, etc. for each event.

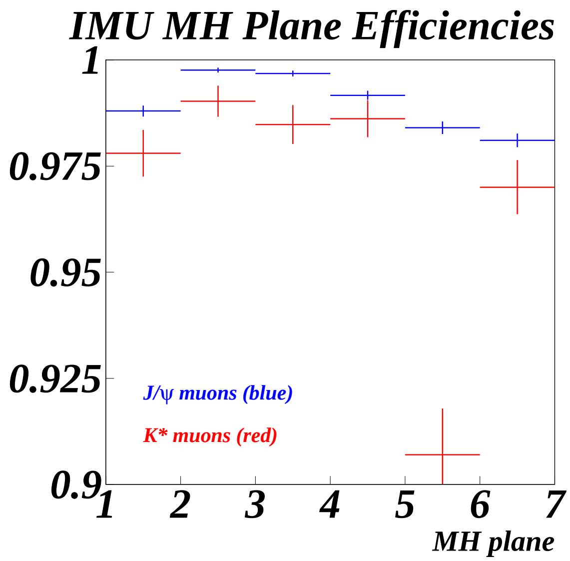

Figure 4.9: MH plane efficiencies computed using $J/\psi \rightarrow \mu^+\mu^-$ and $D^+ \rightarrow K^*(892)^0\mu^+\nu$ decays.

Table 4.1: Each superstream is based on physics topic.

Super Stream	Physics Topics	Skim2 Institution
1	Semi-leptonic	Puerto Rico
2	Topological vertexing and K_s^0	Illinois
3	Calibration and rare decays	CBPF, Brazil
4	Baryons	Fermilab
5	Diffractive (light quark states)	California, Davis
6	Hadronic meson decays	California, Davis

From this large set of data, events were reconstructed into tracks and vertex objects with momentum, energy, and particle identification information.

The first step of data processing is called Pass-1. Only pathological events were eliminated at this stage to allow the reconstructed data to be of the same size of the raw data, resulting in about 6000 new tapes. In the next step, called Skim-1, the data was divided in 6 smaller data sets ("superstreams") corresponding to different physics topics and totals about 2500 tapes. Pass-1 data processes has been done in Fermilab while Skim-1 was performed half at CU and half at Vanderbilt university. In Table 4.1 the six super-streams are listed.

The final step, Skim-2, produced 40 additional “streams” for a total of 2500 additional tapes. From these smaller skims each user was able to perform analysis with a reasonable data size. A schematic view of the data reconstruction process from DAQ to the final skims used for the data analysis is shown in Fig. 4.10

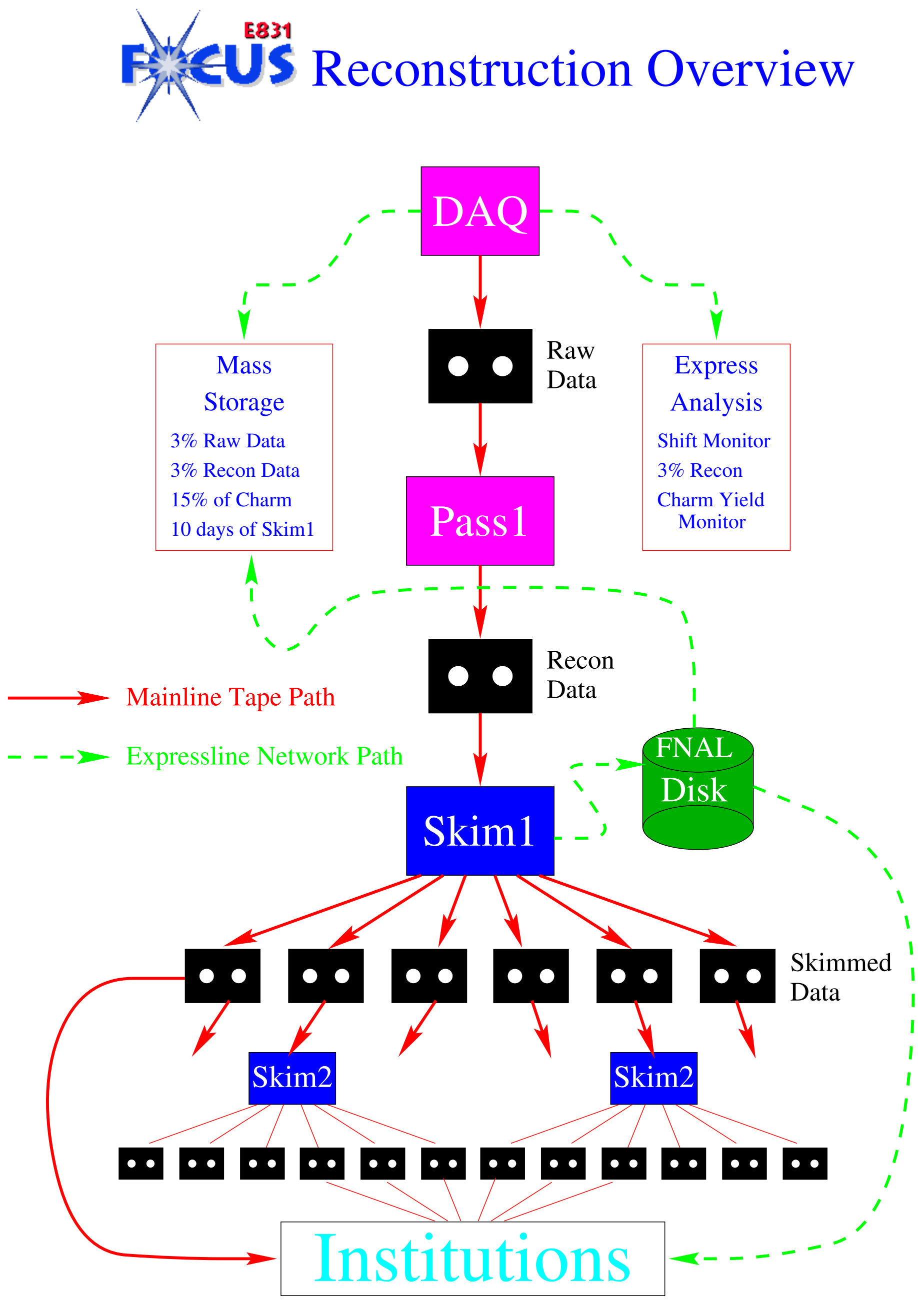

Figure 4.10: Data processing in FOCUS

Chapter 5

$D^0 \to \pi^-\mu^+\nu$ and $D^0 \to K^-\mu^+\nu$ event selection

This analysis is based on the Slepnorm skim created from Global Vertex skim-stream[1] . The purpose of this skim is to minimize any possible bias between a semileptonic decay and the relative normalization modes. In this analysis we are interested in the two semileptonic decays $D^0 \to \pi^-\mu^+\nu$ and $D^0 \to K^-\mu^+\nu$. The Slepnorm skim requires that the muon and another track form a vertex with a confidence level greater than 0.1%. The muon has to be identified by the inner or outer muon detectors with a confidence level greater than 0.1%. The Slepnorm skim consists of 1157 files for a total size of about 247 GBytes.

A sub-skim is applied to the Slepnorm skim to reduce the data to a manageable size and from this sub-skim output, HBOOK ntuples are generated. The final data set has somewhat general requirements which reject most of the background events without compromising the efficiency of the decays of interest. The most important requirements are: to have good primary and secondary vertices, a significance of separation L/σ_L (where L is the distance between primary and secondary vertex and σ_L is the error on this distance) greater than 4, a muon in the inner muon detector and a hadron-lepton invariant mass greater than 0.6 GeV/c^2. In the $\pi^-\mu^+\nu$ sample, the pion is required to be inconsistent with the kaon hypothesis. To improve our signal-to-noise we require the D^0 to come from a D^{*+} decay to $D^0\pi^+$ by reconstructing the corresponding soft-pion

[1] The Global Vertex algorithm requires the separation between the two most separated vertices to be greater than 4.5σ, where σ is the error on the distance between the two vertices.

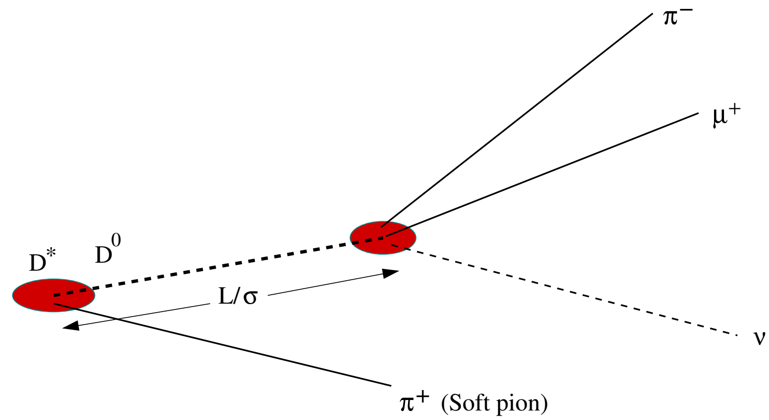

Figure 5.1: Topology of the D^0 semileptonic decays reconstructed in this analysis.

from the primary vertex.

5.1 The Final Data Set Reconstruction

To perform the measurements, we find a series of cuts that give a good signal-to-noise ratio while maintaining reasonable statistics. It is important to reduce the background level in the $\pi\mu\nu$ sample. This mode has a lower branching fraction and therefore will dominate the total uncertainty on the branching ratio measurements. Further, this mode has a significant background from Cabibbo allowed decays (mostly $K^-\mu^+\nu$ and $K^*(892)^-\mu^+\nu$) and from other Cabibbo suppressed decays like $\rho^-\mu^+\nu$. To minimize possible systematic uncertainties we use, when possible, the same cuts in both the decay modes $D^0 \to \pi^-\mu^+\nu$ and $D^0 \to K^-\mu^+\nu$. The statistics in the $D^0 \to K^-\mu^+\nu$ decay are much larger and we can afford to optimize the cuts on the $D^0 \to \pi^-\mu^+\nu$ sample without compromising the precision of the measurement.

The reconstruction starts by requiring two oppositely charged linked tracks corresponding to the candidate hadron and muon. These tracks must form a vertex with a secondary confidence level (CLS) greater than 1%. This vertex must also be isolated from other tracks in the SSD system. This is achieved by requiring that the confidence

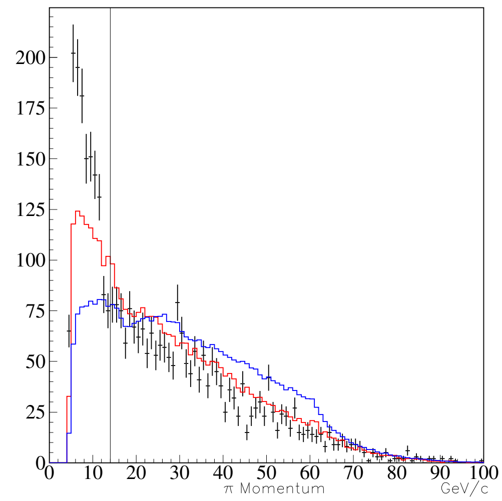

Figure 5.2: The plot shows the cut on the pion momentum. The data (points with error bars) is overlaid with a dedicated Monte Carlo of $\pi^-\mu^+\nu$ (blue histogram) and with a $c\bar{c}$ Monte Carlo (red histogram). The distributions are normalized by area. We reject events below the the black line.

level (ISO2) of another track to form a good vertex with the hadron-muon candidates to be less than 1%. Like the decay vertex, the production vertex must also satisfy a confidence level (CLP) greater than 1%. The most powerful cut in rejecting non charm background is given by the L/σ_L cut. We require L/σ_L to be greater than 6. In Fig. 5.1 we show the semileptonic event topology for this analysis.

The muon candidate must be identified by the inner muon system with a confidence level (CL_μ) on the muon hypothesis greater than 1%. To suppress pion and kaon in-flight decays, the associated track is required to have a consistent momentum when measured separately in the first and second analysis magnets, i.e. TRKFIT>1%. Further, the muon must be a 5-chamber track with a momentum greater than 10 GeV/c and have at most 2 missing planes in the inner muon system. Finally, events in which two muon candidates have a good confidence level and share more than four hits are rejected.

The hadron candidate must satisfy Čerenkov requirements: in the $\pi^-\mu^+\nu$ mode, the pion must be favored with respect to the kaon hypothesis by at least 3 units of likelihoods ($W(K) - W(\pi) > 3$); in the case of $K^-\mu^+\nu$ the kaon also has to be favored over the pion hypothesis by 3 units of likelihoods ($W(\pi) - W(K) > 3$).

Comparing a $c\bar{c}$ Monte Carlo to the data we found evidence for additional non-charm background in the $\pi^-\mu^+\nu$ sample (Fig.5.2) in the region of low momentum pions (where we are referring to the pion from the D^0 decay). We highly reduce this background by requiring the pion to have a momentum greater than 14 GeV/c.

Both the hadron and the muon are required to be singly linked to the PWC detector and to be inconsistent with tracks at zero degrees relative to the beam direction. This suppresses background from electron/positron pairs that have essentially zero transverse momentum.

The primary vertex is found using the tracks reconstructed in the SSD system where we exclude the candidate tracks from the D^0 decay vertex. The remaining tracks are used to form candidate primary vertices. Of these vertices we choose the one with the highest multiplicity and we break ambiguities by picking the most upstream vertex as the primary vertex.

For each hadron-lepton combination that satisfies the above requirements, another track coming from the primary vertex has to be found. This track is the candidate soft-pion from the D^{*+} and has to have a pion hypothesis which is favored over all the particle hypotheses (e, π, K, p) from the Čerenkov system ($W_{min} - W(\pi) > -6$). It must also have a momentum greater than 2.5 GeV/c .[2]

Finally, we remove contamination from $D^0 \to K^-\pi^+$ by applying a hadron-lepton invariant mass cut of less than 1.7 GeV/c^2. Contamination from D^0 decays where we lose a π^0 like $K^*(892)^-\mu^+\nu$, $\rho^-\mu^+\nu$, $K^-\pi^+\pi^0$ and $K^-\pi^+2\pi^0$ are suppressed by requiring the visible mass to be greater than 1.0 GeV/c^2. The list of the cuts that are applied is shown in Table 5.1. With this set of cuts we obtain the two samples shown in Fig. 5.3 a)

[2] The soft pion momentum distribution peaks at about 6 GeV/c.

DECAY	$\pi\mu\nu$	$K\mu\nu$	either
REME			$> 3\%$ on all tracks
NO DOUBLE LINK TRACKS			
CLS			$> 1\%$
ISO2			$< 1\%$
CLP			$> 1\%$
L/σ			> 6
MASS($h\mu$)			< 1.7 GeV/c^2
MASS($h\mu$)			> 1.0 GeV/c^2
$W(\pi)$-$W(K)$		> 3	
$W(K)$-$W(\pi)$	> 3		
min(W_{all})-$W(\pi)$	> -6		
π^- momentum	> 14 GEV/c		
CL$_\mu$			$> 1\%$
Muon Momentum			≥ 10 GeV/c
TRKFIT			$> 1\%$
min(W_{all})-W(π_{soft})			> -6
Soft pion in primary			YES
π_{soft} momentum			> 2.5 GEV/c

Table 5.1: List of the most important selection cuts.

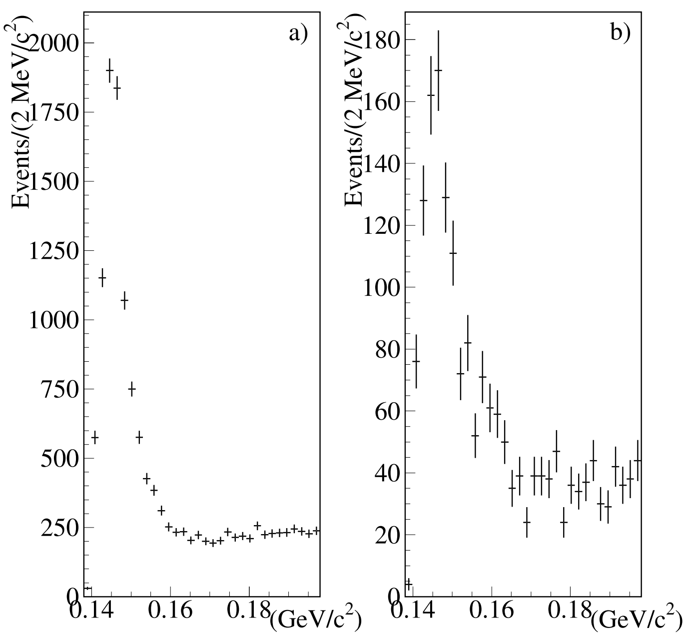

Figure 5.3: $D^{*+} - D^0$ mass difference distributions after the selection criteria. a) $D^0 \rightarrow K^-\mu^+\nu$ b) $D^0 \rightarrow \pi^-\mu^+\nu$

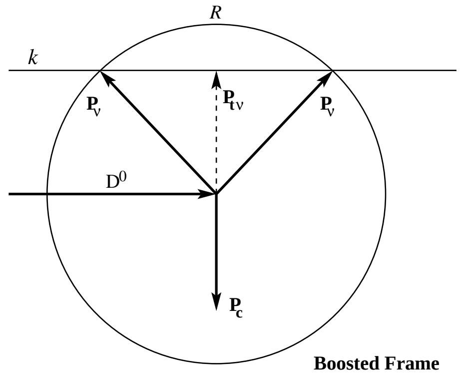

Figure 5.4: Neutrino closure obtained by imposing momentum and energy conservation. From momentum conservation the allowed neutrino momentum lies on the straight line k. From energy conservation the allowed neutrino momenta must lie on the circle $\mathcal{R}$. The intersections determine the two solutions.

and 5.3 b) for $K^-\mu^+\nu$ and $\pi^-\mu^+\nu$, respectively.

Another important issue when dealing with semileptonic decays (especially at fixed target experiments) is to reconstruct the D^0 momentum from the available information. In the case of interest, since the neutrino is lost, kinematic constraints must be applied to extract the D^0 momentum. The lack of information results in ambiguities in the possible solutions. In the following sections we will describe the two approaches that have been used to address this issue.

5.2 The Neutrino Closure

The width of the $D^{*+} - D^0$ mass difference that we obtain by simply subtracting the $h^-\mu^+$ invariant mass from the $h^-\mu^+\pi_s^+$ invariant mass (where h is either a pion or a kaon) can be greatly improved by finding the neutrino momentum. Due to the lack of information (the neutrino is not detected), this can be achieved by imposing kinematic constraints that allow us to determine this momentum up to a two-fold ambiguity.

The easiest way to proceed is to boost the system into a reference frame where the hadron-muon system has a momentum $\vec{P}_c$ orthogonal to the D^0 direction. In this frame the transverse momentum of the neutrino is equal (in magnitude) to the charged system momentum while the longitudinal component is unknown. By imposing the D^0 nominal mass and energy conservation on the decay, the magnitude of the neutrino momentum is determined. This can be pictured by saying that the neutrino momentum has to lie on a circle of fixed radius which intersects the line of possible longitudinal momenta in two points. These two points are shown in Fig. 5.4 and represent the two solutions for the neutrino (and therefore the D^0) momentum. In this analysis we use the solution that gives the lowest mass difference. A complete derivation of the D^0 momenta is shown in Appendix A.

5.3 The D^* Cone Closure

An important part of this analysis is the measurement of the pole masses and of the ratio of form factors $f_-^K(0)/f_+^K(0)$. Most of this information is contained in the q^2 dependence of the decay. Rather than using the neutrino closure described in the previous section we can take advantage of the D^{*+}-tag in the following way: we boost the system into the hadron-lepton center of mass. In this frame the neutrino and the D^0 are directed parallel to each other. By constraining the $K^-\mu^+\nu$ ($\pi^-\mu^+\nu$) mass to the D^0 mass and the $K^-\mu^+\nu\ \pi_s^+$ ($\pi^-\mu^+\nu\ \pi_s^+$) mass to the D^{*+} mass, the D^0 direction describes a cone around the soft-pion direction with fixed relative angle α (Fig. 5.5).

Each point on the cone corresponds to a value of the q^2 within the allowed kinematic range. By sampling the azimuthal angle ϕ we can choose the D^0 direction that is most consistent with pointing to the primary vertex. The choice is based on a χ^2 variable that tests this consistency. The smallest χ^2 gives the best solution for the D^0 (and therefore the neutrino) momentum. With this prescription we can find the best solution among the infinite solutions corresponding to the points on the circle. A complete description of the procedure is described in Appendix B. This technique to discriminate the best solution without implementation of a χ^2 variable is described in Ref. [29]. The χ^2 test was implemented by the University of Illinois group.

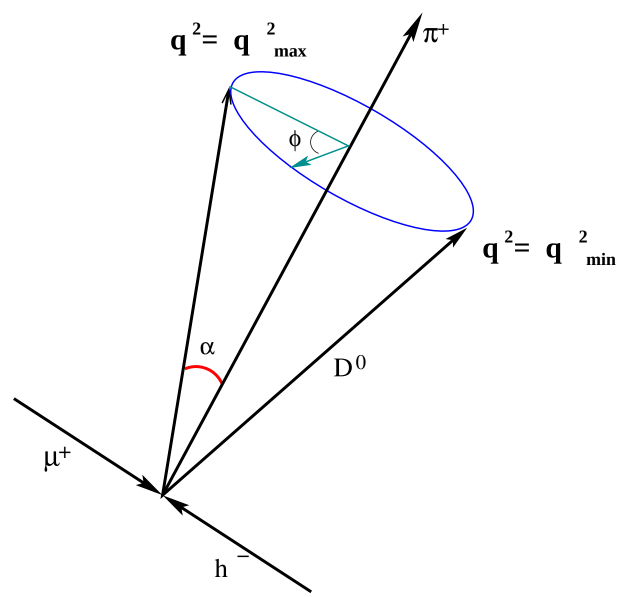

Figure 5.5: The cone closure is obtained by imposing the D^0 mass and the D^* mass in the hadron-lepton rest frame and by choosing the angle ϕ corresponding to the D^0 direction that is most consistent with pointing to the primary.

Chapter 6

Fit to $\pi^-\mu^+\nu$ and $K^-\mu^+\nu$

In this chapter we describe the procedure that we follow to extract signal yields from the data distribution. This is accomplished by using a fitting technique based on the minimization of a negative binned log-likelihood that uses Monte Carlo simulation of the backgrounds and signals to determine the expected number of events in each bin. We give a description of the generation process of the Monte Carlo contributions that we use in the fit. Further, we describe how the same fitting technique allows us to extract information about the q^2 dependence of the decay modes of interest. The chapter ends with a report on the measurement of the form factor ratio f_+^π/f_+^K at $q^2 = 0$.

6.1 General Description of the Fit

The fitting technique is designed to accomplish two goals: the first is to give information about the background shapes to minimize the correlation of these shapes to the signal. The second goal is to include as much information as possible about the parameters that we want to measure. With these goals in mind we decided to fit to a two dimensional distribution of q^2 and $\cos\theta_l$. The q^2 contains all the information about the pole mass or in general the q^2 dependence. The $\cos\theta_l$ distribution has all the complementary information about the decay dynamics. Another powerful variable is the $D^{*+} - D^0$ mass difference which is basically unaffected by the choice of the pole mass but is very useful in determining the level of "non-peaking" background. This background comes dominantly from real semileptonic decays associated with random pions which imitates a $D^{*+} \to D^0\pi^+$ decay. The advantage of using $\cos\theta_l$ and q^2 rather than the $D^{*+} - D^0$ mass difference is that we can place a cut in the signal region of the $D^{*+} - D^0$ mass difference and dramatically reduce the amount of background in our sample. This is particularly important because we don't have to heavily rely on the correct simulation of the shape of this background when fitting for the pole masses. Nevertheless, the mass difference is used to determine the amount of combinatoric background that is then fixed in the fit of the q^2 and $\cos\theta_l$ distributions. We use a binned likelihood fit where the likelihood is defined as:

$$\mathcal{L} = \prod_{ij} \frac{f_{ij}^{n_{ij}} e^{-f_{ij}}}{n_{ij}!} \tag{6.1}$$

where f_{ij} (n_{ij}) is the number of expected (observed) events in the bin ij.

6.2 Monte Carlo Simulation

The Monte Carlo simulation of photoproduction of charm particles is obtained by using the PYTHIA generator (version 6.127) which simulates the interaction between a photon with energy corresponding to the energy of the FOCUS beam and a nucleon (neutron or proton). The output is a list of particles with known momenta. The decays of these particles are then simulated using parameters (branching ratio, lifetimes, spins, etc.) defined in the FOCUS code. If the matrix element for a given decay is not known, a flat distribution in the phase space is generated. Further, the FOCUS Monte Carlo is responsible for tracing the particles through the spectrometer.

The reconstruction of simulated decays is performed as closely as possible to the data reconstruction. The tuning of PYTHIA and of the FOCUS Monte Carlo to match the data has been extensively studied by the FOCUS collaboration.

The signals and the main contributions from specific modes to the backgrounds

	$\pi^-\mu^+\nu$	$K^-\mu^+\nu$
$D^{*+} \to D^0\pi^+ \to (\pi^+)\pi^-\mu^+\nu$	YES	NO
$D^{*+} \to D^0\pi^+ \to (\pi^+)K^-\mu^+\nu$	YES	YES
$D^{*+} \to D^0\pi^+ \to (\pi^+)K^-\pi^0\mu^+\nu$	YES	YES
$D^{*+} \to D^0\pi^+ \to (\pi^+)K^0\pi^-\mu^+\nu$	YES	NO
$D^{*+} \to D^0\pi^+ \to (\pi^+)\rho^-\mu^+\nu$	YES	NO
$c\bar{c}$ without individual contributions	YES	YES

Table 6.1: The boxes labeled with "NO" imply that no dedicated contribution is present in the fit, the decay is included in the $c\bar{c}$ Monte Carlo sample.

are generated using a dedicated Monte Carlo meaning that one "leg" (charm or charmbar) will always produce the specified decay while the other leg (charmbar or charm) will be generated according to the hadronization process simulated by PYTHIA.[1] The simulated shapes used in the fit to the data are shown in Table 6.1. Let's now briefly discuss the specific decay modes simulated to fit the backgrounds.

$D^0 \to K^-\mu^+\nu$: this is the Cabibbo favored mode to which we are normalizing the $D^0 \to \pi^-\mu^+\nu$ decay. Since the branching ratio for this mode is much larger than that of the Cabibbo suppressed decay, and the misidentification rate is of the order of few percent, this mode represents a significant component of the background in the $\pi^-\mu^+\nu$ data set. The FOCUS Monte Carlo generates this mode assuming a pole dominance dependence of the form factor with a pole at the mass of the $D_s^*(2114)$.

$D^0 \to K^-\pi^0\mu^+\nu$: this represents the main background contribution to the signal region of the $D^{*+} - D^0$ mass difference for the decay $D^0 \to K^-\mu^+\nu$. It is generated in the same way as decay $D^+ \to K^-\pi^+\mu^+\nu$, which means that about 95% of the time the D^0 decays to $K^{*-}\mu^+\nu$ while 5% of the time it decays through an S-wave component [30]. Again, a pole mass dependence parametrization is assumed for the form factors: we use 2.114 GeV/c^2 for the **vector pole** and 2.5 GeV/c^2 for the **axial pole**.

$D^0 \to K^0\pi^-\mu^+\nu$: this is generated in an identical way to the previous mode $D^0 \to K^-\pi^0\mu^+\nu$. It represents a significant background component only for the $D^0 \to \pi^-\mu^+\nu$ de-

[1] This model predicts that about 15% of the time the "opposite charm" hadronizes into D^{*+} particle.

cay.

$D^0 \to \rho^-\mu^+\nu$: this mode has been generated to assess the amount of background feeding down into the $\pi^-\mu^+\nu$ sample. Since the only difference between $\pi^-\mu^+\nu$ and $\rho^-\mu^+\nu$ is a missing π^0, a mass cut is the only way to reject this background. With a lower limit mass cut of 1 GeV/c^2, we are able to reject most of this background, yet some still remains.

In our default Monte Carlo, no matrix element was simulated for this decay. To have a better estimate of the efficiency and of the shape for $\rho^-\mu^+\nu$, we implemented a matrix element which has the same form factors measured in $D^+ \to K^*(892)^0\mu^+\nu$ [31]. Since the decay $D^0 \to \rho^-\mu^+\nu$ is Cabibbo suppressed, the pole masses are different from the $K^*(892)^0\mu^+\nu$ pole masses: we set the vector pole to be 2.01 GeV/c^2 (like for $\pi^-\mu^+\nu$) and the axial pole to be 2.42 GeV/c^2. This change in the simulation turns out to have a minor effect on the $\rho^-\mu^+\nu$ background efficiency and no effect on the shapes that we fit for.

We generated 60 million events for each of these modes. This guarantees that, after the reconstruction, our Monte Carlo samples have sufficient yields to neglect their contribution to the statistical error. The remaining background is obtained by reconstructing as signal a $c\bar{c}$ Monte Carlo sample where all the specific contributions have been removed. The $c\bar{c}$ Monte Carlo sample consists of more than 20 times larger yield than the FOCUS data set. In Fig. 6.1-6.4 the shapes for the different modes are presented.

6.3 Technical Details

An important issue in this analysis is that the $\pi^-\mu^+\nu$ sample, even after our cut selection, will have background contributions that are of the same order of magnitude as the signal. Since the $K^-\mu^+\nu$ sample is much cleaner and has a much larger yield, we can use the fit to the $K^-\mu^+\nu$ sample to extract information about $\pi^-\mu^+\nu$ background.

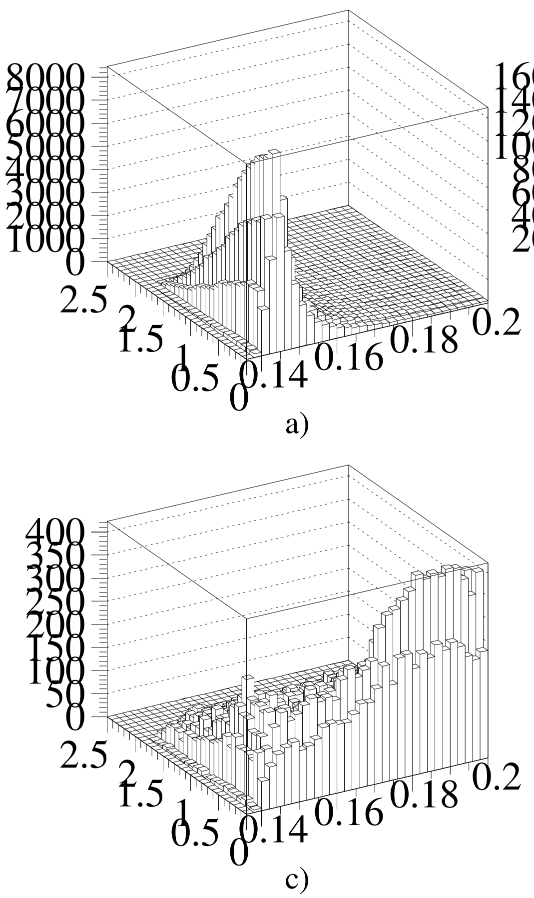

Figure 6.1: $D^* - D$ mass difference versus q^2. Monte Carlo distributions of the shapes used to fit $K^-\mu^+\nu$ sample. a) $K^-\mu^+\nu$, b) $K^-\pi^0\mu^+\nu$ and c) background from a $c\bar{c}$ Monte Carlo sample where the modes $K^-\mu^+\nu$ and $K^-\pi^0\mu^+\nu$ have been removed.

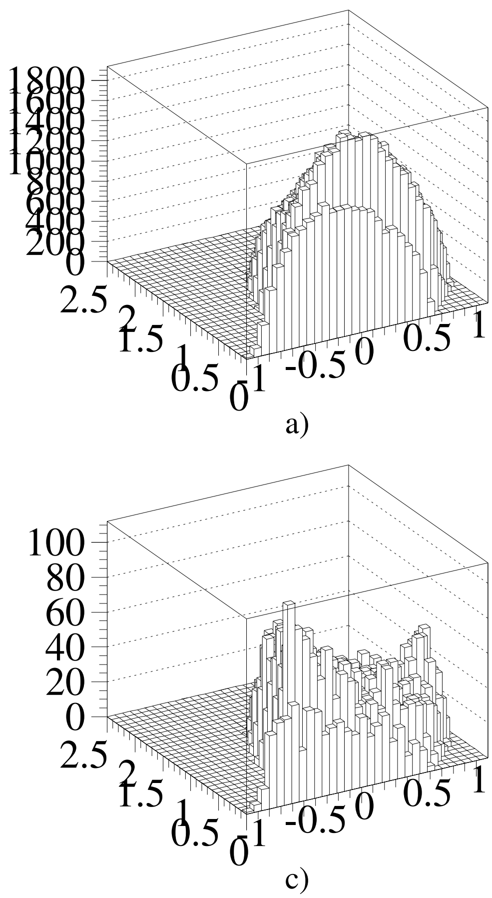

Figure 6.2: $cos\theta_l$ versus q^2. Monte Carlo distributions of the shapes used to fit $K^-\mu^+\nu$ sample. a) $K^-\mu^+\nu$, b) $K^-\pi^0\mu^+\nu$ and c) background from a $c\bar{c}$ Monte Carlo sample where the modes $K^-\mu^+\nu$ and $K^-\pi^0\mu^+\nu$ have been removed.

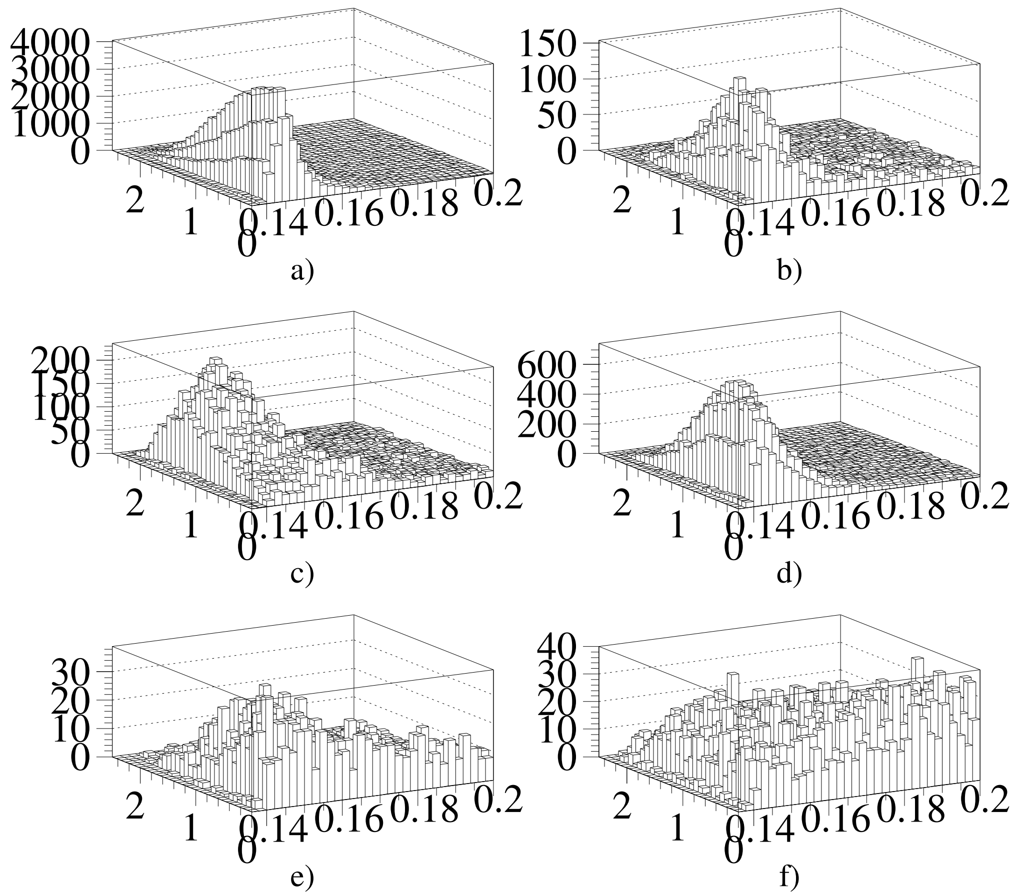

Figure 6.3: $D^* - D$ mass difference versus q^2. Monte Carlo distributions of the shapes used to fit $\pi^-\mu^+\nu$ sample. a) $\pi^-\mu^+\nu$, b) $K^-\mu^+\nu$, c) $K^0\pi^-\mu^+\nu$, d) $\rho^-\mu^+\nu$, e) $K^-\pi^0\mu^+\nu$ and f) background shape generated using a $c\bar{c}$ Monte Carlo sample where the modes a)-e) have been removed.

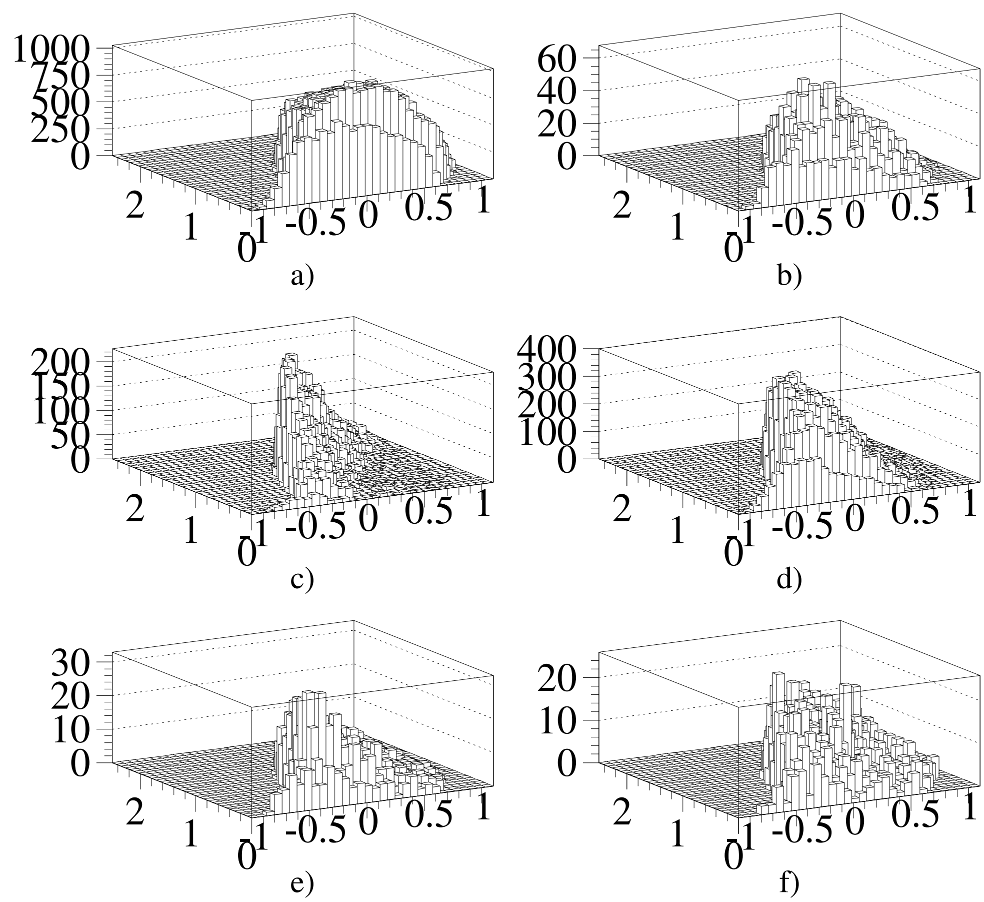

Figure 6.4: $cos\theta_l$ versus q^2. Monte Carlo distributions of the shapes used to fit $\pi^-\mu^+\nu$ sample. a) $\pi^-\mu^+\nu$, b) $K^-\mu^+\nu$, c) $K^0\pi^-\mu^+\nu$, d) $\rho^-\mu^+\nu$, e) $K^-\pi^0\mu^+\nu$ and f) background shape generated using a $c\bar{c}$ Monte Carlo sample where the modes a)-e) have been removed.

Namely, we extract information about two sources of background: the $K^-\mu^+\nu$ itself when the kaon is misidentified as a pion, and the contribution from $K^*(892)^-\mu^+\nu$. We use this information by constraining the relative amounts of these decays in the two samples $\pi^-\mu^+\nu$ and $K^-\mu^+\nu$, to the misidentification rate returned by the Monte Carlo. It should be noticed that the $K^*(892)^-\mu^+\nu$ background is present in the $K^-\mu^+\nu$ sample only when the $K^*(892)^-$ decays to the $K^-\pi^0$ final state, while it is present in the $\pi^-\mu^+\nu$ sample mostly when the $K^*(892)^-$ decays to the $K^0\pi^-$ final state. The appropriate correction for Clebsh-Gordan coefficient has to be made.

Rather than using Eq. 6.1 we prefer to minimize the **negative log-likelihoods**:

$$
\begin{aligned}
F_{\pi\mu\nu} &= -\,2\;\log(\mathcal{L}_{\pi\mu\nu}) \\
F_{K\mu\nu} &= -\,2\;\log(\mathcal{L}_{K\mu\nu})
\end{aligned}
\tag{6.2}
$$

which translates into a sum, over the all the (i, j) bins, of terms of the type:

$$
-2\log(\mathcal{L}^{ij}) = n^{ij}\;\log(f^{ij}) - f^{ij}. \tag{6.3}
$$

The array n_{ij} contains the observed number of events in the 2−dimensional data histogram, while f_{ij} is the number of expected events and is constructed by summing over the expected signal and backgrounds contributions in the following way:

$$
f^{ij}_{K^-\mu^+\nu} = \; Y_{K^-\mu^+\nu}\; S^{ij}_{K^-\mu^+\nu} + Y_{(c\bar{c})}\; S^{ij}_{(c\bar{c})} + Y_{K^-\pi^0\mu^+\nu}\; S^{ij}_{K^-\pi^0\mu^+\nu} \tag{6.4}
$$

for the fit to $K^-\mu^+\nu$, while:

$$
\begin{aligned}
f^{ij}_{\pi^-\mu^+\nu} \;=\;& Y_{\pi^-\mu^+\nu}\; S^{ij}_{\pi^-\mu^+\nu} + Y_{(c\bar{c})}\; S^{ij}_{(c\bar{c})} + Y_{\rho^-\mu^+\nu}\; S^{ij}_{\rho^-\mu^+\nu} + \\
& + Y^0_{K^-\mu^+\nu}\, \frac{\epsilon([K^- \to \pi^-]\mu^+\nu)}{\epsilon(K^-\mu^+\nu)}\; S^{ij}_{[K^-\to\pi^-]\mu^+\nu} + \\
& + Y^0_{K^-\pi^0\mu^+\nu}\, \frac{\epsilon([K^- \to \pi^-]\pi^0\mu^+\nu)}{\epsilon(K^-\pi^0\mu^+\nu)}\; S^{ij}_{[K^-\to\pi^-]\pi^0\mu^+\nu} + \\
& + 2\; Y^0_{K^-\pi^0\mu^+\nu}\, \frac{\epsilon(K^0\pi^-\mu^+\nu)}{\epsilon(K^-\pi^0\mu^+\nu)}\; S^{ij}_{K^0\pi^-\mu^+\nu}.
\end{aligned}
\tag{6.5}
$$

for the fit to $\pi^-\mu^+\nu$. In Eqs. 6.4 and 6.5 the fit parameters Y_α are the yields, S_α are the normalized shapes obtained from Monte Carlo and ϵ the reconstruction efficiency. Further, the quantities $Y^0_{K^-\mu^+\nu}$ and $Y^0_{K^-\pi^0\mu^+\nu}$ in Eq. 6.5 are fixed to the results obtained from the fit to the $K^-\mu^+\nu$ data (Eq. 6.4). In the Eq. 6.5 the symbol $[X \to Y]$ means that a hadron X is misidentified as Y. It should also be noticed that these expressions depend on the efficiencies of $D^0 \to \pi^-\mu^+\nu$ and $D^0 \to K^-\mu^+\nu$. These efficiencies are in general not flat in q^2 . This fact has serious consequences on the fit if the algorithm does not account for the fact that a lower pole mass (with respect to the generated value) results in a change of the overall efficiency of the decay. Therefore the efficiencies become a "dynamical variable" during the minimization process and they change for different choices of the pole masses or of the form factor ratios (this is better explained in the section that describes the weighting technique).

There is another way we can improve the fitting procedure. The branching ratios of a Vector to PseudoScalar (VPS) semileptonic decay have been recently measured by FOCUS [32] for D^+ decays. In the same way the branching ratio of the Cabibbo Suppressed $D^+ \to \rho^0\mu^+\nu$ relative to the Cabibbo Favored $D^+ \to K^*(892)^0\mu^+\nu$ (CSCF) is fairly well known. Assuming isospin symmetry, the VPS branching ratio does not change from D^+ to D^0 decays while a factor of 2 correction must be made to go from D^+ to D^0 in the CSCF branching ratio. We can put this information (with relative uncertainty) in the fit by adding two constraints in the form of χ^2 penalty terms. Eq. 6.2

becomes:

$$F_{\pi\mu\nu} = -2\ \log(L_{\pi\mu\nu}) + \chi_1^2$$
$$F_{K\mu\nu} = -2\ \log(L_{K\mu\nu}) + \chi_2^2 \tag{6.6}$$

where

$$\chi_1^2 = \frac{(3\ \frac{Y_{K^-\pi^0\mu^+\nu}}{Y_{K^-\mu^+\nu}} \frac{\epsilon(K^-\mu^+\nu)}{\epsilon(K^-\pi^0\mu^+\nu)} - VPS)^2}{(SVPS)^2} \tag{6.7}$$

and

$$\chi_2^2 = \frac{(\frac{Y_{\rho^-\mu^+\nu}}{Y_{K^-\pi^0\mu^+\nu}} \frac{\epsilon(K^-\pi^0\mu^+\nu)}{3\ \epsilon(\rho^-\mu^+\nu)} - CSCF)^2}{(SCSCF)^2}. \tag{6.8}$$

We use $VPS = 0.63$ and relative error $SVPS = 0.05$ for the vector to pseudoscalar branching ratio (VPS) while for the $\rho^-\mu^+\nu$ to $K^*(892)^-\mu^+\nu$ branching ratio we used $CSCF = 0.086$ and $SCSCF = 0.01$. In Fig. 6.5 the two projections of the two-dimensional fit are shown overlaid with the data histogram. In Fig. 6.6 we show the combinatoric and semileptonic components as well as the signal component.

6.4 The Weighting Procedure

In the previous section we described how the fit is set up to find the individual contributions from the known backgrounds entering the data sample. In this analysis we also want to measure the parameters entering the decay amplitude of $\pi^-\mu^+\nu$ and $K^-\mu^+\nu$. Therefore we have to be able to modify the shapes that enter Eqs. 6.4 and 6.5 for these two decays. This is achieved by re-weighting each Monte Carlo event according to the ratio of the probability that the event was generated with a pole mass[2] M'_{pole}, and a form factor ratio η' and the probability that the event was generated with the

[2] The measurement is model dependent and we are assuming the pole dominance model described in Chapter 1.

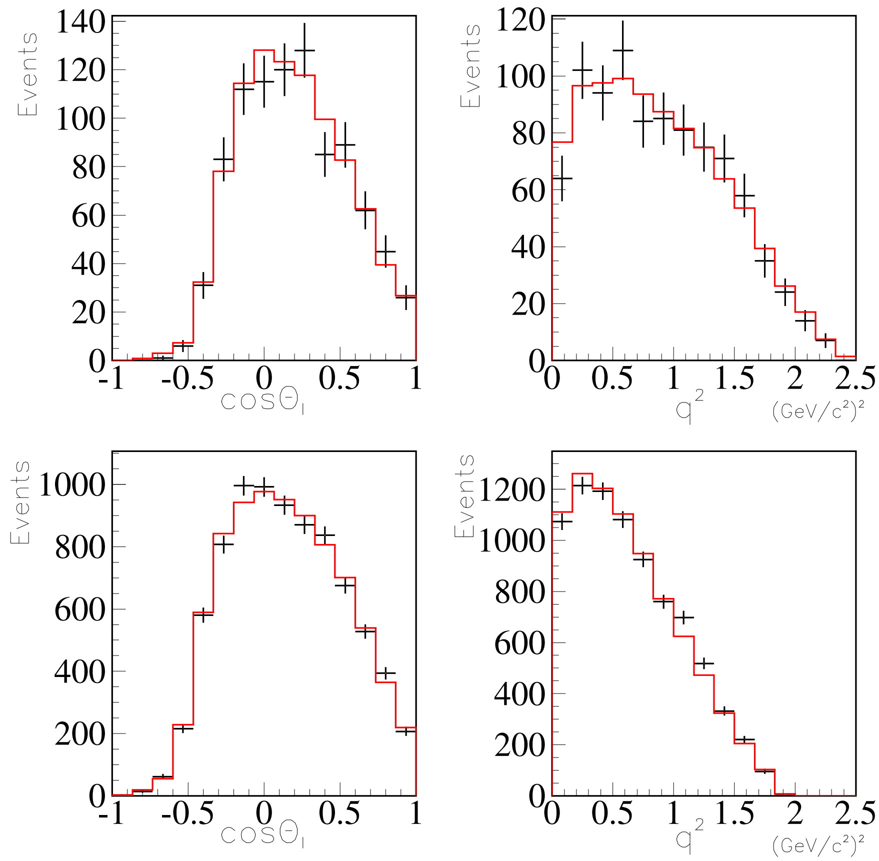

Figure 6.5: Two-dimensional fit projections for $K^-\mu^+\nu$ and $\pi^-\mu^+\nu$.

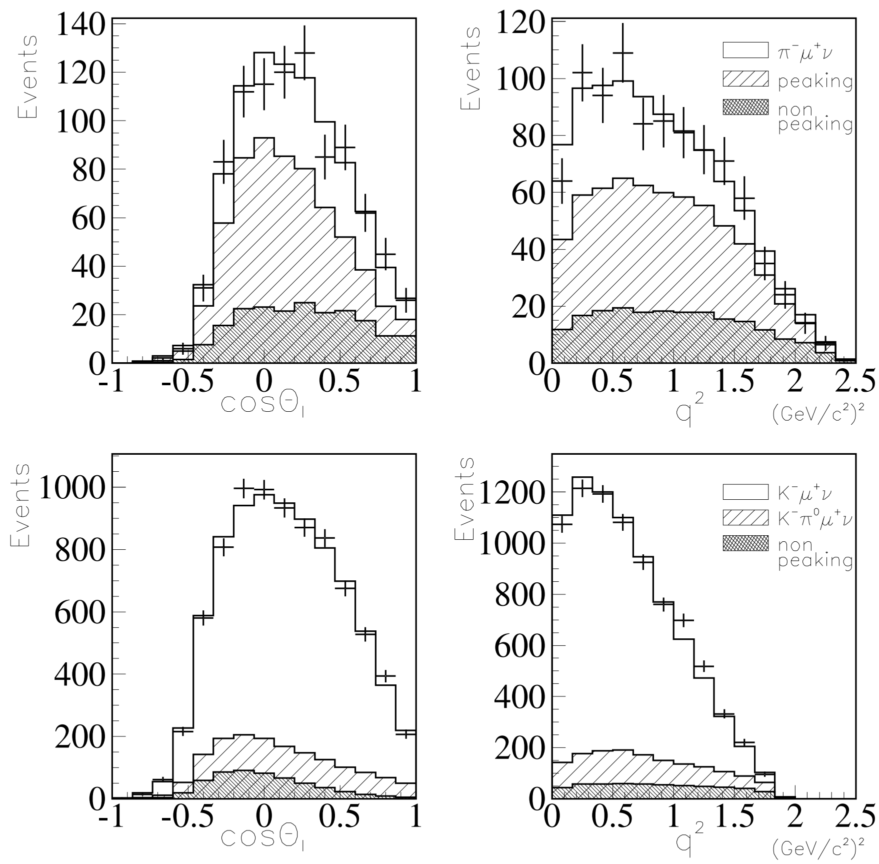

Figure 6.6: Components of the two-dimensional fit for $K^-\mu^+\nu$ and $\pi^-\mu^+\nu$. With the term “non-peaking” we mean the background contribution obtained by a $c\bar{c}$ Monte Carlo with no specific contributions. In the $\pi^-\mu^+\nu$ plot we refer to the packing contribution as the sum of $\rho^-\mu^+\nu$, $K^*(892)^-\mu^+\nu$, and $K^-\mu^+\nu$ backgrounds.

default values M^0_{pole} and η^0. The variables M'_{pole} and η' are the fit parameters and the closer they are to the default values the closer the weight is to 1. The weight, W, is given by the following equation:

$$W_i = \frac{I(M'_{pole}, \eta'; q_i^2)}{I(M^0_{pole}, \eta^0; q_i^2)} \frac{N(I(M^0_{pole}, \eta^0)}{N(I(M'_{pole}, \eta')} \tag{6.9}$$

where the intensity is factorizable into two functions, one dependent only on the pole mass (the form factor) and one dependent on η:

$$I(M_{pole}, \eta; q^2) \propto f_+^2(M_{pole}; q^2)\ g(\eta) \tag{6.10}$$

and the normalization is:

$$N(M_{pole}, \eta) = \sum_{i=1}^{Ngen} f_+^2(M_{pole}; q_i^2)\ g(\eta). \tag{6.11}$$

Two things should be noticed: in the computation of the intensity I, for each event with a given reconstructed q^2, we use the corresponding generated q^2 value. Second, the normalization must be computed by summing over all the generated events (before any kind of reconstruction or trigger requirements). We need the correct probability to generate an event at a given q^2 for a given set of parameters (M_{pole}, η) without including smearing or efficiency effects.

The normalization $N(M_{pole}, \eta)$ plays an important role and must be included in the weighting scheme. We care not only about the change in the shape, to which the normalization does not contribute, but also about the change in the efficiency, which is defined as the ratio of the reconstructed and generated events. Naively, the normalization keeps track of the fact that the number of generated events changes as a function of the pole mass or of the form factor ratio and accounts for this difference in the computation of the overall efficiency of the decay. A flow diagram of the weighting technique is shown in Fig. 6.7. The results from the fit shown in Fig. 6.5 are reported

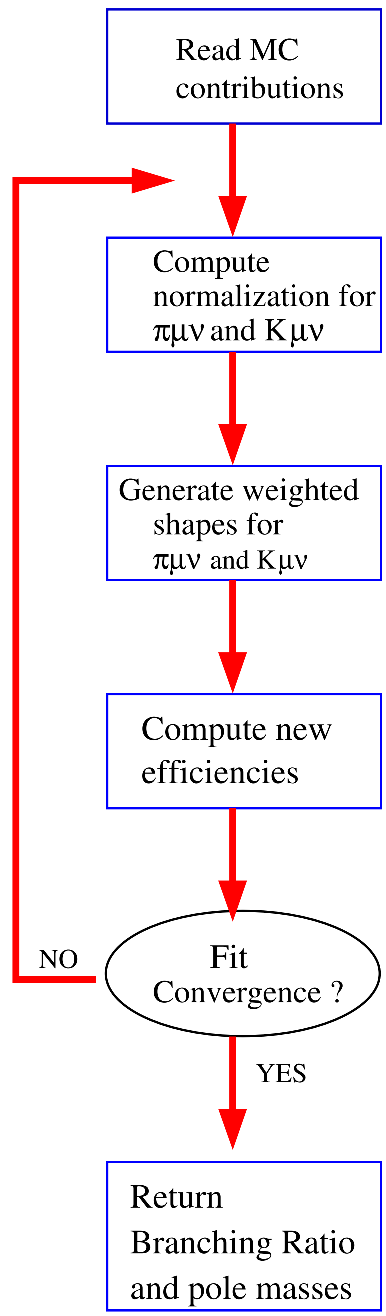

Figure 6.7: Flow diagram describing the steps of the weighting procedure.

in Table 6.2:

parameter	Yield	ϵ	BR	Pole Mass
$K^-\mu^+\nu$	6574 ± 92	0.0058	1.	$1.93^{+0.05}_{-0.04}$
$K^-\pi^0\mu^+\nu$	546 ± 40	0.0024	$\frac{1}{3} \times (0.61 \pm 0.05)$	
$c\bar{c}$ background	1001 ± 43			
$\pi^-\mu^+\nu$	288 ± 29	0.0035	0.074 ± 0.008	$1.91^{+0.30}_{-0.15}$
$K^-\mu^+\nu$	220			
$\rho^-\mu^+\nu$	52 ± 6	0.0009	$VPS \times (0.085 \pm 0.001)$	
$K^0\pi^-\mu^+\nu$	145	0.0003		
$K^-\pi^0\mu^+\nu$	13	~ 0		
$c\bar{c}$ background	200 ± 20			

Table 6.2: Results obtained after applying the fit to the two dimensional $\cos\theta_l$ vs. q^2 distribution.

6.5 Measurement of $f_+^{\pi}(0)/f_+^{K}(0)$

Using the results from the fit, precisely the $\pi^-\mu^+\nu$ and $K^-\mu^+\nu$ yields, it is possible to extract the value of the form factor ratio[3] $f_+^{\pi}(0)/f_+^{K}(0)$. We begin by writing the ratio of the differential decay rates as:

$$\frac{d^2\Gamma(\pi\mu\nu)}{d^2\Gamma(K\mu\nu)} = \frac{dY(\pi\mu\nu)/\epsilon(q^2)_{\pi\mu\nu}}{dY(K\mu\nu)/\epsilon(q^2)_{K\mu\nu}} =$$

$$= \left|\frac{V_{cd}}{V_{cs}}\right|^2 \left|\frac{f_+^{\pi}(0)}{f_+^{K}(0)}\right|^2 \frac{[\frac{f_+(q^2)}{f_+(0)}(A + B\eta + C\eta^2)dE_l dq^2]_{\pi\mu\nu}}{[\frac{f_+(q^2)}{f_+(0)}(A + B\eta + C\eta^2)dE_l dq^2]_{K\mu\nu}}$$

where, integrating both sides, we find:

$$\frac{Y_{\pi\mu\nu}}{Y_{K\mu\nu}} = \left|\frac{V_{cd}}{V_{cs}}\right|^2 \left|\frac{f_+^{\pi}(0)}{f_+^{K}(0)}\right|^2 \frac{[\int_{E_l^{Min}}^{E_l^{Max}} dE_l \int_{q^2_{Min}(E_l)}^{q^2_{Max}(E_l)} dq^2 \frac{f_+(q^2)}{f_+(0)}(A + B\eta + C\eta^2)\epsilon(q^2)]_{\pi\mu\nu}}{[\int_{E_l^{Min}}^{E_l^{Max}} dE_l \int_{q^2_{Min}(E_l)}^{q^2_{Max}(E_l)} dq^2 \frac{f_+(q^2)}{f_+(0)}(A + B\eta + C\eta^2)\epsilon(q^2)]_{K\mu\nu}}.$$

(6.12)

[3] It should be noticed that we are not referring to the ratio $f_-(0)/f_+(0)$, but to the ratio of f_+-type form factors for $\pi^-\mu^+\nu$ and $K^-\mu^+\nu$.

$Y_{\pi\mu\nu}$ and $Y_{K\mu\nu}$ are the fitted yields for $\pi^-\mu^+\nu$ and $K^-\mu^+\nu$ respectively. A, B and C are the kinematic coefficients described in Chapter 1 and V_{cd} and V_{cs} are the CKM matrix elements for Cabibbo suppressed and Cabibbo allowed transitions.

To make the calculations we need to perform the numerical integral on the right-end side. This integral contains the reconstruction efficiency as a function of q^2 which we compute by dividing the sample in bins of q^2 and then computing the ratio between the number of reconstructed and the number of generated events in each bin. The efficiency distribution is then fit to a polynomial function which is used in the integration process. In practice, the efficiency will have a strong dependence on q^2, because the visible mass cut eliminates all the events at high q^2. It's possible to use a reasonably flat efficiency curve by applying the same visible mass cut on the generated events provided that the numerical integral is also computed for events that pass this cut.

6.5.1 Numerical Integration

The numerical integral is performed using a rejection method. First, pure phase space is generated, then we compute the rejection method based on the decay amplitude modulated by the reconstruction efficiency as shown in Eq. 6.12. The two variables we use to describe the decay are the hadron energy E_h and the lepton energy E_μ in the D^0 rest frame. These are randomly generated within their kinematic range:

$$m_\mu < E_\mu < \frac{m_D^2 + m_\mu^2 - m_h^2}{2m_D^2} \qquad\qquad m_h < E_h < \frac{m_D^2 + m_h^2 - m_\mu^2}{2m_D^2}$$

An event generated in this two-dimensional (E_μ,E_h) space is kept only if it falls within the Dalitz boundaries:

$$
\begin{aligned}
E_\mu^{min} &\equiv \frac{1}{2}\frac{\mathcal{A}^2 + m_\mu^2}{\mathcal{A}} < E_\mu < E_\mu^{max} \equiv \frac{1}{2}\frac{\mathcal{B}^2 + m_\mu^2}{\mathcal{B}} \\
E_h^{min} &\equiv \frac{1}{2}\frac{\mathcal{C}^2 + m_h^2}{\mathcal{C}} < E_h < E_h^{max} \equiv \frac{1}{2}\frac{\mathcal{D}^2 + m_h^2}{\mathcal{D}}
\end{aligned}
$$

where $\mathcal{A}$, $\mathcal{B}$, $\mathcal{C}$ and $\mathcal{D}$ are defined as:

$$
\begin{aligned}
\mathcal{A} &= m_D - E_h - \sqrt{E_h^2 - m_h^2} \\
\mathcal{B} &= m_D - E_h + \sqrt{E_h^2 - m_h^2} \\
\mathcal{C} &= m_D - E_\mu - \sqrt{E_\mu^2 - m_\mu^2} \\
\mathcal{D} &= m_D - E_\mu + \sqrt{E_\mu^2 - m_\mu^2}
\end{aligned}
$$

It should be noticed that both E_μ^{max} (E_h^{max}) and E_μ^{min} (E_h^{min}) are function of the hadron energy E_h (lepton energy E_μ) and define the contour of the Dalitz plot. From the hadron energy E_h, the value for the efficiency is obtained using the formula:

$$\epsilon(q^2) = P_1 + P_2 q^2 + P_3 q^2 \tag{6.13}$$

where $q^2 = m_D^2 + m_h^2 - 2m_D E_h$ with $h = K$ or π and P_i are parameters from the fit to the efficiency (see Fig. 6.8). The intensity I is computed so that the "effective intensity" $I' = I \times \epsilon(q^2)$ (which represents the argument of the integral) can be found. If a generated event survives the visible mass cut, the corresponding amplitude is compared to a random number generated between zero and the maximum allowed amplitude. If the random number is smaller, we keep the event. The numerical integral is given by:

$$\int (...) = \frac{N_{ACC}}{N_{GEN}} \times I'_{Max} \times (E_\mu^{max} - E_{mu}^{min}) \times (q^2_{max} - q^2_{min}) \tag{6.14}$$

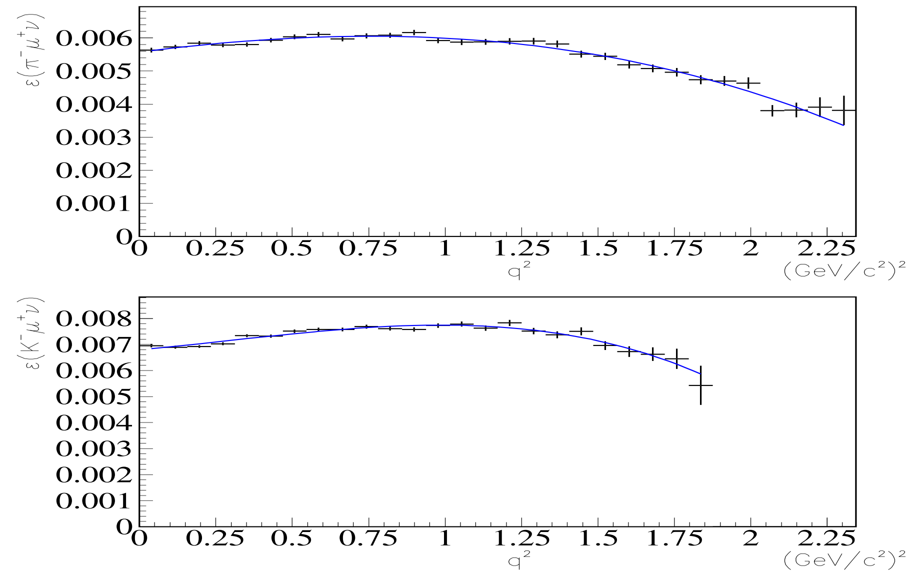

Figure 6.8: Fit to the efficiency as a function of the q^2 for both $D^0 \to \pi^-\mu^+\nu$ (top) and $D^0 \to \pi^-\mu^+\nu$ (bottom).

where N_{ACC} is the number of accepted events and N_{GEN} is the number of generated events. In Fig. 6.9 we show the Dalitz plot of the q^2 versus the visible mass squared before any rejection (pure phase-space) and the same Dalitz plot after a rejection on the basis of the efficiency modulated intensity $I' = I \times \epsilon(q^2)$.

From the numerical integration and using the $\pi^-\mu^+\nu$ and $K^-\mu^+\nu$ yields from the fit we find the ratio:

$$\left|\frac{V_{cd}}{V_{cs}}\right|^2 \left|\frac{f_+^\pi(0)}{f_+^K(0)}\right|^2 = 0.037 \pm 0.004\ (stat.). \tag{6.15}$$

Using the PDG result [39] $|V_{cd}/V_{cs}|^2 = 0.051 \pm 0.001$, derived by imposing the orthogonality of the first two rows of the CKM matrix, we can extract the ratio of the form factors in the maximum recoil configuration ($q^2 = 0$) to be:

$$\left|\frac{f_+^\pi(0)}{f_+^K(0)}\right|^2 = 0.85 \pm 0.04\ (stat.) \pm 0.01\ (CKM) \tag{6.16}$$

where the last error is associated to the error on the CKM matrix elements ratio.

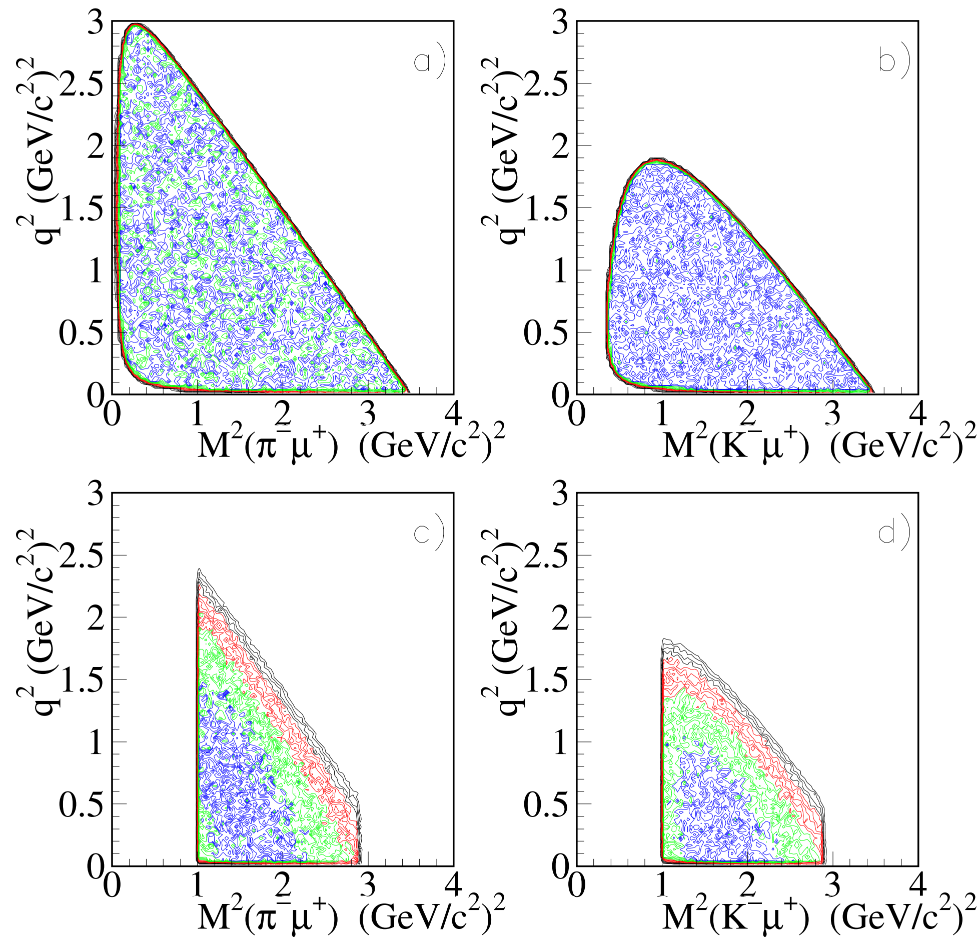

Figure 6.9: a), b) Phase-space before rejection. c), d) Dalitz after rejection on the intensity I'. The left and right columns refer to $\pi^-\mu^+\nu$ and $K^-\mu^+\nu$ respectively.

Chapter 7

Systematic Studies

In the previous chapter we described the analysis technique that we use to measure the relative branching ratio, the pole masses, the ratio $f_-^K(0)/f_+^K(0)$ and the ratio $f_+^\pi(0)/f_+^K(0)$. The errors associated with these quantities are so far only statistical. In this chapter we present the systematic studies performed on the $\pi^-\mu^+\nu$ and $K^-\mu^+\nu$ samples to test the accuracy of our results and the assumptions on which the analysis relies. These studies are so divided:

- Fits to the $c\bar{c}$ Monte Carlo sample to test the overall analysis procedure.
- Stability of the results versus different cut combinations.
- A different fit approach.
- Data fluctuation test: we performed this study to investigate the accuracy of the errors reported by the fit.
- Mini Monte Carlo test: this study allows us to test the goodness of fit, i.e. how well our fit function represents the data.
- Fit variations that test equally probable results.
- Test of the $K \to \pi$ misidentification rate. Since the fit relies on the simulated $K \to \pi$ misidentification rate, we use high statistics D^0 decays to test the match to the data.

7.1 Testing the Fit on a $c\bar{c}$ Monte Carlo

We perform a test fitting a $c\bar{c}$ Monte Carlo sample consisting of 20 times the FOCUS statistics. This sample has a known relative branching ratio $\Gamma(\pi^-\mu^+\nu)/\Gamma(K^-\mu^+\nu)$ and known pole masses. Therefore we can assess the correctness of the fit and investigate possible problems in the reconstruction or selection routines. Using the selection criteria reported in Table 5.1 and scanning over 8 different values of the significance of separation L/σ_L, we fit the $c\bar{c}$ Monte Carlo sample using the procedure described in Chapter 6. The results for the branching ratio and the pole masses are shown in Fig. 7.1.

Even with a statistical error which is about 5 times smaller than what we expect in the fit to the data we are able to measure the Monte Carlo input parameters with good accuracy. The fitting procedure can therefore be considered reliable.

7.2 Cut Variations

We tested a variety of selection cuts to investigate the stability of the results. The variations are made changing one by one the most important cuts applied on the sample. We investigate possible problems related to Čerenkov identification, vertex confidence level, significance of separation between the primary and the secondary vertex, muon identification, and hadrons and muon momenta. In Table 7.2 we show the correspondence between each variation name and the actual cuts applied.

We investigate possible systematic effects by looking directly at the branching ratios and the pole masses as well as at other variables like the efficiency corrected yields[1] and the returned $\rho^-\mu^+\nu$ to $K^*(892)^-\mu^+\nu$ branching ratio which is the most poorly known constraint in the fit (see Eq. 6.8). In Fig. 7.2 we show the efficiency

[1] The efficiency corrected yield is defined as the ratio between the data yield and the reconstruction efficiency. The efficiency is computed as the ratio between the number of reconstructed events divided by the number of generated.

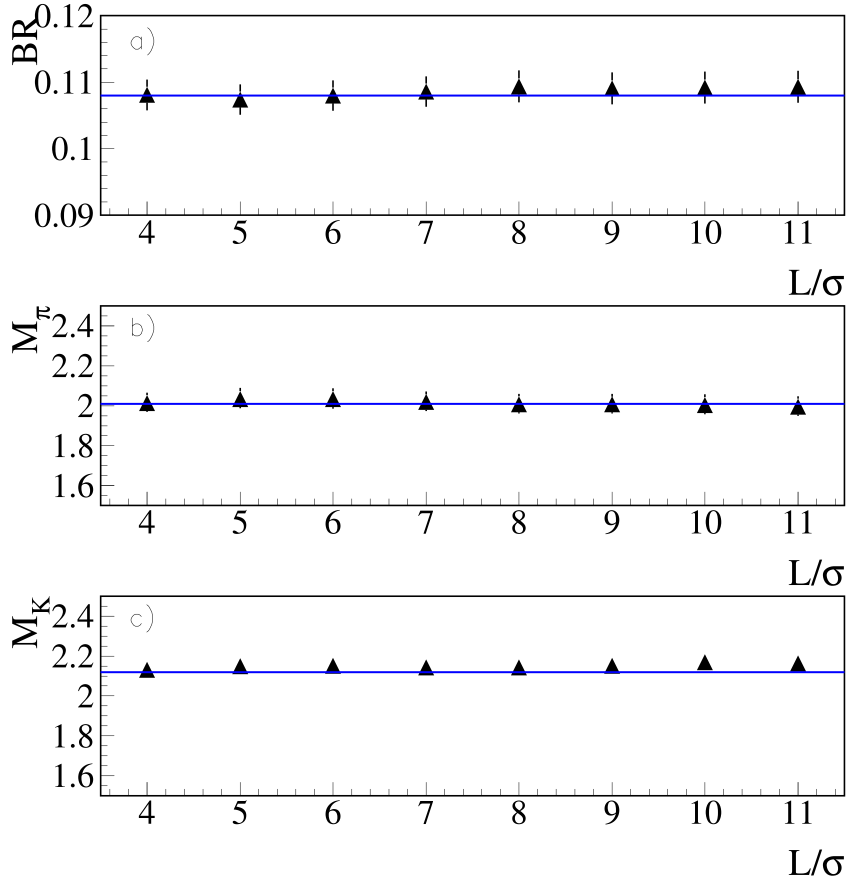

Figure 7.1: Fit to the $c\bar{c}$ Monte Carlo sample for eight different L/σ values. The blue line represent the input value in the FOCUS Monte Carlo. a) Relative branching ratio of $\pi^-\mu^+\nu$ to $K^-\mu^+\nu$. b) $\pi^-\mu^+\nu$ pole mass. c) $K^-\mu^+\nu$ pole mass.

corrected yields for the two modes $K^-\mu^+\nu$ and $\pi^-\mu^+\nu$ and the relative branching ratio. The results are very stable and suggest that the Monte Carlo models the data well.

In Fig. 7.3 we show the returned branching ratio of the decay mode $\rho^-\mu^+\nu$ relative to $K^*(892)^-\mu^+\nu$. It should be remembered that in the fit, this branching ratio is "weakly constrained" by its error through a χ^2 term. Nevertheless the fit does not show any significant shift from the input value.

Finally, we show the results for the pole masses and the form factor ratio $f_-^K(0)/f_+^K(0)$ in Fig. 7.4. Also in this case there is good agreement between different selection criteria.[2]

NAME	CUT
BL	see Table 5.1
SP4	BL+ Soft pion momentum cut greater than 4 GeV/c
WPK5	BL+ $W(K) - W(\pi) > 5$ for $\pi\mu\nu$
CLMU	BL+ $CL_\mu > 15\%$
CLS	BL+ $CLS > 15\%$
OOM2	BL+ $OOM > 2$ for secondary vertex
PKA25	BL+ Hadron from D^0 momentum > 25 GeV/c
PMU25	BL+ Muon from D^0 momentum > 25 GeV/c
LSIG	BL+ $L/\sigma > 11$
PSPI	BL+ TrackFit $C.L. > 15\%$
VM	scan on visible mass 0.85 $\rightarrow$ 1.25 in steps of 0.05 GeV/c^2

Table 7.1: Most important cut variations names and corresponding selection cuts. BL refers to the BaseLine set of cuts.

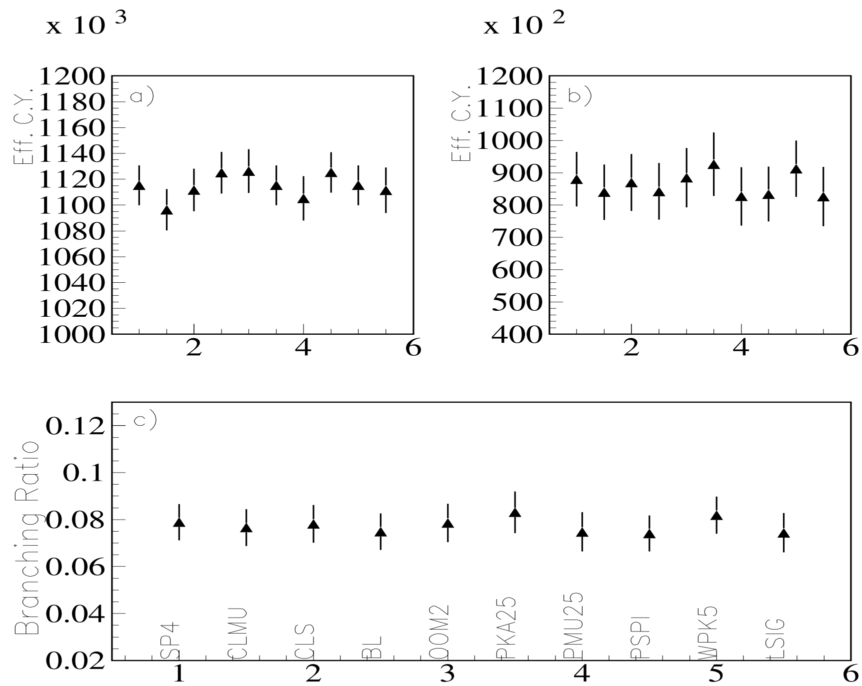

Figure 7.2: Cut variations: a) Efficiency corrected yields for $D^0 \rightarrow K^-\mu^+\nu$. b) Efficiency corrected yield for $D^0 \rightarrow \pi^-\mu^+\nu$. c) Relative branching ratio of $D^0 \rightarrow \pi^-\mu^+\nu$ to $D^0 \rightarrow K^-\mu^+\nu$.

[2] The most interesting result is given by the $K^-\mu^+\nu$ pole mass which is systematically lower than the nominal value (the $D_s^*(2114)$ mass) by about 4 to 5 standard deviations. This clearly illustrates how the pole dominance parametrization of the form factors fails to describe our data.

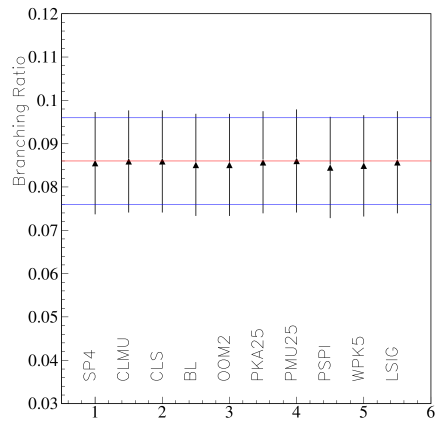

Figure 7.3: $\rho^-\mu^+\nu$ to $K^*(892)^-\mu^+\nu$ branching ratio. The blue and red lines show the input value in the weak constraint with relative error. The fit always returns a branching ratio which is consistent with the input value.

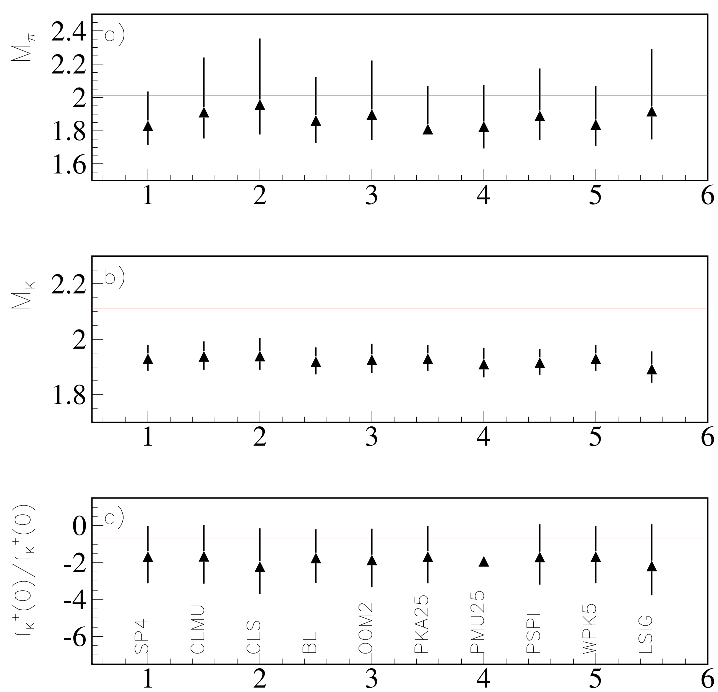

Figure 7.4: Cut variations. The nominal value for these parameters is given by the red line. a) Pole mass for $\pi^-\mu^+\nu$. b) Pole mass for $K^-\mu^+\nu$. c) Ratio $f_-^K(0)/f_+^K(0)$ for $K^-\mu^+\nu$. In all cases the results are consistent with each other. In particular the $K^-\mu^+\nu$ pole mass is statistically inconsistent with the nominal pole at 2.114 GeV/c^2. Notice that the fit corresponding to the variation PMU25 (muon momentum greater than 25 GeV/c) failed to find the asymmetric errors.

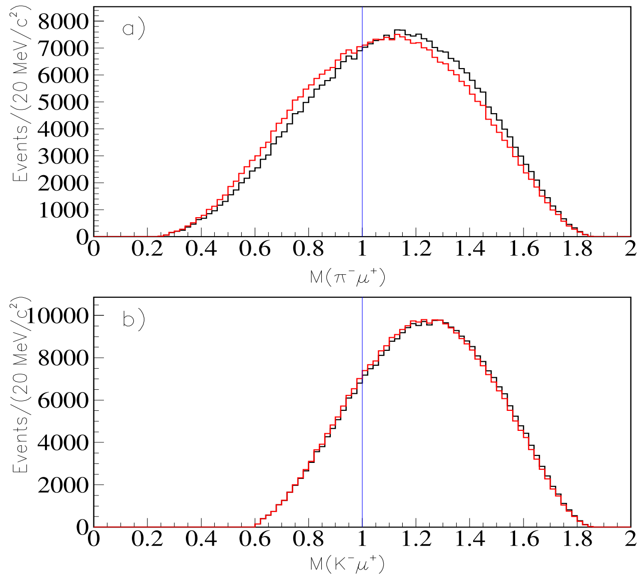

Figure 7.5: Visible mass distributions for different pole masses. a) $\pi^-\mu^+$ invariant mass distribution for a pole mass equal to 2.10 GeV/c^2 (black) and 1.90 GeV/c^2 (red). b) $K^-\mu^+$ invariant mass distribution for a pole mass equal to 2.10 GeV/c^2 (black) and 1.90 GeV/c^2 (red). The decay $D^0 \to \pi^-\mu^+\nu$ is more sensitive to the choice of the pole mass due to the large q^2 reach that better probes the "real pole".

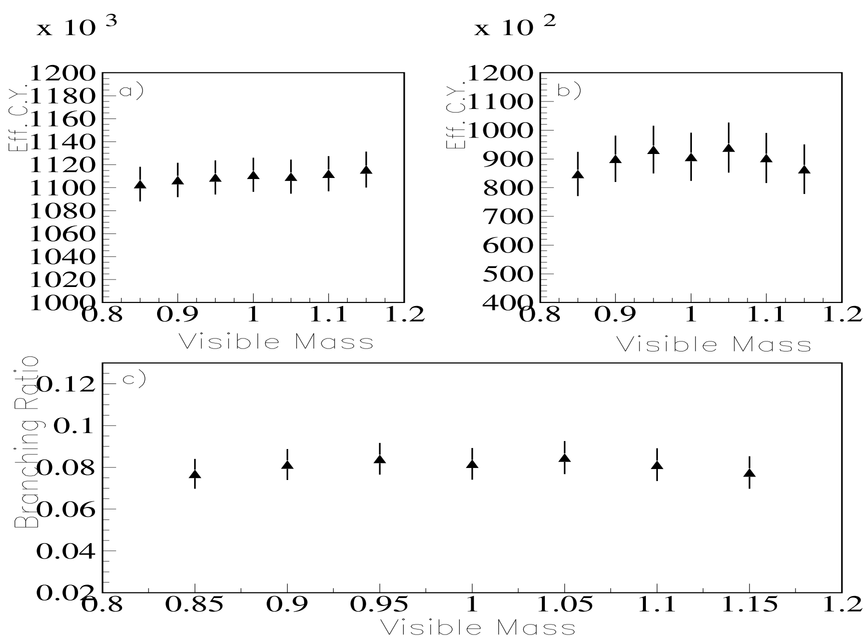

Figure 7.6: Branching ratio for different visible mass cuts.

Additional checks have been performed on the two samples. Given the big back-

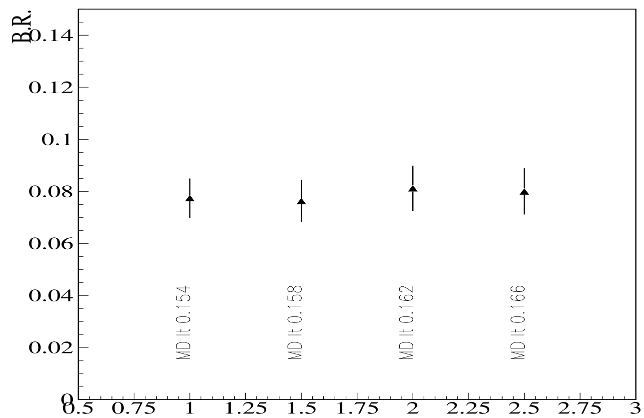

Figure 7.7: $\Gamma(\pi^-\mu^+\nu)/\Gamma(K^-\mu^+\nu)$ branching ratio for different $D^{*+}-D^0$ mass difference cuts.

grounds from decays with missing particles we were forced to apply a visible mass cut on the sample at 1 GeV/c^2 . A good reason to further investigate this cut is shown in Fig. 7.5 where we can appreciate how the $\pi^-\mu^+$ visible mass distribution changes with the pole mass value. The FOCUS Monte Carlo is generated using the nominal pole masses therefore one must quantify the effect due to a possible mismatch with the data. A wide range of visible mass cuts have been tested and the results are shown in Fig. 7.6. The scan on the visible mass cut shows consistent results and therefore we can safely choose a mass cut at 1 GeV/c^2 .

We mentioned that the fit to the $\cos\theta_l$ and q^2 distributions is performed after we applied a cut on the $D^{*+} - D^0$ mass difference. This has the advantage of highly reducing combinatoric background as well as the contamination from $D^0 \rightarrow \rho^-\mu^+\nu$ and $D^0 \rightarrow K^*(892)^-\mu^+\nu$ for which the signal region is broader in the $D^{*+} - D^0$ mass difference distribution compared to $D^0 \rightarrow \pi^-\mu^+\nu$. We must check that the Monte Carlo properly simulates these background distributions and we have to make sure that we do not introduce any bias when placing this cut. We decided to test the effect of the mass difference cut (the default value is at 0.154 GeV/c^2) on the branching ratio by recomputing the measurement increasing the mass window by 4 MeV/c^2 each time.

In Fig. 7.7 we show the branching ratio for four different cuts, the results are again consistent. We conclude that from cut variation we find no significant deviations from the baseline set of cuts.

7.3 Assessing Errors and Goodness of Fit

In this section we describe two different studies based on the fluctuation of the data distribution and of the fit function. The first study aims to address the accuracy of the statistical error returned by the fit as well as to check for possible biases on the central value. A flow diagram of this study is shown in Fig. 7.8 a). The second study is performed to investigate how well the fit function represents the data [33]. The flow diagram, in this case, is shown in Fig. 7.8 b).

7.3.1 Data Fluctuations Study

We performed a study using fluctuated data to assess the correctness of the errors reported by the fit procedure. Starting from the data sample, after all the selection cuts were applied, we fluctuated each bin independently according to a Poisson distribution with central value equal to the bin yield. Since the fit is done on a 2-dimensional distribution and since a fit to the mass difference is also performed in order to assess the amount of combinatoric background, we must fluctuate a three dimensional array that for each event saves its q^2, the $D^{*+} - D^0$ mass difference, and its $\cos\theta_l$. Once we obtained a sample of fluctuated data, we fit each data set and we save the fit results. The distribution of these fit parameters is compared to what we obtain in the standard fit to the unfluctuated data (Fig. 7.9). We expect a spread in the results consistent with the statistical error, while any deviation must be considered in the computation of the systematic error. We also expect the mean of the distribution to be consistent with our measurement. From the fit to the branching ratio distribution to a single Gaussian we

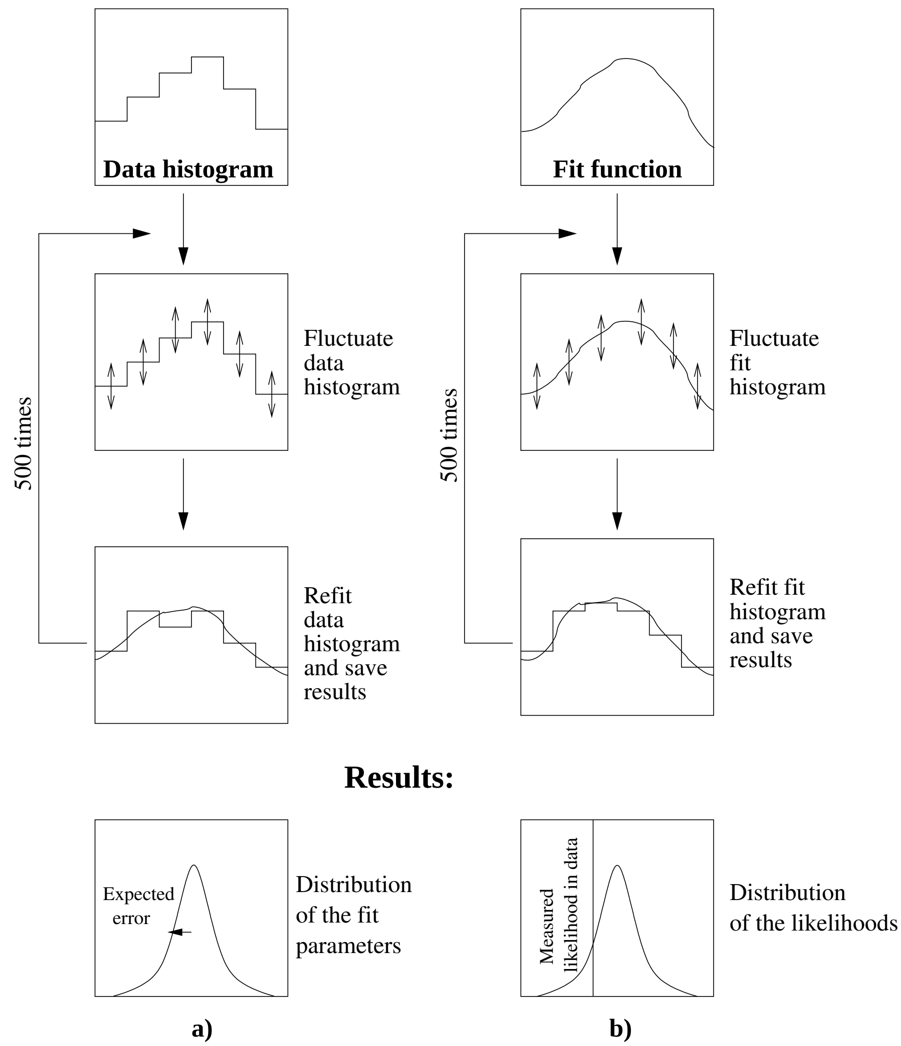

Figure 7.8: The diagrams show the test made to assess the accuracy of the statistical error (a) and of the goodness of fit (b).

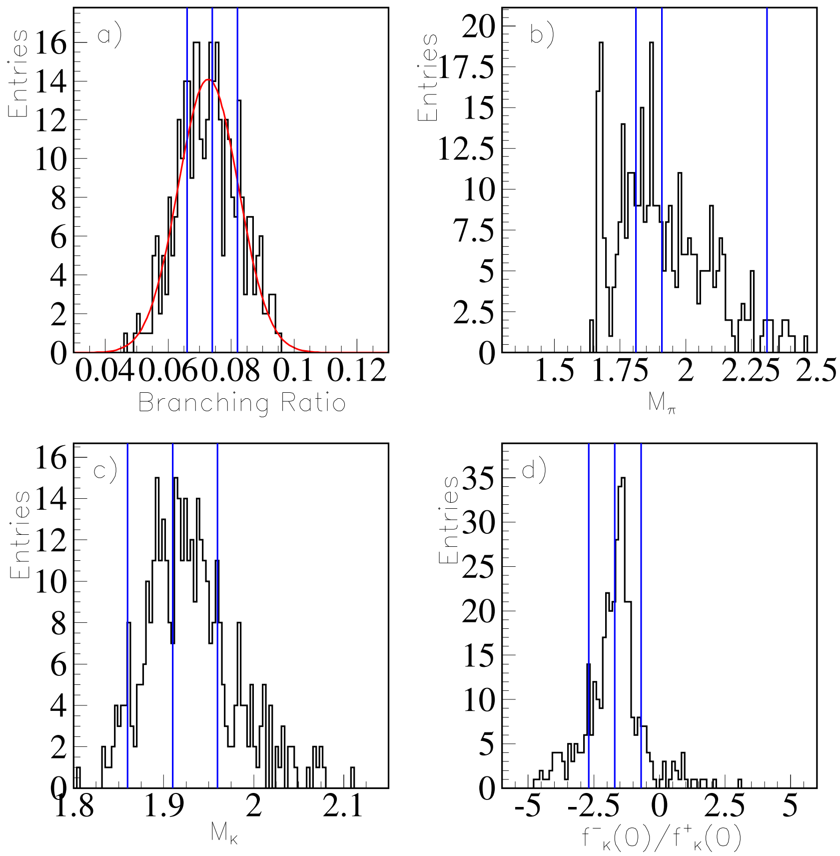

Figure 7.9: These distributions are obtained by fluctuating 500 times the data distributions and fitting each "new" data set following the procedure described in chapter 6. The blue lines show the measured value with relative error ($\pm 1\sigma$) in the fit to the unfluctuated data. a) Branching ratio results: the red curve is the fit of the distribution to a Gaussian shape. b) $\pi^-\mu^+\nu$ pole mass: the plot shows a small pile up of events at the low end tail of the distribution. This effect is an artifact of the fit and is due to the large statistical error on the $\pi^-\mu^+\nu$ pole mass. It reflects the singularity of the pole dominance parametrization of the form factor. c) $K^-\mu^+\nu$ pole mass, d) form factor ratio $f_-^K(0)/f_+^K(0)$.

find evidence for a small bias in the statistical error returned by the fit. The width of the Gaussian is 0.095 ± 0.003 compared to the quoted statistical error of ± 0.08. This is probably due to the fact that the amount of $K^-\mu^+\nu$ in the $\pi^-\mu^+\nu$ background is estimated from the fit to the $K^-\mu^+\nu$ and it is not allowed to float in the $\pi^-\mu^+\nu$ fit. This causes the statistical error to be underestimated due to the fact that the error matrix does not account for the correlation between the signal and this background.

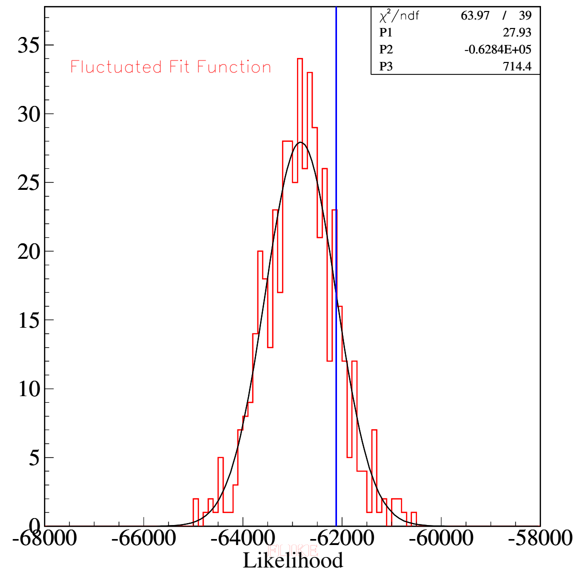

Figure 7.10: The red distribution is obtained by fluctuating the fit function obtained by the fit on the mass difference and q^2. The fit is obtained using a Gaussian: the parameters p1, p2, and p3 represent the amplitude, the mean and the σ of the Gaussian, respectively. The blue line, which indicates the likelihood value returned by the fit to the data is fully compatible with the red distribution.

We will account for this bias by adding a contribution to the systematic error. We find no evidence for a significant bias in the central values.

7.3.2 Fit Function Fluctuations Study

The next study is analogous to what we described in the section 7.3.1, but involves fluctuating the fit function rather than the data distribution. The test now is to compare the distribution of the expected likelihoods obtained from the fit to the fluctuated fit function and the likelihood obtained in the fit to the data. If we obtain consistent results, the fit function well represents the data distribution. In Fig. 7.10, the red distribution is the distribution of the likelihoods obtained by fluctuating the Monte Carlo fit function. The fit has been performed using one Gaussian. The blue line represents the measured likelihood when we fit to the unfluctuated data and it is fully compatible with Gaussian width. We conclude that the fit function correctly represents the data.

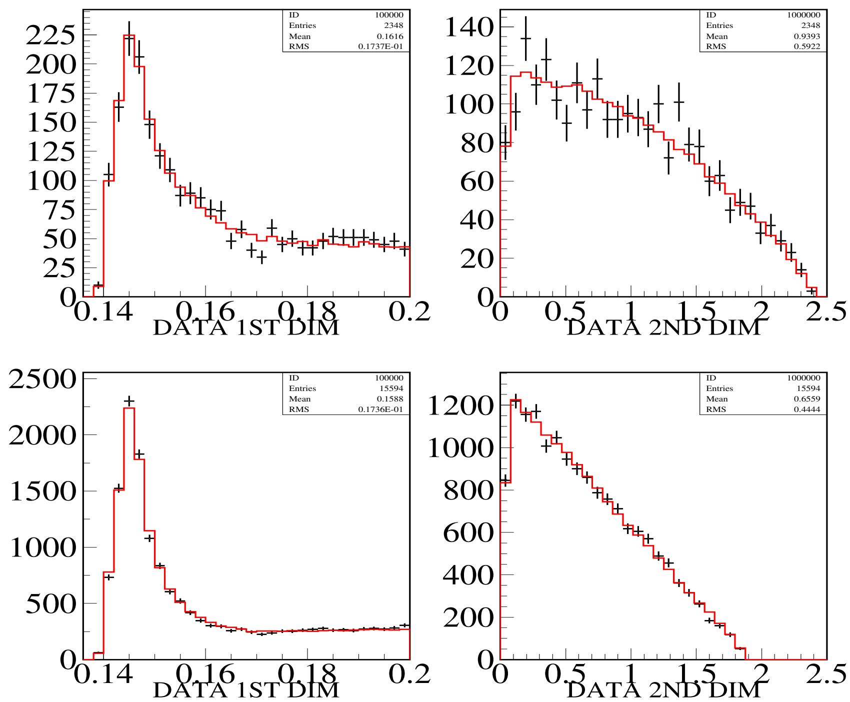

Figure 7.11: Projections of the fit to the $D^{*+}-D^0$ mass difference vs. q^2 two-dimensional distribution. The top row shows the $\pi^-\mu^+\nu$ projections while the bottom row shows the $K^-\mu^+\nu$ projections.

7.4 A Different Fit Approach

We decided to use an alternative technique in which we fit the $K^-\mu^+\nu$ and $\pi^-\mu^+\nu$ distributions simultaneously. The overall amplitude of the the $K^-\mu^+\nu$ and the $K^*(892)^-\mu^+\nu$ contributions are "free" to float, but the relative amounts in the Cabibbo suppressed and in the Cabibbo allowed samples are still fixed to the misidentification rate returned by the Monte Carlo. The function that is minimized is a negative log-likelihood of the form:

$$F = -2\ log(\mathcal{L}_{\pi\mu\nu}) - 2\ log(\mathcal{L}_{K\mu\nu}) + \chi_1^2 + \chi_2^2 \tag{7.1}$$

where we added the two constraints on the vector to pseudoscalar and the $\rho^-\mu^+\nu$ to $K^*(892)^-\mu^+\nu$ branching ratios in the form of χ^2 terms. In Fig. 7.11 we show the fit to the $D^{*+} - D^0$ mass difference and the q^2 distributions. These results are consistent with the standard fit results and are presented in Fig. 7.12 for eight different L/σ cuts.

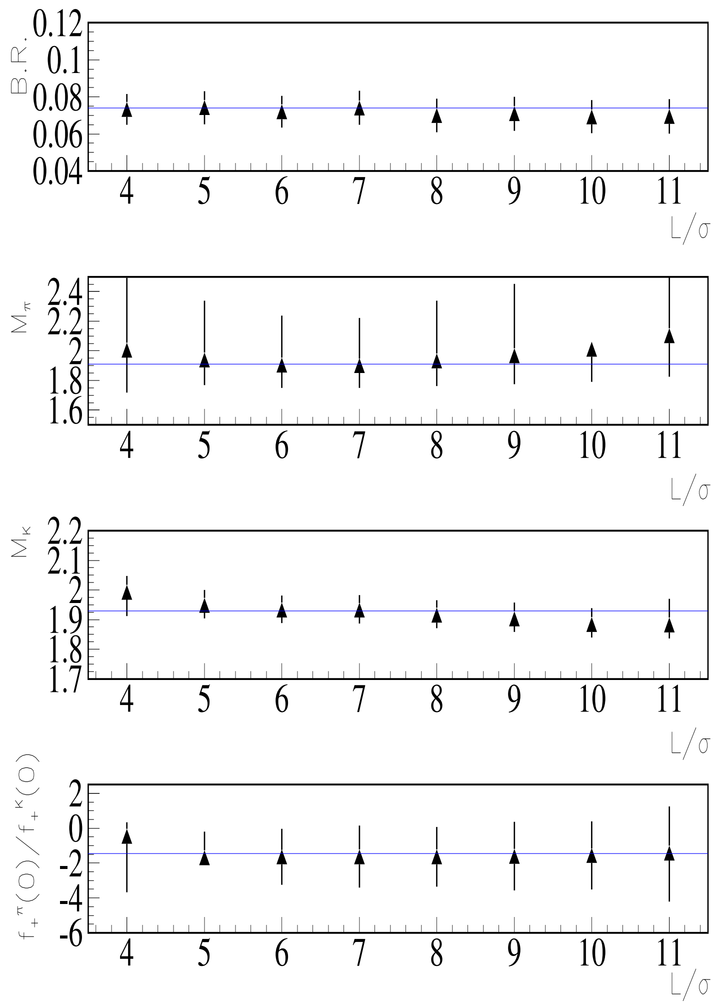

Figure 7.12: Fit results using a fit to the $D^{*+} - D^0$ mass difference and q^2 fit. The results are in good agreement with the results obtained in the standard fit (blue line).

The results are considered fit variations and are included in the computation of the systematic uncertainty. Other fit variations have been performed. Namely, we fit the distributions with different bin sizes and we test the response of the fit when we inflate the error on both the penalty terms by 20%. As far as bin size is concerned, the standard distribution uses 15 bins in q^2 and 15 bins in $\cos\theta_l$ (15×15). We also performed a test using 15×8 and 32×32 bins.

7.5 $K - \pi$ misidentification.

The fitting procedure uses the Monte Carlo misidentification rate to determine the amount of $K^- \mu^+ \nu$ background in the $\pi^- \mu^+ \nu$ sample. This is a background component in the decay $\pi^- \mu^+ \nu$ sample that is nearly identical to the signal shape in both the q^2 and the $\cos \theta_l$ projections. We have to rely on Čerenkov identification to separate the signal from this background. Further, given the high statistics of the $D^0 \to K^- \mu^+ \nu$ sample, a small mismatch between the real misidentification rate and the Monte Carlo simulated rate can dramatically change the amount of background in the $D^0 \to \pi^- \mu^+ \nu$ sample.

The first test of the misidentification rate is to investigate the evolution of the branching ratio on a wide range of $K - \pi$ Čerenkov separation cuts. We tested five different cuts corresponding to a piconicity $(W(K) - W(\pi))$ greater than 1, 3, 5, 7, and 9. The branching ratio results are presented in Fig. 7.13 and show an evident drop in the branching ratio when the $K^- \mu^+ \nu$ contamination is highly suppressed. This result suggests that the misidentification rate in the Monte Carlo is underestimated.

To further investigate this problem we use data from a skim which selects high statistics charm decays without any requirement on the Čerenkov identification. We perform this study using the two decays $D^0 \to K^- \pi^+$ and $D^+ \to K^- \pi^+ \pi^+$ where the same momentum cut, used on the semileptonic mode (14 GeV/c), has been applied on the candidate kaon. To minimize possible biases we use most of the requirements used to select the hadron particle in the semileptonic decays. Further, the decay $D^0 \to K^- \pi^+$ is reconstructed requiring a tagging pion in a manner similar to the semileptonic decay and by using the DVFREE routine to find the primary vertex. We tag the kaon by fitting the two-body and three-body invariant masses which are shown in Figs. 7.14 and 7.15, respectively. We use a single Gaussian for the signal region and a second degree polynomial for the background for both the data and the Monte Carlo. The

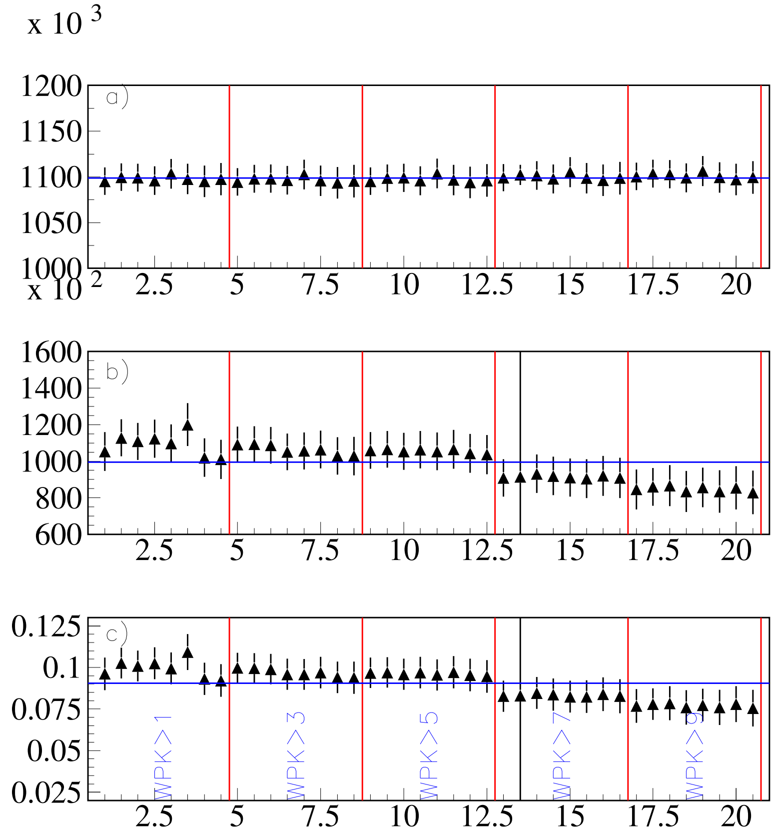

Figure 7.13: Efficiency corrected yields and branching ratio versus piconicity. a) $D^0 \to K^-\mu^+\nu$ efficiency corrected yields b) $D^0 \to \pi^-\mu^+\nu$ efficiency corrected yields c) Relative branching ratio (in scan of L/σ). For each piconicity cut we scan over eight L/σ values. The main source of misidentification in $K^-\mu^+\nu$ comes from $\pi^-\mu^+\nu$ decays. The trend on the branching ratio and the $\pi^-\mu^+\nu$ efficiency corrected yields is consistent with an underestimation of the misidentification rate in the FOCUS Monte Carlo.

resolution is good enough so that we can discriminate between signal and backgrounds. In the $D^0 \to K^-\pi^+$ invariant mass, the big distortion in the background is caused by $D^0 \to \pi^+\pi^-$ decays. To select $D^+ \to K^-\pi^+\pi^+$ events we added an isolation cut on the primary vertex that requires that no tracks from the secondary vertex be consistent with originating from the primary vertex with a confidence level greater than 1%. This requirement rejects contamination from $D^{*+} \to \pi^+ D^0$ with the D^0 decaying to $K^-\pi^+$.

In Fig. 7.16 we show the actual misidentification rate in data and Monte Carlo where we can confirm that the misidentification rate is underestimated in the Monte Carlo. A better estimation is presented in Fig. 7.17 where we show the ratio of misiden-

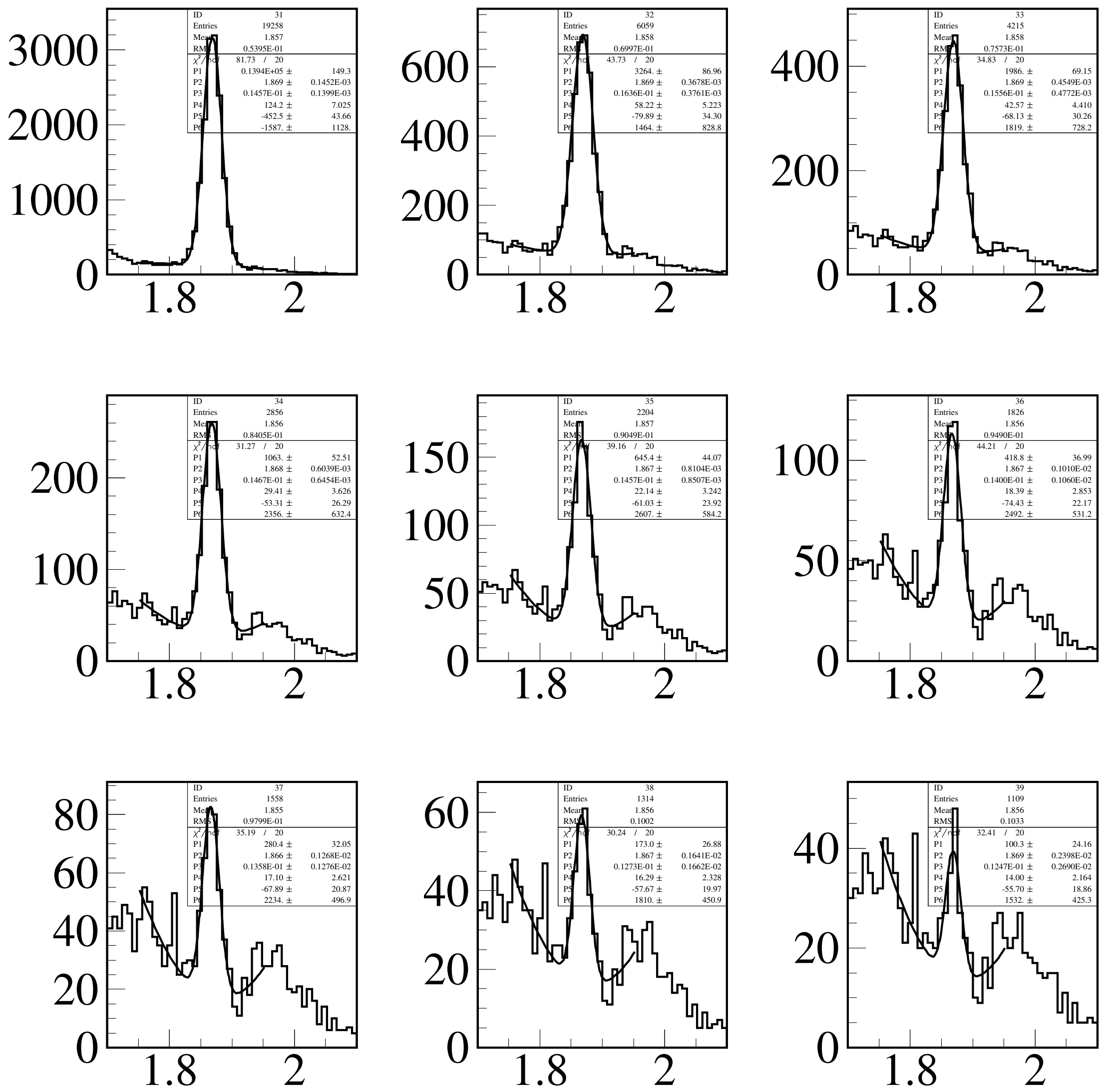

Figure 7.14: $K^{-}\pi^{+}$ invariant mass distributions for events that satisfy a D^{*}-tag and lie between 0.143 and 0.149 GeV/c^2. The fit is performed using a single Gaussian for the signal and a second degree polynomial for the background. The first plot on the top left does not have any Čerenkov requirement while on the following distributions we apply a piconicity cut on the kaon track of -1, 0, 1, 2, 3, 4, 5 and 6.

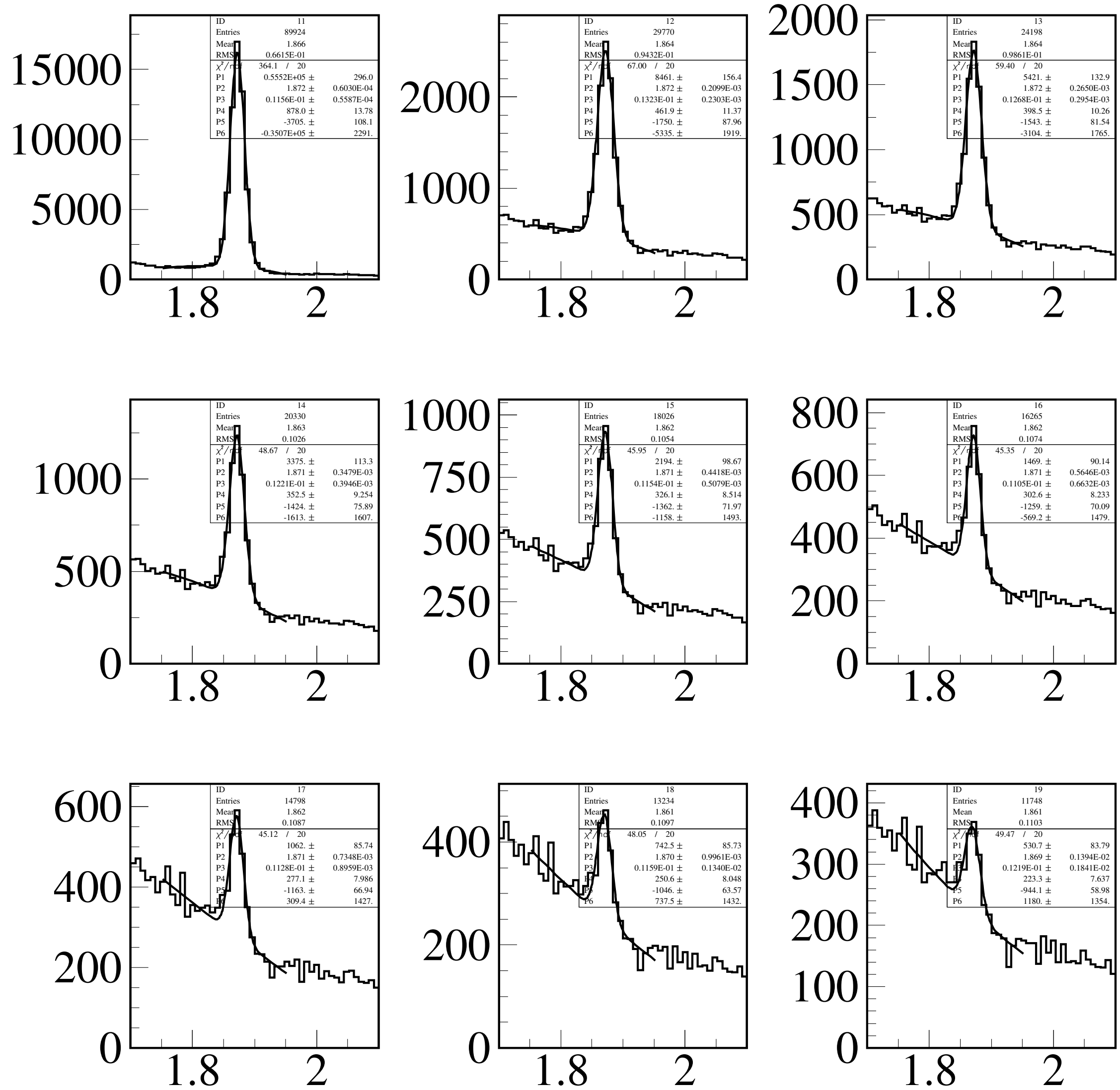

Figure 7.15: $K^-\pi^+\pi^+$ invariant mass distributions. The fit is performed using a single Gaussian for the signal and a second degree polynomial for the background. The first plot on the top left does not have any Čerenkov requirement while on the following distributions we apply a piconicity cut on the kaon track of -1, 2, 3, 4, 5 and 6.

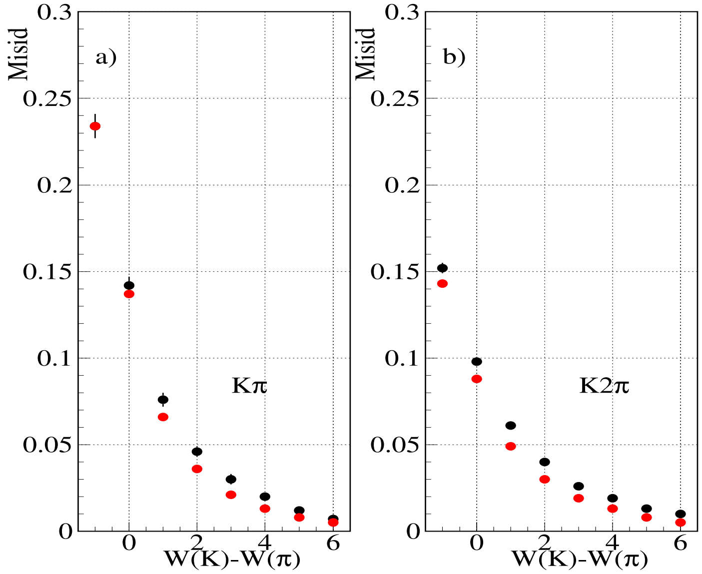

Figure 7.16: Actual misidentification in data (black) and Monte Carlo (red) for: a) $D^0 \to K^-\pi^+$ and b) $D^0 \to K^-\pi^+\pi^+$.

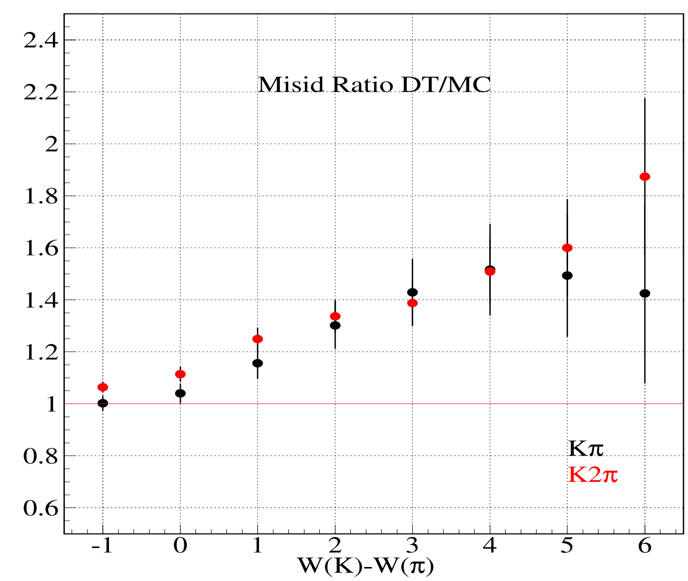

Figure 7.17: The ratio of the misidentification rate between data and Monte Carlo for different piconicity cuts.

tification between data and Monte Carlo for several different piconicity requirements on the kaon. The discrepancy between data and Monte Carlo is evident. At the standard

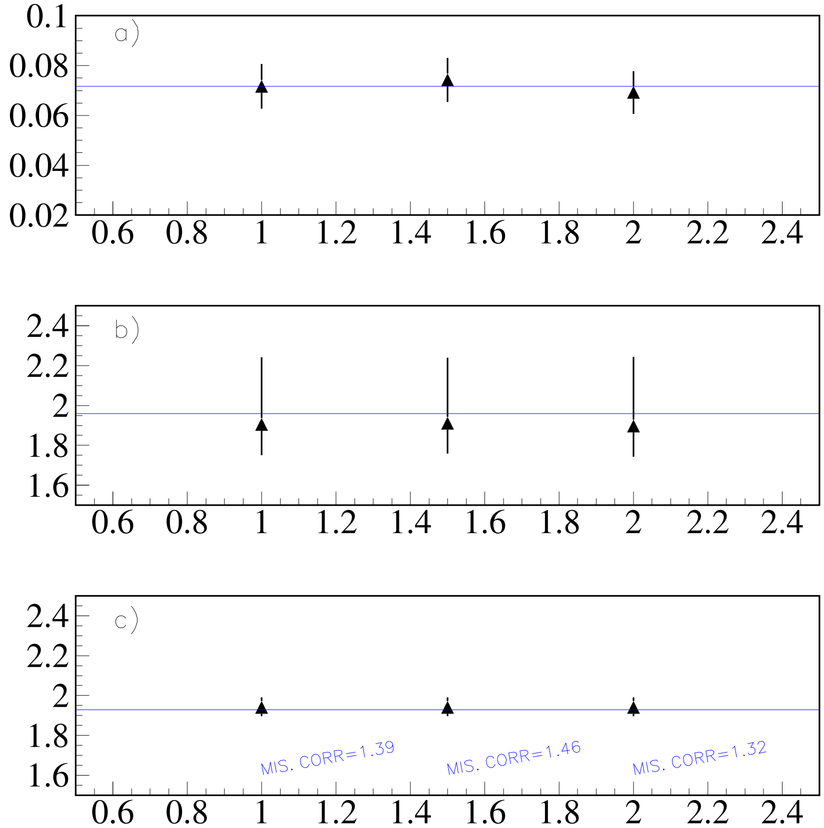

Figure 7.18: a) Relative branching ratio. b) $\pi^-\mu^+\nu$ pole mass. c) $K^-\mu^+\nu$ pole mass. We tested the dependence of these parameters from the $K \to \pi$ misidentification rate. We varied the correction to the Monte Carlo of $\pm 1\sigma$ where σ is given by the statistical uncertainty obtained from the study performed on D decays to $K^-\pi^+$ and $K^-\pi^+\pi^+$. For each tested parameter, the three points correspond to a misidentification rate correction of 1.39, 1.46, and 1.32, respectively.

cut of $W(K) - W(\pi) > 3$ we find that the Monte Carlo underestimates the amount of misidentification by about 40%.

We decided to correct the misidentification rate given by the efficiency ratio $\epsilon([K^- \to \pi^-]\mu^+\nu)/\epsilon(K^-\mu^+\nu)$ by introducing a multiplicative factor equal to 1.39 ± 0.07 (corresponding to the combined $D^0 \to K^-\pi^+$ and $D^0 \to K^-\pi^+\pi^+$ plots). We obtain results compatible with those obtained using a very tight $K - \pi$ separation cut, in which the amount of $K^-\mu^+\nu$ backgrounds is negligible (see Fig. 7.13). To quote a systematic uncertainty on the level of misidentification we use the statistical error of the combined sample of $D^0 \to K^-\pi^+$ and $D^+ \to K^-\pi^+\pi^+$. In Fig. 7.18 the change in the branching ratio, the pole masses and the $K^-\mu^+\nu$ form factor ratio is shown when we change the misidentification rate by $\pm 1\sigma$. The results are in agreement showing that the branching ratio does not depend strongly on the exact value of the misidentification rate.

7.6 Systematic error on $f_+^\pi(0)/f_+^K(0)$

We described in Chapter 6 how we measure the form factor ratio $f_+^\pi(0)/f_+^K(0)$ using the yields obtained from the fit. From the same equation (Eq. 6.12) we can extract the contribution to the systematic uncertainty on the form factor ratio which corresponds to a given contribution in the branching ratio. The only additional source of systematic uncertainty is given by the fit of the efficiency as a function of q^2. The $f_+^\pi(0)/f_+^K(0)$ central value is computed using 32 bins in q^2 and fitting the efficiency distribution with a third degree polynomial. Fit variations include a smaller binning (10 bins in q^2) and a different polynomial, namely a second and a fourth degree polynomial. Adding in quadrature the systematic uncertainties from the branching ratio measurement (properly rescaled) and from the fit variations on the efficiency, we quote the final results:

$$\left|\frac{V_{cd}}{V_{cs}}\right|^2 \left|\frac{f_+^\pi(0)}{f_+^K(0)}\right|^2 = 0.037 \pm 0.004\ (stat.) \pm 0.004\ (sys.). \tag{7.2}$$

Using the PDG value $|V_{cd}/V_{cs}|^2 = 0.051 \pm 0.01$, we find

$$\frac{f_+^\pi(0)}{f_+^K(0)} = 0.85 \pm 0.04\ (stat.) \pm 0.04\ (sys.) \pm 0.01\ (\mathrm{CKM}). \tag{7.3}$$

7.7 Conclusions

All the systematic studies have been performed using the misidentification correction factor found using golden modes $D^0 \to K^-\pi^+$ and $D^+ \to K^-\pi^+\pi^+$. These studies include:

- Cut variations: include variation of selection cuts: out of material, muon confidence level, secondary vertex confidence level, hadron momentum, muon momentum, L/σ, soft pion momentum.

- Fit variations: include binning and a different fit where we use mass difference and q^2.

- We used the predicted error from a fit on the fluctuated data to determine an underestimation of the statistical error returned from the fit.

- Misidentification rate: using a combined sample of $D^0 \to K^-\pi^+$ and $D^+ \to K^-\pi^+\pi^+$ we varied the misidentification rate by $\pm 1\sigma$.

- For the ratio $f_+^\pi(0)/f_+^K(0)$ we propagated the error on the yield ratio and we added variations on the fit due to the efficiency as a function of the q^2, $\epsilon(q^2)$. We varied the bin size and the fitting function using a second, a third, and a fourth degree polynomial.

For each set of variations we compute the relative contribution to the systematic error assuming that all the fits are a priori equally likely. Therefore, we find the mean value for the variation is given by:

$$< x >= \sum_i^N x_i/N$$

while the associated error is given by the r.m.s. spread:

$$\sigma_{var} = \sqrt{\frac{\sum_i^N x_i^2 - N < x >^2}{N-1}}.$$

The contribution $\sigma_{f.d.}$ to the systematic error from the fluctuated data study, is computed using the formula:

$$\sigma_{sys} = \sqrt{\sigma^2_{f.d.} - \sigma^2_{stat}}.$$

In Table 7.7 the contributions from the studies performed are reported.

	BR	$\pi\mu\nu$ pole mass	$K\mu\nu$ pole mass	$f_-^K(0)/f_+^K(0)$	$f_+^\pi(0)/f_+^K(0)$
cut variations	0.003	0.052	0.019	0.25	0.017
fit variations	0.004	0.050	0.015	0.19	0.023
misidentification	0.002	~ 0	0.	0	0.011
$\epsilon(q^2)$ fit var.		-	-	-	0.010
fluctuated data	0.005				0.029
TOTAL	0.007	0.072	0.03	0.3	0.043

Table 7.2: Contributions from different sources to the systematic uncertainties. The final error is obtained by adding in quadrature each component in the table.

Using the fit to the two-dimensional $\cos\theta_l$ vs. q^2 distribution we obtain the results:

$$\frac{\Gamma(D^0 \to \pi^-\mu^+\nu)}{\Gamma(D^0 \to K^-\mu^+\nu)} = 0.074 \pm 0.008\ (stat.) \pm 0.007\ (sys.)$$

$$m_\pi = 1.91^{+0.30}_{-0.15}\ (stat.) \pm 0.07\ (sys.)$$

$$m_K = 1.93^{+0.05}_{-0.04}\ (stat.) \pm 0.03\ (sys.)$$

$$\frac{f_-^K(0)}{f_+^K(0)} = -1.7^{+1.5}_{-1.4}\ (stat.) \pm 0.3\ (sys.)$$

$$\frac{f_+^\pi(0)}{f_+^K(0)} = 0.85 \pm 0.04\ (stat.) \pm 0.04\ (sys.) \pm 0.01\ (\mathrm{CKM})$$

In a similar way we compute a fit to the $\pi^-\mu^+\nu$ and $K^-\mu^+\nu$ sample assuming a modified pole model for the q^2 dependence:

$$f_\pm(q^2) = \frac{f_\pm(0)}{[1 - \frac{q^2}{m^2_{pole}}][1 - \frac{\alpha\, q^2}{m^2_{pole}}]}.$$

This form allows a measurement of the contribution of higher order poles to the dominant one. From the fit we find:

$$\alpha_\pi = 0.27^{+0.35}_{-0.47}\ (stat.) \pm 0.15\ (sys.)$$

$$\alpha_K = 0.28 \pm 0.08\ (stat.) \pm 0.05\ (sys.).$$

Chapter 8

q^2 Dependence

In this chapter we present the measurement of the q^2 dependence of the form factor $|f_+(q^2)|^2$ for the high statistics decay $D^0 \to K^-\mu^+\nu$. This analysis consists of combining n independent measurements of $|f_+(q^2)|^2$ where each measurement is an average of the form factor over a given q^2 bin. This part of the analysis has been performed in a more complete way by the University of Illinois group who also investigated different sources of systematic error [34]. We will describe the methodology followed by the Colorado group.

The main issues in this measurement are the subtraction of the background from the $K^-\mu^+\nu$ sample and the data correction for smearing effects which, when the experimental resolution is comparable to the bin size of the distribution of interest (in this case the q^2 distribution), cannot be neglected. While the first two sections focus on these problems, the third section describes how the fit to the form factor distribution, using the most commonly used parametrization (pole dominance), is performed. The chapter concludes with a comparison of the results obtained with these fits to the results obtained from the parametric analysis.

8.1 Deconvolution Technique

As we mentioned above, when the experimental resolution is large compared to the bin size of a distribution we want to measure, the migration of events from the proper generated bin to the adjacent bins cannot be neglected. In the FOCUS experiment, the momentum of the charm particle is inferred from the momentum of the daughters of the decay. Since semileptonic decays have a neutrino in the final state and the neutrino cannot be reconstructed in the spectrometer we can count only on kinematic constraints to reconstruct the q^2 of a given event. As we already discussed in chapter 4, this is accomplished by implementing the so called D^{*+}-cone closure (see Appendix B for a complete description of this technique). Even though this constraint greatly improves our q^2 resolution[1] , we still end up with a resolution more than one order of magnitude worse than that for a fully reconstructed decay.

To address this problem we applied a technique that aims to deconvolve the experimental resolution through a deconvolution matrix based on Monte Carlo simulation. An important assumption is that our Monte Carlo well simulates the experimental smearing observed in the data. For this purpose, studies within the FOCUS collaboration have been performed using the high statistics mode $D^0 \to K^-\pi^+\pi^-\pi^+$ in which one of the charged pions is blanked and treated as a neutrino. The q^2 obtained by using the D^{*+}-cone closure is compared to the fully reconstructed q^2. Besides providing an idea of our resolution, these studies have been performed on data and Monte Carlo and show good agreement between the two. The results are shown in Fig. 8.1 and yield a resolution in q^2 of the order of 150 (MeV/c^2)^2.

The goal is to give n independent measurements of the form factor $|f_+(q^2)|^2$. In order to proceed we refer again to Eq. 1.6, which, when integrated over the lepton energy, becomes:

[1] Studies performed on high statistics modes show that this technique outperform the standard neutrino closure resulting in a two-fold ambiguity.

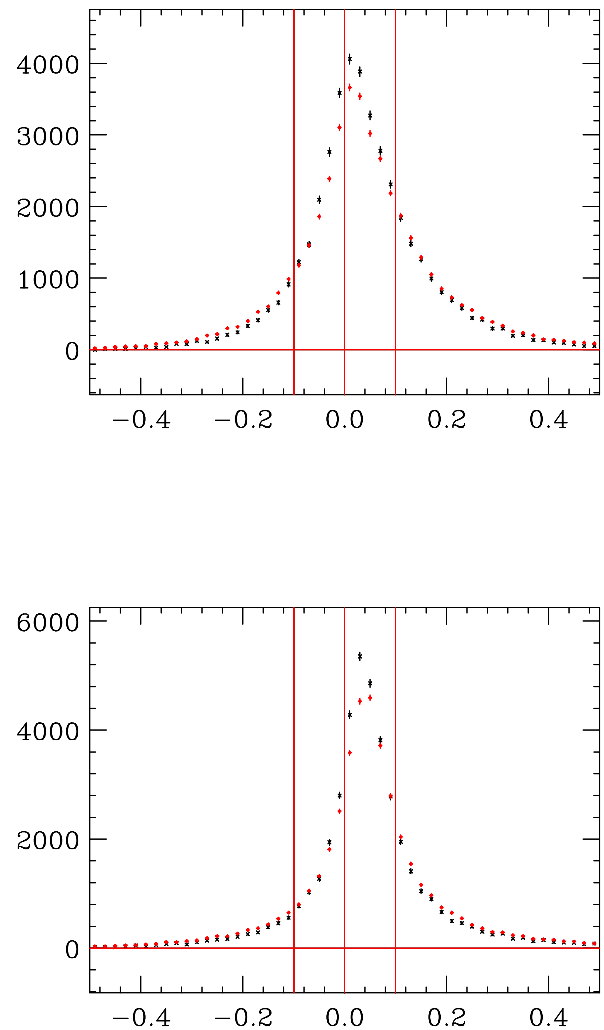

Figure 8.1: Blanking studies using $D^0 \to K^-\pi^+\pi^+\pi^+$. In the top plot a comparison of the q^2 resolution between data (black) and Monte Carlo (red) is shown for the standard neutrino closure. At the bottom the same comparison when we apply the D^{*+} cone closure technique. This study has been performed using the decay $D^0 \to K^-\pi^+\pi^+\pi^+$.

$$\frac{d\Gamma}{dq^2} = \frac{G_F^2}{8\pi^3\ m_D}\left|V_{cs}\right|^2 \left|f_+(q^2)\right|^2 P_K \left(\frac{W_0 - E_K}{F_0}\right)^2 \left[\frac{1}{3}m_D P_K^2 + \frac{m_\mu^2}{8m_D}(m_D^2 + m_K^2 + 2m_D E_K) \right.$$
$$\left. + \frac{1}{3}m_\mu^2 \frac{P_K^2}{F_0} + \frac{1}{4}m_\mu^2 \frac{m_D^2 - m_K^2}{m_D} Re\left(\frac{f_-(q^2)}{f_+(q^2)}\right) + \frac{1}{4}m_\mu^2 F_0 \left|\frac{f_-(q^2)}{f_+(q^2)}\right|^2\right] \tag{8.1}$$

where:

$$W_0 = \frac{m_D^2 + m_K^2 - m_\mu^2}{2m_D}$$
$$F_0 = \frac{W_0 - E_K + m_\mu^2}{2m_D}$$

Equation 8.1 shows that in the assumption that the two form factors $f_-(q^2)$ and $f_+(q^2)$ have the same (or at least very similar) q^2 dependence [2] , the term in squared parentheses is independent of the q^2 dependence of the form factors, and the differential decay rate is proportional to $|f_+(q^2)|^2$. In the following discussion we therefore assume:

$$\xi \equiv \frac{f_-^K(0)}{f_+^\pi(0)} \sim \text{constant}$$

Let's now assume we want to measure the form factor average $< f_+(q^2) >$ over three q^2 bins[3] . We start by generating a high statistics dedicated Monte Carlo sample[4] in which, for each event, we save the generated as well as the reconstructed q^2 values in a two dimensional matrix $M_{i\alpha}$ (the Roman index refers to the reconstructed bin and the Greek index refers to the generated bin). This matrix is constructed using events generated within the spectrometer acceptance and that survive the selection criteria and the trigger requirements.

The number of Monte Carlo events $N(q_i^2)$ reconstructed in the i-th q^2 bin is found by summing over all the events generated in bin α=1,2,3, but that are reconstructed in bin i:

$$N(q_i^2) = \sum_{\alpha=1}^{3} M_{i\alpha}. \tag{8.2}$$

[2] To the best of our knowledge there no reason to think that this assumption is incorrect.
[3] The actual measurement will be performed over 5 bins of q^2 but it's easier to use three bins to describe the method.
[4] By "dedicated" Monte Carlo we refer to the fact that in each generated event, the decay $D^0 \to K^-\mu^+\nu$ is produced in at least one of the two "legs", charm or charmbar.

Since the Monte Carlo has been generated assuming a certain model for the form factor, namely the pole dominance form, we must generalize Eq. 8.2 for a generic form factor $\tilde{f}_+^2(q^2)$ describing the data distribution. This is accomplished by weighting each matrix element $M_{i\alpha}$ for the number of events that the new form factor would have generated in each α bin. This is expressed by the following relation:

$$\begin{pmatrix} N(q_1^2) \\ N(q_2^2) \\ N(q_3^2) \end{pmatrix} = R \begin{pmatrix} M_{11} & M_{12} & M_{13} \\ M_{21} & M_{22} & M_{23} \\ M_{31} & M_{32} & M_{33} \end{pmatrix} \begin{pmatrix} |\tilde{f}_+(q_1^2)|^2/|f_+(q_1^2)|^2 \\ |\tilde{f}_+(q_2^2)|^2/|f_+(q_2^2)|^2 \\ |\tilde{f}_+(q_3^2)|^2/|f_+(q_3^2)|^2 \end{pmatrix} \tag{8.3}$$

where the multiplicative factor R is just a normalization factor that accounts for the difference in the Monte Carlo and data yields and the term $|\tilde{f}_+(q_i^2)|^2/|f_+(q_i^2)|^2$ is the weight.

We can implement Eq. 8.3 on data, where the form factor $|\tilde{f}_+(q^2)|^2$ describes the unknown decay mechanism that we want to measure and $N(q_i^2)$ is the observed number of signal events in the $K^-\mu^+\nu$ data sample. The form factor $|f_+(q^2)|^2$ used in the generation can be effectively included in the resolution matrix M. Inverting Eq. 8.3 we find a set of equations that, for each q^2 bin, allow us to compute independent measurements of the form factor $|\tilde{f}_+(q^2)|^2$ through the use of the inverse matrix M^{-1} and the measured q^2 distribution in data given by $N(q_i^2)$:[5]

$$\begin{pmatrix} |\tilde{f}_+(q_1^2)|^2 \\ |\tilde{f}_+(q_2^2)|^2 \\ |\tilde{f}_+(q_3^2)|^2 \end{pmatrix} = \frac{1}{R} \begin{pmatrix} M_{11}/|f_+(q_1^2)|^2 & M_{12}/|f_+(q_1^2)|^2 & M_{13}/|f_+(q_1^2)|^2 \\ M_{21}/|f_+(q_2^2)|^2 & M_{22}/|f_+(q_2^2)|^2 & M_{23}/|f_+(q_2^2)|^2 \\ M_{31}/|f_+(q_3^2)|^2 & M_{32}/|f_+(q_3^2)|^2 & M_{33}/|f_+(q_3^2)|^2 \end{pmatrix}^{-1} \begin{pmatrix} N(q_1^2) \\ N(q_2^2) \\ N(q_3^2) \end{pmatrix} \tag{8.4}$$

[5] By construction, the deconvolution matrix accounts for reconstruction efficiency acceptance and the kinematic term P_K^3 with P_K being the momentum of the kaon in the D^0 center of mass.

In Eq. 8.4 the inverse matrix M^{-1} is called the **deconvolution matrix**. In Fig. 8.2 we show the resolution and the deconvolution matrix obtained by the method described above. The off-diagonal elements of the resolution matrix show the smearing effects in the q^2 distribution. With a binning of the order of 300 (MeV/c^2)^2 we still have a large migration of events from the generated bin to the other bins.

Also the deconvolution matrix has interesting features. First, the monotonic increase in the yields of the diagonal terms reflects the fact that the decay rate is proportional to P_K^3 term which approaches zero at maximum q^2. The other characteristic of this matrix is given by an alternating sign when moving along each row. This is caused by the fact that when we measure the number of generated events in a given q^2 bin, we have to subtract the contribution from events that, from adjacent bins, migrated into the bin of interest.

8.2 Background Subtraction

In the previous section we demonstrated how it's possible to extract information about the form factor $f_+(q^2)$ for a pseudoscalar semileptonic decay. From the practical point of view, in order to find the vector $N(q_i^2)$ of the number of $K^-\mu^+\nu$ events, one needs to subtract the backgrounds from the total sample.

This can be accomplished in different ways. One way is to perform a weighting, similar to the one described before, on both the total sample as well as on the background where the weights on the data have a positive sign while the weights on the background have a negative sign. This technique effectively resolves the background subtraction.

We followed a different path by taking advantage of the fitting technique used in the parametric analysis described in Chapter 6 which already returns the background components in the q^2 projection. The contributions found in the fit, namely the combinatoric background and the $K^*(892)^-\mu^+\nu$ components, are subtracted from the total sample leaving only the q^2 distribution for signal events of $D^0 \to K^-\mu^+\nu$.

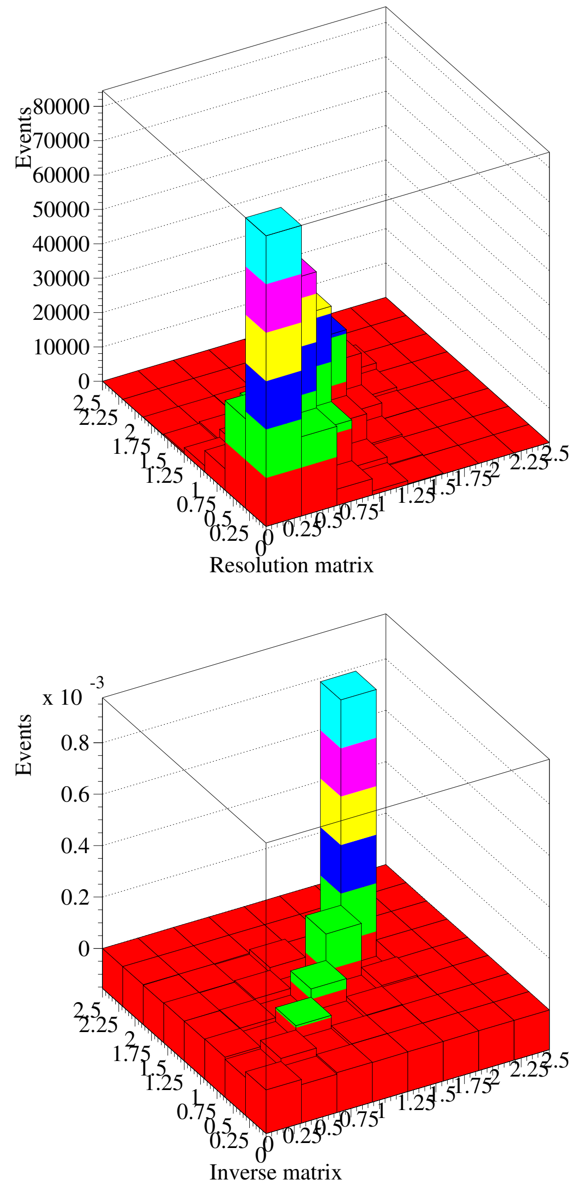

Figure 8.2: (top) Resolution matrix: the non-diagonal terms show the importance of resolution effects in the analysis. We need to account for the fact that in many cases the event is reconstructed in a q^2 bin different from the one where it was generated; (bottom) deconvolution matrix obtained by inversion of the resolution matrix.

Since the $K^-\mu^+\nu$ sample is much cleaner than the $\pi^-\mu^+\nu$ sample we didn't need very tight cuts. Therefore, we performed the fit to the $D^{*+} - D^0$ mass difference and q^2 distributions (rather that the fit on q^2 and $\cos\theta_l$) in such a way to avoid the tight cut

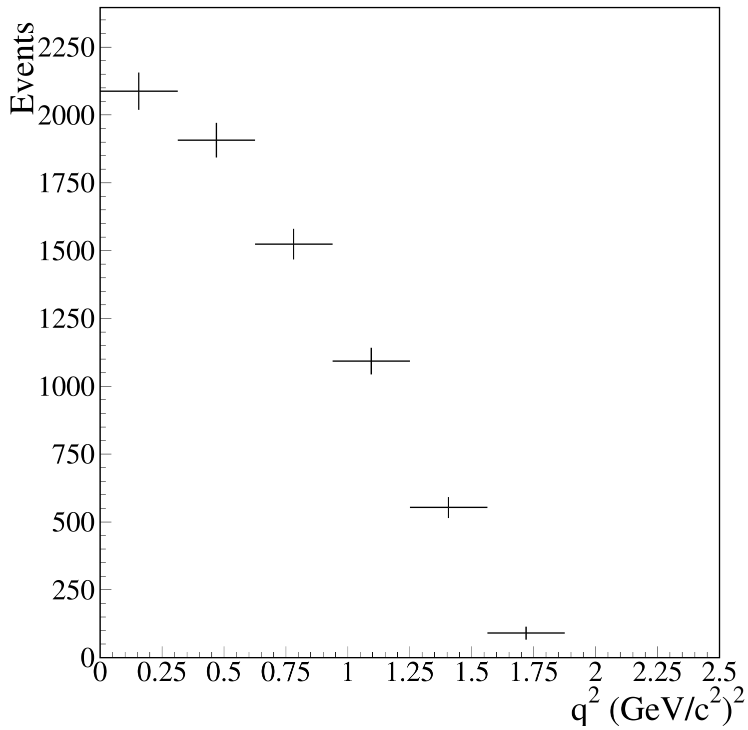

Figure 8.3: Background subtracted q^2 distribution for $D^0 \to K^-\mu^+\nu$. The distribution is obtained by performing a fit to the two dimensional distribution q^2 vs. $D^{*+} - D^0$ mass difference and subtracting the background components from the total sample.

on the mass difference signal region. In this way we were able to gain in statistics. In Fig. 8.3 the background subtracted distribution for the $D^0 \to K^-\mu^+\nu$ decay is shown. After applying the procedure described above we obtain the distribution in Fig. 8.4 for the q^2 dependence of the $D^0 \to K^-\mu^+\nu$ form factor squared $|f_+(q^2)|^2$ where the overflow bin has been dropped because of the higher background from $D^0 \to K^*(892)^-\mu^+\nu$.

8.3 Fit to the q^2 Distribution

We fit the q^2 distribution to the pole dominance form and compare these results to the results obtained in the parametric analysis. The issue is to properly account for the correlation between the different bins. This is accomplished by implementing the full correlation matrix in the computation of the χ^2. The correlation matrix is defined

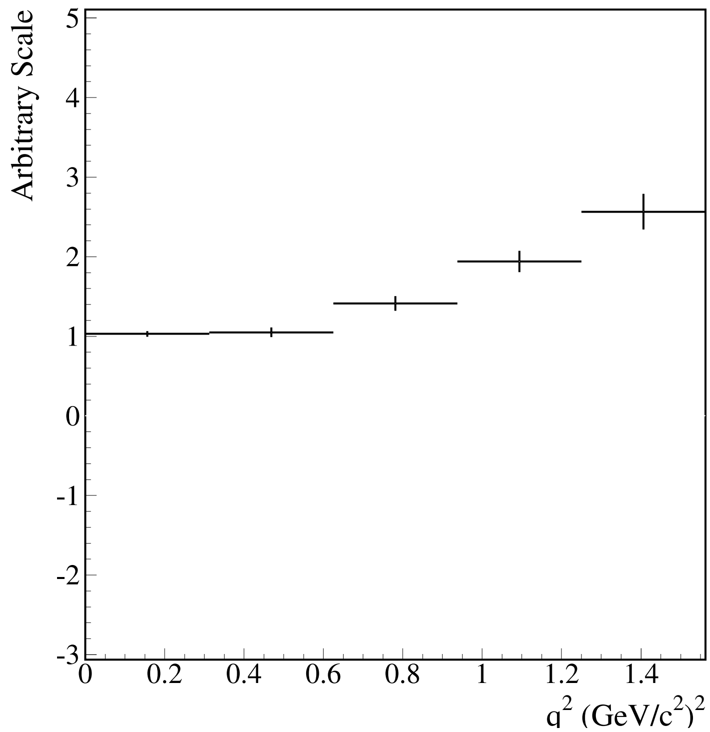

Figure 8.4: $D^0 \rightarrow K^-\mu^+\nu$ q^2 dependence.

as:

$$C_{\alpha\beta} = \left\langle \delta|f_+^\alpha|^2 \times \delta|f_+^\beta|^2 \right\rangle .$$

The error $\delta|f_+^\alpha|^2$ is given by the weighted sum over the measured bins:

$$\delta|f_+^\alpha|^2 = \sum_\alpha D_{i\alpha}\delta n_i.$$

where δ_i represents the error on the measured i-th bin and where we re-wrote the deconvolution matrix $M_{i\alpha}^{-1}$ as $D_{i\alpha}$. Again, the Greek index refers to the generated q^2 bin while the Roman index refers to reconstructed q^2 bins. The $\alpha\beta$ element of the correlation matrix can be written as:

$$C_{\alpha\beta} = \sum_\alpha \sum_j D_{i\alpha} < \delta n_i \delta n_j > D_{j\beta}. \tag{8.5}$$

If we assume Poisson distribution fluctuations over the measured bins, then they must satisfy the relation $< \delta n_\alpha \delta n_\beta >= n_\alpha \delta_{\alpha\beta}$, which replaced in equation 8.6 gives:

$$C_{\alpha\beta} = \sum_{events} D_{i\alpha} D_{i\beta}. \tag{8.6}$$

If we now define the vector of the expected form factor values as $\vec{f^*}$ and the vector of the measured form factor values as $\vec{f}$ we can construct the χ^2:

$$\chi^2 = (\vec{f^*} - \vec{f}(m))^T C^{-1} (\vec{f^*} - \vec{f}(m)) \tag{8.7}$$

where m is the fit parameter. As we previously mentioned, incorporating the covariance matrix plays a critical role given the strong correlation between adjacent bins. Using the uncorrelated form would return a much bigger error than what we get using Eq. 8.7. To obtain an idea of the correlation between adjacent bins we can construct the correlation matrix :

$$\rho_{\alpha\beta} = \frac{\left\langle \delta|f_+^\alpha|^2 \times \delta|f_+^\beta|^2 \right\rangle}{\sqrt{\left\langle \delta|f_+^\alpha|^2 \times \delta|f_+^\alpha|^2 \right\rangle \left\langle \delta|f_+^\beta|^2 \times \delta|f_+^\beta|^2 \right\rangle}}$$

which returns correlations up to 60%.

In the fit, the free parameter is the pole mass, while the overall normalization is fixed. The fit is shown in Fig. 8.5 and it returns the pole mass:

$$M_{pole}^K = 1.92 \pm 0.03\ (stat.)$$

in excellent agreement with the result obtained in Chapter 6:

$$M_{pole}^K = 1.93^{+0.05}_{-0.04}\ (stat.) \pm 0.03\ (sys.).$$

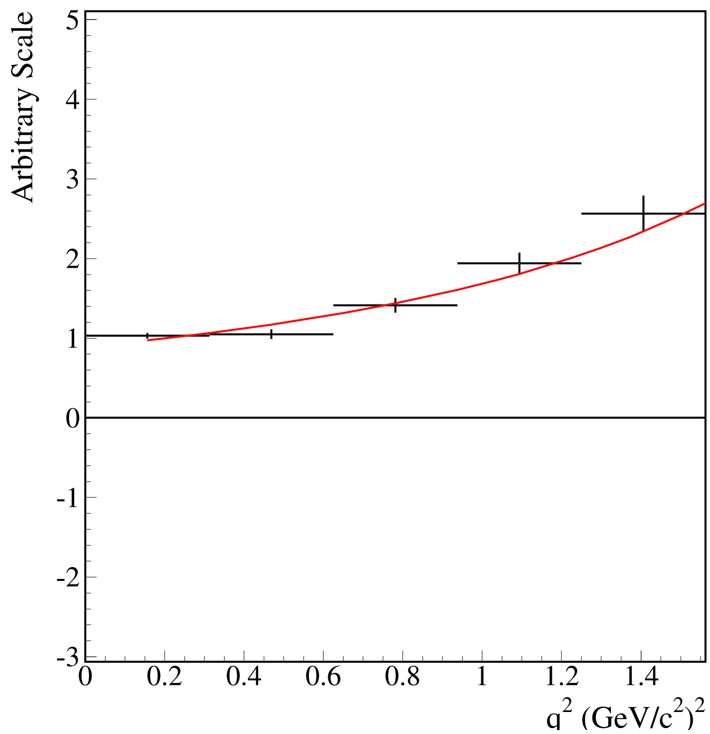

Figure 8.5: Fit to $|f_+(q^2)|^2$ using a pole mass dependent functional form. The fit returns a pole mass which is in very good agreement with the result obtained from the parametric analysis.

Chapter 9

Summary and Conclusions

9.1 Summary

The study of semileptonic decays has always been important due to the simplifications that can be made in the theoretical description compared to hadronic decays. Thanks to the small q^2 compared to the W^+ mass, the Hamiltonian of these decays can be assumed to be the product of two independent currents: the leptonic current which is theoretically well understood and is described by the V-A interaction, and the hadronic current which contains the QCD contribution to the decay. In pseudoscalar semileptonic decays the hadronic current can be described by two form factors f_+ and f_- which are each only a function of the lepton-neutrino invariant mass, called q^2. In the assumption that the q^2 dependence is the same for the two form factors, the differential decay amplitude can be written to be proportional to $|f_+(q^2)|^2$ (see Eq. 1.6). Furthermore, each contribution to the decay rate from the form factor f_- is strongly suppressed by a factor proportional to the lepton mass squared.

We have performed an exhaustive analysis of the pseudoscalar semileptonic decays, $D^0 \to \pi^-\mu^+\nu$ and $D^0 \to K^-\mu^+\nu$. Namely, we made a measurement of the relative branching ratio $\Gamma(\pi^-\mu^+\nu)/\Gamma(K^-\mu^+\nu)$ and of the form factor ratio $f_+^\pi(0)/f_+^K(0)$. Assuming a pole dominance and a modified pole dependence of the form factors, we further measured the pole masses and the parameter α which measures the contribution of higher poles to the decay width for the two decays (see Eq. 1.12).

Given the experiment's high efficiency at reconstructing muons, FOCUS is one of the few experiments that can extract information about the form factor f_-. We report a new measurement of the form factor ratio $f_-^K(0)/f_+^K(0)$ for the decay mode $D^0 \rightarrow K^-\mu^+\nu$. The final part of this analysis is dedicated to a model independent measurement of the q^2 dependence of the form factor for decay $D^0 \rightarrow K^-\mu^+\nu$.

From the experimental point of view the analyses of semileptonic decays are challenging, since the neutrino from the decay is not reconstructed in the spectrometer. This lack of information on the decay has two main experimental consequences: first, it is impossible to use the reconstructed D^0 momentum vector to find the primary vertex of the decay and second, there is no peaking signal corresponding to the D^0 mass that we can reconstruct. The visible mass, which is defined as the hadron-lepton invariant mass, is spread over a large fraction of the mass spectrum and does not show any striking difference from the background distributions. In this analysis, the interpretation of the invariant mass distribution, is even more complicated by the fact that the Cabibbo suppression in the $D^0 \rightarrow \pi^-\mu^+\nu$ decay, results in a final sample in which the signal and the backgrounds from Cabibbo allowed decays (especially $D^0 \rightarrow K^-\mu^+\nu$) have comparable statistics.

The most important tool to overcome these problems is to use a sample in which the D^0 candidate comes from the decay of a D^{*+} particle. We use pions from the D^0 production vertex and we construct the $D^{*+} - D^0$ mass difference which allows us to better discriminate between the signal and the combinatoric background. Additional techniques can be implemented to improve our ability to reject backgrounds and to better determine the neutrino momentum. We implemented two kinds of kinematic constraints: the first is the traditional neutrino closure (see Appendix A) which returns two possible solutions for the D^0 (or the neutrino) momentum, the other is the D^{*+} cone closure (Appendix B) which takes advantage of the D^{*+}-tag and returns the best hypothesis for the q^2 of each candidate event.

In the fit to the data we use information from three variables, the $D^{*+} - D^0$ mass difference just discussed, q^2, and $\cos\theta_l$ (where θ_l is defined as the angle between the neutrino and the D^0 direction in the lepton-neutrino center of mass frame). The parameters of the fit are the yields for signal and backgrounds, the pole masses and the form factor ratio $f_-^K(0)/f_+^K(0)$. We implement a weighting technique based on the decay intensity for each event to fit for these parameters. Since the efficiency has a non-trivial q^2 dependence, the fit is designed in such a way that for each choice of the pole masses or $f_-^K(0)/f_+^K(0)$ the efficiency is recomputed and used in the next fit iteration.

By using the $\pi^-\mu^+\nu$ and $K^-\mu^+\nu$ fit yields, we can extract the form factor ratio $f_+^\pi(0)/f_+^K(0)$ by computing a numerical integration of the decay intensity modulated by a function that describes the reconstruction efficiency as a function of the q^2.

Even if the kinematic constraints greatly improve the ability to separate signal and backgrounds, the missing neutrino has important consequences on the experimental resolution. This represents the most important issue in the non-parametric analysis of the q^2 dependence. We must account for the fact that the migration of events from the generated q^2 bin to another bin is significant. We implement a method to deconvolve the experimental resolution by using a Monte Carlo that for each event saves the generated and the reconstructed q^2 values, and describes migrations between bins by a matrix. After a proper normalization we can invert this matrix and extract five independent measurements of the form factor, $f_+^K(q^2)$, where each measurement is an average of the form factor value over a given q^2 bin.

Once the deconvolution has been applied we proceed to a fit of these independent measurements of $f_+^K(q^2)$ using the same models implemented in the parametric analysis. Because of the strong correlation between the q^2 bins, we must build a full correlation matrix which is then used to construct the χ^2 function to be minimized. Aside from the obvious importance of the non-parametric form factor measurement, the fits represent an additional cross check on the results obtained in the parametric analysis.

9.2 Conclusions

So far we have described the measurements reported in this thesis and the techniques implemented to obtain them, but one fundamental question is yet to be answered: why are are these results important and what do they add to our understanding of physics?

To answer this important question it should be realized that a large fraction of the research effort in particle physics today, from both the theoretical and experimental points of view, is dedicated to the understanding of the CKM matrix and its implication on the Standard Model picture. In the Standard Model, this matrix is unitary, and a precise measurement of the matrix elements can probe the existence of new physics. Each row of the matrix corresponds to a unitarity triangle. One way to test the CKM unitarity is to combine redundant measurements of these triangles by measuring both angles and sides.

While exclusive semileptonic decays have always been an excellent tool to measure the sides of these triangles, unfortunately they require a reliable parametrization of the form factors. The best example is given by the matrix element V_{ub} where theoretical uncertainties are about 10%, well above the desired uncertainty of 5% needed to put a significant constraint on one side of the unitary triangle [38]. The b-factories have a good opportunity to measure this parameter, but the present theoretical uncertainties on the form factors represent a limit on the experimental sensitivity. In Fig. 9.1, the status of the unitary triangle as reported in reference [39] is shown.

Experimental information about the pseudoscalar form factors in the charm sector are of great interest because the matrix elements V_{cs} and V_{cd} are well known. This allows for the matrix element uncertainty to be removed when determining the form factors. A direct comparison of the form factor results between the various theoretical approaches (like Lattice QCD, quark models, and QCD sum rules) and the experiments, provide

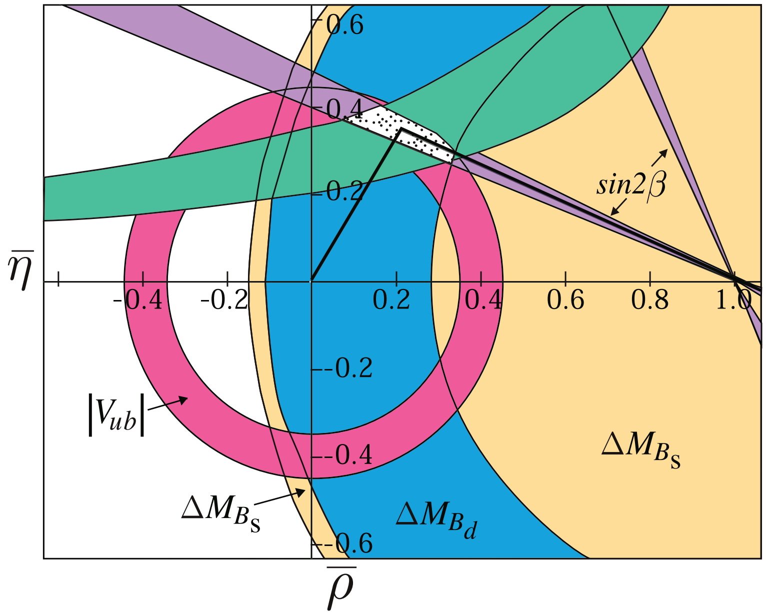

Figure 9.1: Status of the unitary triangle

an important check on the theory and a calibration tool of these different approaches. Once a reliable approach is found and its systematic uncertainties are under control, the same framework can be applied to the determination of the form factors in the b sector allowing us to reduce the uncertainty on V_{ub}. Furthermore, the measurement of the branching ratio $\Gamma(D^0 \to \pi^-\mu^+\nu)/\Gamma(D^0 \to K^-\mu^+\nu)$ provides an important engineering number which can be used in determining the level of charm backgrounds in bottom quark decays (since bottom particles decay to charm particles most of the time).

A comparison of experimental results for semimuonic and semielectronic modes for both the branching ratio $\Gamma(D^0 \to \pi^-\mu^+\nu)/\Gamma(D^0 \to K^-\mu^+\nu)$ and the form factor ratio $f_+^\pi(0)/f_+^K(0)$ is shown in Table 9.1. Our branching ratio measurement of $0.074 \pm 0.008 \pm 0.007$ is in good agreement with the most recent measurements but it should be noticed that the recent values are about 25% lower than the PDG average of 0.101 ± 0.017 (in the electron mode) [39]. Further, the form factor ratio $f_+^\pi(0)/f_+^K(0)$ also seems to be lower than what was measured by older experiments [42, 35, 37]. The newer experiments are in better agreement with the theoretical predictions reported in Table 9.3.

Experiments	$\Gamma(\pi^-\mu^+\nu)/\Gamma(K^-\mu^+\nu)$	$\Gamma(\pi^-e^+\nu)/\Gamma(K^-e^+\nu)$	$f_+^\pi(0)/f_+^K(0)$
This work	$0.074 \pm 0.008 \pm 0.007$		$0.85 \pm 0.04 \pm 0.04 \pm 0.01$
CLEO-c [40]		$0.070 \pm 0.007 \pm 0.003$	
CLEO [41]		$0.082 \pm 0.006 \pm 0.005$	$0.86 \pm 0.07^{+0.06}_{-0.04} \pm 0.01$
E687 [42]	$0.101 \pm 0.020 \pm 0.003$		$1.00 \pm 0.11 \pm 0.02$
CLEO [35]		$0.103 \pm 0.39 \pm 0.013$	$1.01 \pm 0.20 \pm 0.07$
MARK III [36]	$0.110^{+0.07}_{-0.04} \pm 0.02$		
CLEO [37]		$0.170 \pm 0.054 \pm 0.028$	$1.29 \pm 0.21 \pm 0.11$

Table 9.1: List of experimental results for the branching ratio and the form factor ratio $f_+^\pi(0)/f_+^K(0)$. The FOCUS results have the smallest uncertainties in the semimuonic sector.

Experiments	M^π_{pole}	M^K_{pole}	$f_-^K(0)/f_+^K(0)$
This work	$1.91^{+0.30}_{-0.15} \pm 0.07$	$1.930^{+0.05}_{-0.04} \pm 0.03$	$-1.7^{+1.5}_{-1.4} \pm 0.30$
CLEO [41]	$1.86^{+0.10}_{-0.06} \pm 0.05$	$1.89 \pm 0.05^{+0.04}_{-0.03}$	
E687 [29]		$1.87^{+0.11}_{-0.08} \pm 0.06$	$-1.3^{+3.6}_{-3.4} \pm 0.6$

Table 9.2: List of experimental results for the pole masses and the form factor ratio $f_-^K(0)/f_+^K(0)$.

In the same way, we compare the results for the q^2 dependence in Table 9.2. Again we find that FOCUS results for the pole masses are in agreement, but have smaller uncertainty, with previous measurements. The most interesting result is given by the $K^-\mu^+\nu$ pole mass which is significantly lower than the value predicted by the naive pole dominance dependence. Even though the uncertainty on the $\pi^-\mu^+\nu$ pole mass is large, M^π_{pole} seems to show the same trend as the $K^-\mu^+\nu$ pole mass. We also report the best measurement on the contribution of the form factor ratio $f_-^K(0)/f_+^K(0)$ to the $D^0 \to K^-\mu^+\nu$ decay rate. As the $f_-^K(0)$ term only appears multiplied by the lepton mass squared, it can only be studied in the semimuonic channels.

These results are interesting and can impact other measurements such the study of semileptonic vector decays which rely on a pole dominance parametrization of the axial-vector and vector form factors. An analysis of the q^2 dependence of the vector modes could lead to a better understanding of the discrepancy between the theoretical models and the experimental results.

In Table 9.3 we show theoretical predictions of the branching ratio $\Gamma(D^0 \rightarrow \pi^-\mu^+\nu)/\Gamma(D^0 \rightarrow K^-\mu^+\nu)$, the ratio $f_-^K(0)/f_+^K(0)$, and the ratio $f_+^\pi(0)/f_+^K(0)$. It's worthwhile noticing how well the results reported in this thesis agree with the most recent theoretical calculation obtained by an unquenched lattice QCD calculation [43, 44].

In the near future, at least from the experimental point of view, significant improvements in the measurements of semileptonic decays in the charm and bottom sector will be made. The CLEO-c experiment is currently acquiring a clean sample of $D^0 \rightarrow \pi^- e^+\nu$ and $D^0 \rightarrow K^- e^+\nu$ decays which, combined with excellent q^2 resolution, should allow us to improve several models. The B-factories (BABAR, BELLE, and possibly CDF) can also provide big improvements on these parameters. In particular they could improve our measurement of the term $f_-^K(0)/f_+^K(0)$. This ratio is suppressed by the lepton mass squared and therefore cannot be investigated in the electron sector. These improvements will lead to improvements in the determination of CKM matrix elements and will aid in our quest to find physics beyond the Standard Model.

Theory	$\Gamma(\pi^-\mu^+\nu)/\Gamma(K^-\mu^+\nu)$	$f_-^K(0)/f_+^K(0)$	$f_+^\pi(0)/f_+^K(0)$
Aubin *et al.* [44]	$0.084 \pm 0.007 \pm 0.017 \pm 0.009$		$0.86 \pm 0.05 \pm 0.11$
Okamoto *et al.* [43]			0.85 ± 0.05
Melikhov *et al.* [45]	0.098		0.88
Amoros *et al.* [11]		~ -0.72	~ 1.05
LCR [10]			0.83
Abada *et al.* [9]			0.86
Scora *et al.* [46]	0.048		
Lubicz *et al.* [47]	0.086 ± 0.041		0.92 ± 0.18
Narison [48]	0.083		0.91 ± 0.01
Demchuk *et al.* [49]	0.073		0.87

Table 9.3: List of theory results.

Bibliography

[1] L. Wolfenstein, Phys. Rev. Lett. **51**, 1945 (1983).

[2] S. L. Glashow, J. Iliopoulos and L. Maiani, Phys. Rev. D **2**, 1285 (1970).

[3] J. D. Richman and P. R. Burchat, Rev. Mod. Phys. **67**, 893 (1995).

[4] E. Fermi, Nuovo Cim. **11**, 1 (1934).

[5] C. S. Wu, E. Ambler, R. W. Hayward, D. D. Hoppes and R. P. Hudson, Phys. Rev. **105**, 1413 (1957).

[6] D. J. Griffiths, "Introduction To Elementary Particles.", New York, USA: WILEY, 392p (1987).

[7] L. Jauneau, "Spectra and Polarization in $K_{\mu 3}$", Methods in Subnuclear Physics, Edited by M. Nikolic, Vol.3, 123 (1969).

[8] D. Becirevic and A. B. Kaidalov, Phys. Lett. B **478**, 417 (2000).

[9] A. Abada, D. Becirevic, P. Boucaud, J. P. Leroy, V. Lubicz and F. Mescia, Nucl. Phys. B **619**, 565 (2001).

[10] A. Khodjamirian, R. Ruckl, S. Weinzierl, C. W. Winhart and O. I. Yakovlev, Phys. Rev. D **62**, 114002 (2000).

[11] G. Amoros, S. Noguera and J. Portoles, Eur. Phys. J. C **27**, 243 (2003).

[12] J. Wiss, "Charm at Fixed Target", Lectures at Varenna Summer School (1997).

[13] G. Alimonti *et al.*, Nucl. Instrum. Meth. A **314**, 411 (1992).

[14] P. L. Frabetti *et al.* [E-687 Collaboration], Nucl. Instrum. Meth. A **320**, 519 (1992).

[15] J. M. Link *et al.* [FOCUS Collaboration], Nucl. Instrum. Meth. A **516**, 364 (2004).

[16] J. M. Link *et al.* [FOCUS Collaboration], Nucl. Instrum. Meth. A **484**, 270 (2002).

[17] L. Cinquini *et al.*, "A Description of the Inner Electromagnetic Calorimeter for FOCUS", Internal Memo.

[18] S. Bianco *et al.*, arXiv:hep-ex/9912066.

[19] V. Arena *et al.* [Focus Collaboration], Nucl. Instrum. Meth. A **434**, 271 (1999).

[20] C. Cawlfield, "Studies of the Semileptonic Decays of D Mesons," Ph.D. thesis, University of Illinois at Urbana-Champaign, (2001).

[21] J. Wiss, private communication and http://www.hep.uiuc.edu/e687/muon/muon.html.

[22] P. D. Sheldon [Focus Collaboration], *Prepared for 3rd International Workshop on Resistive Plate Chambers and Related Detectors (RPC 95), Pavia, Italy, 11-12 Oct 1995*

[23] A. Kreymer and F. Prelz [Focus Collaboration], http://www-focus.fnal.gov/papers/daq_main/daq_main/daq_main.html

[24] R.L. Culbertson, "Four-Body Semileptonic Decays of D Mesons", Ph.D. thesis, University of Illinois at Urbana-Champaign, (1993).

[25] J. M. Link *et al.* [FOCUS Collaboration], Nucl. Instrum. Meth. A **484**, 174 (2002)

[26] E. Vaandering, "Mass and Width Measurements of the Σ_c Baryons," Ph.D. thesis, University of Colorado at Boulder, (2000).

[27] J. Wiss [Focus Collaboration], "Thoughts for muon identification algorithms for E831," http://web.hep.uiuc.edu/e687/muon/mu_id_thoughts.ps.

[28] G. Bonomi, "An iron/scintillator tile calorimeter for the FOCUS experiment at Fermilab", *Given at 7th International Conference on Calorimetry in High-Energy Physics (ICCHEP 97), Tucson, AZ, 9-14 Nov 1997*

[29] W. E. Johns, "Measurements of the semileptonic decay of the neutral charmed meson D0 → K- mu+ muon-neutrino", FERMILAB-THESIS-1995-05

[30] J. M. Link *et al.* [FOCUS Collaboration], Phys. Lett. B **535**, 43 (2002).

[31] J. M. Link *et al.* [FOCUS Collaboration], Phys. Lett. B **544**, 89 (2002).

[32] J. M. Link *et al.* [FOCUS Collaboration], Phys. Lett. B **598**, 33 (2004).

[33] W. Johns, " D^{**} fitting tests", Internal memo, (2003).

[34] J. Wiss, "Deconvolving the D to Kmunu form factors", Internal memo, (2004).

[35] F. Butler *et al.* [Cleo Collaboration], Phys. Rev. D **52**, 2656 (1995).

[36] J. Adler *et al.* [MARK-III Collaboration], Phys. Rev. Lett. **62**, 1821 (1989).

[37] M. S. Alam *et al.* [CLEO Collaboration], Phys. Rev. Lett. **71**, 1311 (1993).

[38] Z. Ligeti, eConf **C030603**, JEU10 (2003) [arXiv:hep-ph/0309219].

[39] S. Eidelman *et al.* [Particle Data Group], Phys. Lett. B **592**, 1 (2004).

[40] K. Y. Gao [CLEO Collaboration], arXiv:hep-ex/0408077.

[41] G. S. Huang *et al.* [CLEO Collaboration], arXiv:hep-ex/0407035.

[42] P. L. Frabetti *et al.* [E687 Collaboration], Phys. Lett. B **382**, 312 (1996).

[43] M. Okamoto *et al.*, Nucl. Phys. Proc. Suppl. **129**, 334 (2004).

[44] C. Aubin *et al.* [Fermilab Lattice Collaboration], arXiv:hep-ph/0408306.

[45] D. Melikhov and B. Stech, Phys. Rev. D **62**, 014006 (2000).

[46] D. Scora and N. Isgur, Phys. Rev. D **52**, 2783 (1995).

[47] V. Lubicz, G. Martinelli, M. S. McCarthy and C. T. Sachrajda, Phys. Lett. B **274**, 415 (1992).

[48] S. Narison, Phys. Lett. B **337**, 163 (1994).

[49] N. B. Demchuk, I. L. Grach, I. M. Narodetski and S. Simula, Phys. Atom. Nucl. **59**, 2152 (1996).

Appendix A

Neutrino Closure

Let's examine a D^0 decay to $K^-\mu^+\nu_\mu$, we can write the 4-momentum for the D^0 as:

$$P_D = P_K + P_\mu + P_\nu = P_c + P_\nu$$

where P_c is the charged system 4-momentum. Then:

$$m_\nu^2 = P_\nu^2 = (P_D - P_c)^2 = m_D^2 + m_c^2 + 2|p_D|\hat{p}_D\vec{p}_c - 2E_DE_c$$

and setting $M^2 = m_D^2 + m_c^2 - m_\nu^2$:

$$2E_DE_c = M^2 + 2|p_D|\hat{p}_D\vec{p}_c$$

and extracting the energy E_D of the D^0

$$E_D = \frac{1}{2E_c}(M^2 + 2|p_D|\hat{p}_D\vec{p}_c).$$

Squaring both sides and writing $E_D^2 = m_D^2 + p_D^2$ we can reduce everything to the equation:

$$\frac{[(\hat{P}_D\vec{P}_c)^2 - 1]}{E_c^2}|p_D|^2 + \frac{M^2}{E_c^2}(\hat{p}_D\vec{p}_c)|p_D| + \frac{M^4 - m_D^2}{4E_c^2} = 0.$$

We can now choose a reference frame where $\hat{P}_D\vec{P}_c = 0$ so that the previous equation becomes:

$$\frac{1}{(E_c^*)^2}\ |p_D^*|^2 - \frac{M^4 - m_D^2}{4(E_c^*)^2} = 0$$

from which we can derive the two solutions for p_D^*.

Appendix B

D^{*+} cone closure

The D^{*+} cone closure takes advantage of the fact that the reconstructed semileptonic decay comes from a D^{*+} decay to $D^0\pi^+$. The decay is boosted in a reference frame where the hadron-lepton system is at rest. In the boosted frame the cosine of the angle between the neutrino and the soft pion is:

$$\cos\theta = \frac{1}{|P_{\pi_s}||P_\nu|}\left\{E_D E_{\pi_s} - \frac{1}{2}(M^2_{D^*} - M^2_D - m^2_{\pi_s})\right\} \tag{B.1}$$

while the neutrino energy (and momentum) is:

$$E_\nu = |P_\nu| = \frac{M^2_D - m^2_{K\mu} - m^2_\nu}{2m_{K\mu}} \tag{B.2}$$

where $m_{K\mu}$ is the kaon-muon system invariant mass. Further, we construct a vector $\vec{u}$ that lies in the same plane as $\vec{P}_\mu$ and is perpendicular to $\vec{P}_{\pi_s}$ and a vector $\vec{v}$ perpendicular to $\vec{P}_{\pi_s}$ and $\vec{P}_\mu$. These two vectors plus the vector of unit length directed along the soft pion direction constitute the new frame shown in Fig. B.1.

Using Eqs. B.1 and B.2 we compute the $q^2(\phi_i)$ corresponding to the angle ϕ_i:

$$q^2(\phi_i) = m^2_\mu + m^2_\nu + 2E_\nu E_\mu - 2\vec{P}_\nu\vec{P}_\mu \tag{B.3}$$

where the scalar product $\vec{P}_\nu\vec{P}_\mu$ depends on ϕ_i:

$$\vec{P}_\nu\vec{P}_\mu = P^w_\mu P_\nu\cos\theta + P^u_\mu P_\nu\sin\theta\cos\phi_i \tag{B.4}$$

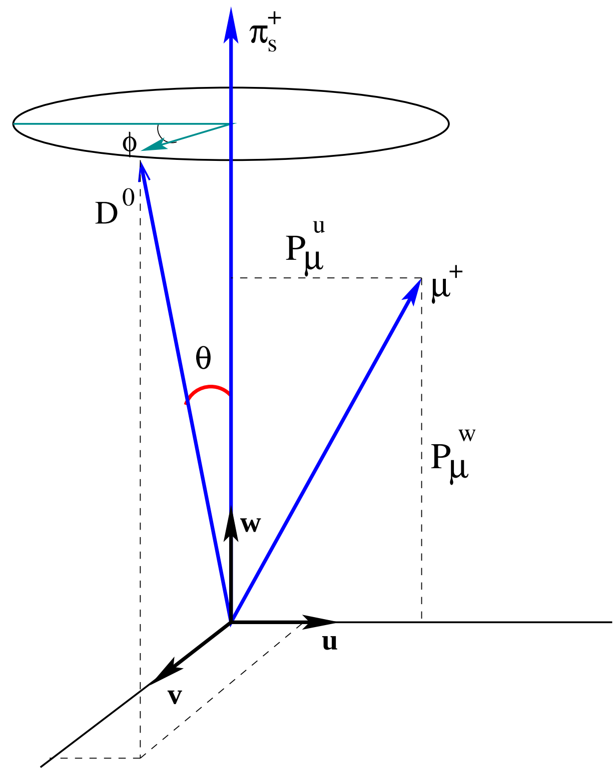

Figure B.1: $u\hat{v}w$ frame used in the D^{*+} cone closure

Now we construct a χ^2 test to the hypothesis that the D^0 direction (corresponding to ϕ_i) is consistent with coming from the primary vertex. This is achieved by boosting the system to the lab frame. If $\vec{P}_D$ is the vector of unit length describing the D^0 direction in the lab frame corresponding to the azimuthal angle ϕ_i, and $\vec{T}$ is the direction of flight reconstructed in the spectrometer, we can construct the quantity:

$$\mathcal{L} = \frac{\sum_i \sum_j \; P_D^i \; C^{ij} \; T^j}{\sum_i \sum_j \; P_D^i \; C^{ij} \; P_D^j}$$

where C^{ij} is the inverse covariance matrix of the sum of primary and secondary vertices covariance matrices and the indexes run over the x, y and z axis in the lab reference frame. By defining the variable Δ^i as:

$$\vec{\Delta} = \vec{V} - \mathcal{L} \; \vec{D}$$

we construct the χ^2 variable as:

$$\chi^2 = \sum_i \sum_j \Delta^i \, C^{ij} \, \Delta^j$$

Sweeping the angle ϕ, the q^2 value corresponding to the lowest χ^2 is saved. The error on the q^2 is then computed by changing it of an amount that corresponds to a change of 1 units in the χ^2.